Development of a wind turbine condition monitoring facility for drivetrain torsional dynamics investigations

by

Paul van Niekerk

Submitted in partial fulfilment of the requirements for the degree

Masters of Engineering (Mechanical)

in the

Department of Mechanical and Aeronautical Engineering

Faculty of Engineering, Built Environment and Information Technology

UNIVERSITEIT VAN PRETORIA
UNIVERSITY OF PRETORIA
YUNIBESITHI YA PRETORIA

2018

Title: Development of a wind turbine condition monitoring facility for drivetrain torsional dynamics investigations

Author: P.J. van Niekerk

Supervisor: Prof. P.S. Heyns

Year: 2018

Abstract

Maintenance can be performed according to one of two strategies, failure based or condition based. In most cases, where large and expensive assets such as wind turbines are operated on a continuous basis, condition based maintenance is preferred. However, condition based maintenance relies on the continuous and accurate gathering of condition-information of the particular machine and its various components.

This dissertation reports the experimental and numerical work performed as part of the development of an experimental facility that will allow the development of condition monitoring techniques for wind turbines. This work is focussed on the torsional dynamics of a wind turbine setup. A physical setup, consisting of a 1.6 m diameter turbine, a 1:1.2 speed-multiplication gearbox, and a 24 Volt direct current generator is built. All of it is mounted within an open-return wind tunnel, which is also designed and built as part of this work. The following two cost-effective experimental techniques are used to measure the torsional natural frequencies: a shaft encoder tachometer from which instantaneous rotational frequency is obtained, and power signal analysis, where the generated voltage is recorded and analysed. It is shown how an algorithm developed by Diamond et al. (2016) is used for the shaft encoder geometry compensation. Frequency spectra based on Fourier transforms and short time Fourier transforms are used to identify harmonic frequencies. Both measurement techniques proves useful to identify not only natural frequencies of torsional vibration, but also various characteristic frequencies of the drivetrain such as shaft rotation, blade pass, gear mesh and generator armature. It is found that power signal analysis is more useful to identify the characteristic frequencies.

Torsional dynamics of the drivetrain and its components are also investigated with the following two numerical methods: an eight-degree-of-freedom torsional Lumped Mass Model (LMM), and a three-dimensional Finite Element Model (FEM). Torsional mode shapes and frequencies are calculated with both methods and a good agreement is found in the lower four

modes. Numerical results are then compared with the experimental results, where there is also good agreement in the lower four modes. Model updating is performed on the FEM and by changing the torsional stiffness of the flexible couplings, the difference between measured and calculated natural frequencies are reduced to less than 6 %. It is concluded that future models should address lateral vibration of the drivetrain and the support structure.

From this study the following is contributed to the wind turbine condition monitoring field: considerations for the design and a working example of an experimental facility for investigating torsional dynamics, illustration of two measurement techniques, and two types of validated numerical models.

Acknowledgements

I thank the following people for their contribution:

Table of Contents

Nomenclature

Abbreviation	Description
C-AIM	Centre for Asset Integrity Management at the University of Pretoria
CC	Closed Corporation
CM	Condition Monitoring
DAQ	Data AcQuisitioning
EOM	Equation Of Motion
FFT	Fast Fourier transform
FEM	Finite Element Model(ing)
Freq.	Frequency
HSC	High-Speed Coupling
LMM(s)	Lumped Mass Model(s)
LSC	Low-Speed Coupling
MPPR tacho	Multi-Pulse Per Revolution tachometer
NI	National Instruments
PC	Personal Computer
SPPR tacho	Single Pulse Per Revolution tachometer
WT(s)	Wind Turbine(s)
WTCM	Wind Turbine Condition Monitoring

Symbol	Description	Unit
A	Cross-sectional area	[m²]
c or C	Torsional damping	
F	Natural frequency	[Hz]
G	Shear modulus $\left[G = \frac{E}{2(1+v)}\right]$	[Pa]
I	Rotational inertia	[kg·m²]
J	Area moment of inertia	[m⁴]
K	Torsional stiffness	[N·m·rad⁻¹] or [kN·m·rad⁻¹]
l_e	Element length	[mm]
M	Bending moment	[N·m]
P	Power	[W], [kW] or [MW]
R	Radius	[m] or [mm]
T	Torque	[N·m]
V	Velocity	[m·s⁻¹]
P	Density	[kg·m³]

Subscript	Description
eff	Effective
gb1	Low-speed gearbox shaft
gb2	High-speed gearbox shaft
gs	Generator shaft
gr	Generator rotor
hsc	High speed coupling
lss	Turbine shaft (low-speed shaft)
lsc	Low speed coupling
rot	WT rotor
GMESH	Gear mesh

1 Introduction

1.1 Background

Wind energy takes the lead as a renewable energy source. According to the Global Wind Energy Council 63 GW of Wind Power was installed in 2015. This brings the total installed capacity to 432 GW. Locally the amount of installed wind power capacity almost doubled during 2015, from 570 MW to 1053 MW (GWEC, 2015).

Reliability of wind turbines (WTs) is a key to the growth of the wind energy industry as it is an incentive and security for investors. Two approaches are taken to improve the reliability of the WTs: Firstly, WT design is improved, and secondly, downtime due to failure is reduced through preventative maintenance.

Preventative maintenance is performed at an optimal time. Damaged or fatigued parts are repaired or replaced before failing. This ensures that the WT is not brought to an unforeseen standstill.

WTs are assets which need a preventative maintenance strategy. Optimal preventative maintenance is possible when the asset condition is known, be it a machine or a structure. Not only does this require effective condition monitoring (CM) techniques, but also an understanding of the dynamics of the asset. Considering the existing CM expertise in the field of rotating machinery, entering the wind energy industry is merely an extension of this field.

1.2 Literature review

The literature review gives background to the methods and theory relevant to this study by reporting methods that are used for the condition monitoring of WTs, principles of measuring torsional dynamics with a shaft encoder, modelling of WT drivetrains and the updating of mathematical models. This ensures that the work done in this study is a logical continuation of previous work.

1.2.1 State of the art of WT condition monitoring

García Márquez et al. reported condition monitoring techniques that are currently employed on WTs. They identified condition monitoring methods for seven components of the WT: blades,

1

rotor, gearbox, generator, bearings, yaw system and tower. A summary of the methods used for five of these components is given in Table 1-1. The yaw system and tower are excluded as it is not relevant to the current investigation of torsional dynamics.

Table 1-1: Condition monitoring methods used for the various components of the WT reported by García Márquez et al. (2012).

	Blades	Rotor	Gearbox	Generator	Bearings
Vibration	✓	✓	✓		✓
Acoustic Emission	✓	✓	✓		✓
Ultrasonic Techniques	✓				
Oil analysis			✓	✓	✓
Strain	✓				
Electric Signal Analysis	✓	✓		✓	
Shock pulse methods					✓
Process Parameters	✓			✓	
Performance Monitoring	✓		✓	✓	✓
Radiographic Inspections	✓				
Thermography	✓		✓	✓	

Blades

Avdelidis & Gan as well as Yang & Sun explain that WT blades are long slender wing-like structures usually made from composite materials such as fibre-glass. For large blades, carbon and Kevlar fibres are often used to reinforce epoxy resin. Currently the largest blades are more than 70 m in length; larger WTs are more cost-efficient and for this reason machines with rotor diameters of up to 240 m are planned. Blade manufacturing costs account for about 15 % of the total WT production cost (Avdelidis & Gan, 2013; B. Yang & Sun, 2013).

Zhou et al. report that causes of blade damage include moisture absorption, sleet, ultraviolet irradiation, corrosion, fatigue, wind gusts and lightning strikes. They also mention that damaged blades have broken into pieces that were flung up to 500 m from the WT tower. This not only pose a danger to people in vicinity, but also in many cases a damaged or unbalanced rotor causes damage of other components in the drivetrain, such as the gearbox or generator (Zhou et al., 2014).

2

Various authors reported methods that are used to either determine the health or monitor the condition of WT blades. These methods are presented in Table 1-2 with a short description of the method.

Table 1-2: Methods used for blade condition monitoring.

Method	Description
Visual inspection (Tchakoua, Wamkeue, Tameghe, & Ekemb, 2013; B. Yang & Sun, 2013)	Close-up inspection technique to locate any damage visible to human eye.
X-ray imaging (Tchakoua, Wamkeue, Tameghe, et al., 2013; B. Yang & Sun, 2013)	Radiographic imaging to inspect structure internally. Effective for detecting cracks and delamination.
Infrared thermography (B. Yang & Sun, 2013)	Identifying and sizing of discontinuities by thermal imaging.
Ultrasound (Tchakoua, Wamkeue, Tameghe, et al., 2013)	Estimating the health of the structure by evaluating echoing from high frequency sound.
Point tracking (Paulsen, Erne, Möller, Sanow, & Schmidt, 2009; Tchakoua, Wamkeue, Slaoui-Hasnaoui, Tameghe, & Ekemb, 2013)	Stereo-photogrammetry technique that is used to measure the blade deformation of an operational WT. Blade deformation can be translated to structural health through modal analysis.
Digital image correlation (DIC) (Avitabile, Baqersad, & Niezrecki, 2014; Helfrick, Pingle, Niezrecki, & Avitabile, 2009)	Full-field dynamic strain estimation by stereo-photogrammetry. Strain can be translated to structural health through comparison with FEM.
Modal analysis with accelerometers (Ganeriwala, Yang, & Richardson, 2011; Watson, Esu, Flint, & Lloyd, 2014)	Suggested low-cost instrumentation for vibration measurement on various locations on a blade. Blade vibration is translated to structural health through modal analysis.
Continuous scan laser vibrometry (S. Yang & Allen, 2012)	An algorithm for detecting mode shapes on an operational parked WT from a ground based laser; velocity is measured by the laser. Mode shapes can be used to determine structural health.
Optical fibre strain measurement (Arsenault, Achuthan, Marzocca, Grappasonni, & Coppotelli, 2013; Tchakoua, Wamkeue, Tameghe, et al., 2013)	Distributed strain measurement. Strain can be translated to structural health through comparison with FEM.

Hub

Only 7% of annual failures are related to damage in the rotor hub, according to Faulstich et al. They report on the reliability of various WT subassemblies. Data originates from a survey that was taken on a representative sample of German WTs over a seventeen year period from 1989

to 2006. However, each rotor hub failure on average caused close to 4 days of downtime (11% of the mean annual downtime) (Faulstich, Hahn, & Tavner, 2011). It is important to monitor the condition of the hub. This component is constantly stressed as it is transferring moments from the blades to the turbine shaft. Fluctuating wind loads impose fluctuating stresses on the hub, creating the ideal environment for fatigue. It is at the connection of the blade that one expects fatigue crack growth.

Turbine shaft

Not only does the turbine shaft transfer a moment from the WT rotor to the gearbox (or directly to the generator in some cases), but also it is subjected to large torque reversals due to fluctuation of the wind speed and electric load. According to Tchakoua et al. there are various condition monitoring methods that are used on the shafts of a WT. Torque measurement, acoustic emission, strain measurement, and visual inspection are listed (Tchakoua et al., 2014). It is conceivable that ultrasonic testing will reveal growing cracks, although it requires machine outage. Modal analysis is also useful as growing cracks alter the damping and stiffness properties of the shaft.

Generator

WT generators fail mechanically and electrically. Bearing damage is the most common mechanical failure. An example of electrical failure is short circuiting of rotor or stator windings. Various condition monitoring techniques that are used for WT generators are shown in Table 1-1, as reported by García Márquez et al. (2012). Interestingly, Yang et al. devised a condition monitoring technique which can be used for generator fault detection by analysing the power signal and rotational speed of the generator. The method is validated on a WT test rig (W. Yang, Tavner, Crabtree, & Wilkinson, 2010).

Gearbox

WT gearboxes need to be able to withstand extraordinary loading conditions. Connection and disconnection to the electrical grid which happens regularly since the WT needs to generate a specific frequency, means that the drivetrain is accelerated quickly and experiences large torque reversals which can damage gears. Torque reversals of 1230 kN·m in less than 100 milliseconds have been measured on the intermediate shaft of a 1.5 MW gearbox. Another factor that complicates WT gearboxes is the extremely high torques at low rotational speed on the one side

4

and low torque at high rotational speed on the other side (Kotzalas & Doll, 2010). This means that the lubrication that is used is optimal for only one of these sides. Larger rotors cause larger loads on the drivetrain components; provision need to be made for larger rotors that are used more commonly (B. Yang & Sun, 2013).

It is reported that failure of the gearbox is the largest contributor to WT downtime; 24% is reported (Mcmillan & Ault, 2007). In the previous subsection it was mentioned that 80% of gearbox failures result from faulty or worn bearings. Other causes of gearbox failures that were found in literature are broken gear-teeth, leaking gearbox casings, insufficient lubrication and misalignment due to displacement and eccentricity (Tchakoua et al., 2014).

In many cases the whole or parts of a gearbox need to be replaced, which results in prolonged downtime. A case of severe downtime reported in literature was due to the combination of unscheduled maintenance, where parts need to be ordered from the manufacturer, and prohibiting weather conditions. Downtime stretched to 700 hours (29 days) (Mcmillan & Ault, 2007). Another source reported a mean annual downtime of 14 hours caused by gearbox failures (Faulstich et al., 2011). Improved CM and scheduled maintenance can reduce downtime due to gearbox failure.

A variety of methods are used to monitor the condition of gearbox components. Favourites include oil analysis and vibration analysis, which are used to detect the amount of wear on gear teeth and bearings. Other methods that are reported in the literature are summarised in Table 1-1.

1.2.2 Existing facilities

Detrick, Yang and Ganeriwala mention the WT simulator that was developed by *SpectraQuest*. The simulator is a fully functional small-scale WT that can be used for training of wind farm operations and maintenance personnel, as well as for research. Components such as blade pitch mechanisms and nacelle yaw are part of the simulator. The setup has also been used for gearbox vibration analysis (Detrick, Yang, & Ganeriwala, 2012).

Yang and Yang et al. report the use of an experimental setup that was designed for developing CM methods based on the (generated) electric signal. The drivetrain consisted of a DC motor, a gearbox and synchronous permanent magnet generator connected to resistive load banks.

Accelerometers, torque transducers and proximity sensors were installed on the setup (W. Yang, 2015; W. Yang et al., 2010).

1.2.3   Shaft encoder measurement

Diamond et al. developed an algorithm for accurately measuring instantaneous angular speed with a non-perfect zebra-strip shaft encoder. Their algorithm relies on Bayesian regression to calculate the encoder geometry. They showed that the algorithm is capable of determining the shaft encoder geometry given any non-steady shaft speed (Diamond, Heyns, & Oberholster, 2016).

1.2.4   Torsional dynamics modelling

LMMs have been developed for WT drivetrains. One such model attempts to capture the fundamental frequency of torsional vibration (Girsang, Dhupia, Muljadi, Singh, & Pao, 2013). Another example is more complex. This drivetrain consists of shafts, a planetary gear stage, and two spur gears. Stiffness, inertia, and damping are described in Lagrangian equations of motion with which the matrices are populated and eigenfrequencies can be solved (Shi, Kim, Chung, & Park, 2013).

Scheepers reviewed rotor dynamics modelling which included torsional vibration. He reports that lumped and distributed parameter models are two of the discretisation approaches that are used for modelling rotor systems. Distributed parameter models are typically able to produce more accurate results than the lumped parameter models, mainly due to a higher level of discretisation. However, lumped parameter models are 'generally adequate for investigating machine layouts and low order sub-synchronous frequencies'. FEM, due to the ease of commercial software packages, provides the finest discretisation when three dimensional models are used, and as expected, yield more accurate results than one dimensional models (Scheepers, 2013).

1.2.5   Model updating

Krüger updated a one dimensional and a three dimensional FEM. He used the 'MSC.Nastran Design Optimization capability'. An error function was specified to minimise the difference between the natural frequencies obtained from FEM and the frequencies obtained through experimental analysis. Elastic moduli of the FEM were updated and the result was that the first

three natural frequencies of the updated model differed with less than 4 % compared to the experimental results. Damping was neglected (Krüger, 2012).

1.3 Scope

Condition monitoring is critical to the profitable use of WTs. Unlike a run-to-failure maintenance strategy, a condition-based maintenance strategy enables the wind farm operator to schedule maintenance during planned outages. However, there are multiple components in a WT, each requiring mature condition monitoring technology applicable to that specific component. At least eleven condition monitoring methods are applied on WT components. It ranges from online vibration and power signal monitoring, to periodic investigation techniques such as ultrasonic testing and oil analysis (García Márquez, Tobias, Pérez, & Papaelias, 2012). Vibration monitoring has been used extensively in rotating machinery and can be considered a mature technology. However, efforts are made to develop more advanced and effective vibration monitoring technology for WTs, for example on the blades (Watson et al., 2014). Several studies have focussed on optical techniques such as laser vibrometry (S. Yang & Allen, 2012) and photogrammetry (Paulsen et al., 2009). Power signal analysis was investigated and has been proven useful as a condition monitoring method (W. Yang, 2015; W. Yang et al., 2010).

Online or in-operation condition monitoring is important in the condition monitoring of WTs. Contact methods such as ultrasonic testing and oil analysis not only require an outage, but also access to the nacelle. And since increasing numbers of WTs are installed offshore, access to the turbines is expensive and even dangerous. There are many benefits in monitoring the machine from a central point. However, online condition monitoring requires a thorough understanding of the characteristics of the machine, the operating conditions of the machine and the correct interpretation of measured data. The characteristics of the machine determine its response to the operating conditions, and a change in the condition of the machine is reflected in the response. Interpretation of data is important in order to detect such changes.

One set of characteristics is that of the drivetrain, described by the torsional dynamics. The torsional dynamics is the torsional response of the drivetrain to the given operating conditions. It is dependent on the characteristics of the components, and therefore on the condition of each component.

With this situation as background, the investigation is undertaken and the work of this study is chosen. This project entails the development of a physical facility which can be used to

investigate the torsional dynamics of WTs on a laboratory scale. Development of this facility encompasses the,

- definition of the requirements of such a facility,
- design and manufacture of the facility,
- modelling of the WT's torsional dynamics, and
- measurement of the torsional dynamics.

Existing facilities with a similar purpose are described in the literature. One is a full-scale large size WT (Paulsen et al., 2009) and the other is a small-scale WT. The former can be driven by natural wind whereas the latter is driven with wind from a fan. These facilities served as inspiration for the development of the new WT condition monitoring facility at the University of Pretoria. Apart from being less expensive, a small WT can be driven by wind from a fan, enabling better control of the operating environment. A commercial WT, even if it is small, has technology such as blade materials and generator functions that are similar to large scale WTs. Another consideration is the configuration of the drivetrain. Since there is a large interest in the condition monitoring of bearings and gears in wind turbine applications, it makes sense to develop a facility which have these components.

Torsional dynamics may be described by the torsional mode shapes, natural frequencies and damping of a system. These parameters (excluding damping) may be estimated with either LMMs or FEM. LMMs of WT drivetrains have been developed. It requires a set of equations of motion that describes the mass, stiffness and damping distribution in the drivetrain. In this case damping is deemed negligible. One example captures the dynamics of a multiple shaft and multiple gear stage drivetrain (Shi et al., 2013). Another example reduces the drivetrain to two lumped masses with which the fundamental vibration frequency is estimated (Girsang et al., 2013). Finite elements are used for higher order modelling of the drivetrain. The large number of degrees of freedom in a FEM not only allows the estimation of more modes, but also for better accuracy. Commercial software packages have been proven in the solution of many industrial problems. Reportedly, it has also been used to model the drivetrain of a WT (Haastrup, Hansen, Ebbesen, & Mouritsen, 2012).

To illustrate the use of the facility, the torsional dynamics of the installed drivetrain is measured. Instead of a complete torsional modal analysis, which will include the mode shapes, damping and frequencies, only the natural frequencies are determined. These frequencies are used to investigate the torsional behaviour of the drivetrain. Lateral dynamics must however

also be understood. Lateral vibration is measured with a tri-axial accelerometer at specific points on the drivetrain, during modal analyses. The information from these measurements helps to distinguish bending modes from torsional modes. Torsional vibration modes can also be identified from the lateral vibration measurement. The focus of measuring the torsional dynamics is the use of rotational speed and power signal analysis. Using two methods enabled us to compare the performance of each with the other. It is not necessary to use tri-axial accelerometers as well for torsional vibration. A fairly high angular resolution encoder (minimum 94 samples per revolution) is used in an attempt to capture torsional vibration while the drivetrain is rotating under normal conditions. Zebra tape is used as a shaft encoder and a multi-pulse per revolution tachometer signal is obtained. Voltage serves as a power signal, which is also analysed to identify system dynamics and torsional vibration modes. Two methods The FEM is validated with the frequencies that were measured experimentally.

Although it is not practical to obtain the design details of utility size WTs (this is protected intellectual property of the manufacturers), the principles of measurement and modelling investigated in this study are applicable for utility size WTs. In the industry, design details could be purchased from WT manufacturers, and used under license, to develop suited torsional dynamics models and CM methods for the specific machines. Rather, this facility makes provision for current methodology by serving as a platform for installing and using instrumentation such as tachometers, accelerometers, laser vibrometers and photogrammetry cameras.

1.4 Overview

Background to the project is given in Chapter 1, which highlights some current developments in the wind energy industry and the need to maintain WTs. The literature is consulted to learn about the existing condition monitoring techniques for WTs and to obtain an overview of the state of the art. The scope of the dissertation is stated and the content of the dissertation is summarised in an overview.

Chapter 2 describes the design and manufacture of the experimental test facility. First the requirements of the setup are stipulated. Then possible solutions are considered, as concepts, after which the detail of the final design is presented. Pictures and drawings are used to illustrate the design and the manufacture of the test setup.

Mathematical models of the WT drivetrain are developed in Chapter 3. The first model is a 'lumped mass' model and the development includes the discretisation of the geometry, the equations of motion and the results of an eigenvalue analysis performed on its mass and stiffness matrices. The second model is a FEM and the details that are reported include simplification of the geometry, the elements that were used, boundary conditions, and results of the eigenvalue analysis.

Measurement of the torsional vibration is described in Chapter 4. Instrumentation, equipment and the experimental procedure are detailed. Measured vibration data is then analysed to find the frequencies of the torsional vibration modes. Finally the properties of the lumped mass and FEM are adjusted in an attempt to match the estimated frequencies of torsional vibration with the measured frequencies.

Lastly, conclusions are drawn and presented in Chapter 6. Outcomes of the study are compared with the objectives and recommendations are made for future work.

2 Experimental setup

2.1 Background

Without access to WTs, studies are limited to the modelling of components. Facilities are needed where condition monitoring methods for WTs are applied, improved and developed. Such facilities need to accommodate both the existing technology and allow for further developments. To fulfil this requirement four considerations govern the design of the facility:

1. Design the facility to fit indoors;
2. Make use of a commercially available WT;
3. Power the turbine by wind from a fan; and
4. Insert at least a single gear stage in the drivetrain.

With the conditions of the design laid, the components of the facility are considered individually while keeping in mind that it forms part of the system. The design process includes the concepts that are considered, calculations and equipment selection.

2.2 Design

2.2.1 Turbine

A WT is needed which is sold commercially and suitable for the available space. Rotor diameter, blade material and cut-in wind speed are considered. Each of these properties are discussed below.

Rotor diameter is limited by the available space in the laboratory. Considering the cost, it was decided to use a small WT, complete with rotor and generator. Laboratory space allows for rotor diameters smaller than 2.5 meters. Various models in this class are available, mainly for battery charging purposes.

Blades of utility scale WTs are typically hollow and wing like, made of fibreglass composite material. The blades of the WT condition monitoring facility need to be made from a similar material to extend the use of the facility to methods that are applicable to large WT blades.

11

The rated cut-in wind speed of the turbine is the lowest wind speed that a WT requires to start generating electricity. A lower cut-in wind speed increases the range of operating wind speeds of the setup. Cut-in wind speed was included in the selection criteria, lower being preferred.

Two machines were considered: the Kestrel e160i and the Primus wind power Air 40. Both these machines are commercially available in South Africa, and of suitable size. Details of the two machines are presented in the table below with the specifications that were considered.

Table 2-1: Specifications of two small wind turbines that were considered.

	Kestrel e160i[a]	Primus wind power Air 40[b]
Number of blades	5	3
Rotor diameter [m]	1.60	1.17
Cut-in wind speed [m·s^{-1}]	2.5	3.1
Rated power, [W]	750 at 12 m·s^{-1}	220 at 12 m·s^{-1}
Blade material	Fibreglass Composite	Injection Moulded Composite

[a] (Kestrel Renewable Energy, 2014); [b] (Primus Wind Power, 2014)

Both the Air 40 and e160i WTs are suitable. The Kestrel e160i was favoured based on three factors: lower cut-in wind speed, a larger diameter WT for a similar price, and it is produced in South Africa which creates the possibility of support from the manufacturers.

Figure 2-1 shows the rotor and generator of the Kestrel e160i. The purchase also included a fibre-glass nacelle cover and a tail fin. The back plate of the turbine was disassembled from the generator. Then the turbine was assembled according to the specifications prescribed in the manual. A component called the 'turbine boss' was manufactured for mounting the turbine onto a 25 mm diameter shaft. The boss is fixed to the rotor with five M10 bolts. A detail drawing of the boss is given in Appendix B.
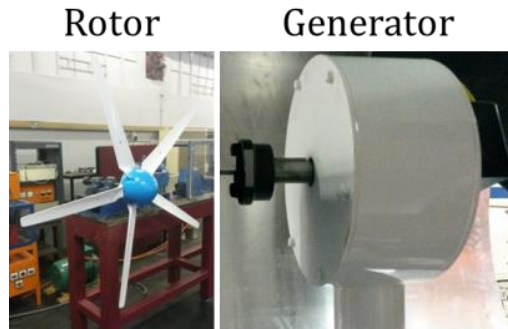
Figure 2-1: Main components of the Kestrel e160i.

2.2.2 Duct

On wind farms, WTs are elevated above obstructions such as trees and landscape features that cause turbulent airflow. This practice not only protects the machine against the associated loads, but also ensures more sufficient use of the available kinetic energy in the wind. For the same reasons, and to protect operators, a duct is required to safely and efficiently channel a flow of air inside the laboratory. The function of the duct is to channel air through the WT at a uniform velocity. Two specific requirements were derived from the fulfilment of this function:

1. Sufficient air flow to drive the WT.
2. Uniform flow velocity through the WT.

Another requirement that stemmed from the purpose of the facility is that it should be possible to use relevant condition monitoring measurement techniques. For the WT blades, optical measurement techniques are considered most important. Such methods are photogrammetry, digital image correlation, and scanning laser vibrometry.

Literature on wind tunnels was consulted. Existing wind tunnels were considered as concepts for the duct. Work by Barlow et al. indicated three main configurations of wind tunnels: closed loop, open jet and open return (Barlow, Rae, & Pope, 2010).

Although a closed loop wind tunnel will be the most energy efficient, it will not be feasible for the WT condition monitoring facility. After visiting the wind tunnel facilities of the CSIR, guided by Peter Skinner, it became clear that flow conditioning is required for closed loop wind tunnels. Flow conditioning typically consists of expansion chambers, wire meshes and honeycomb flow straighteners. A contraction chamber is also necessary upstream of the test section. Open jet and open return configurations were considered. See Figure 2-3.

13

An open jet wind tunnel blows air onto the WT. It provides unobstructed access to the drivetrain. Flow conditioning, in the form of a honeycomb, wire mesh and contraction chamber, is necessary for a uniform flow velocity at the jet. An open jet wind tunnel obstructs the view of the WT from the front and complicates the use of optical measurement techniques.

With an open return configuration it is possible to have the fan downstream of the test section. A bell mouth inlet to the wind tunnel improves the smoothness of the flow at the entry of the tunnel and renders it unnecessary to have additional flow conditioning. View of the WT blades from the front is unobstructed, although access to drivetrain components is limited. The open return type wind tunnel was selected as the final concept.

A uniform velocity is required over the WT. However, a boundary layer was expected to develop in the duct, starting from the inlet. To determine the boundary layer thickness at the WT, a bell-mouth inlet with a quarter-ellipse shape was selected (see Figure 2-2). It was assumed that the inlet shape could be approximated with several flat plates. The development of the boundary layer across these flat plates was then calculated. With this method, for the inlet geometry, it is estimated that the boundary layer is developed to approximately 46 mm at the WT rotor. A factor of 1.5 was included for uncertainty, which results in a tip clearance of 70 mm. Therefore, at the WT the duct diameter is 1.74 m.
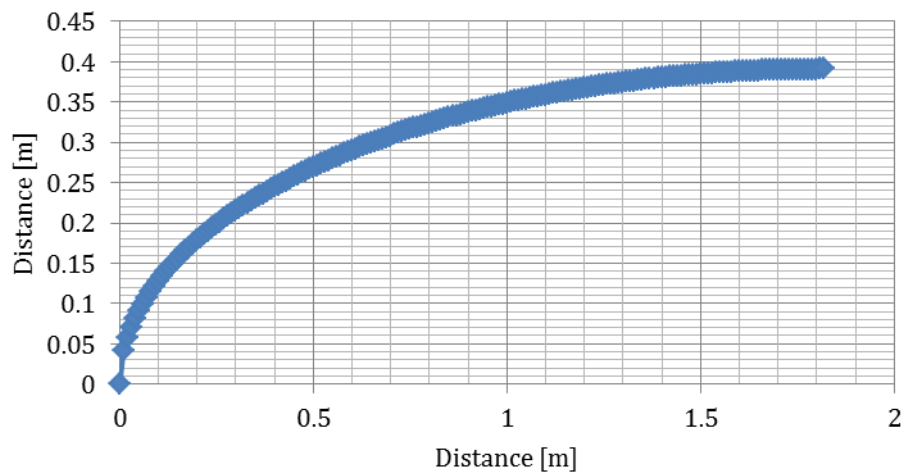

Figure 2-2: Quarter-ellipse shape of the bell-mouth inlet.

It was expected that the air flowing through the WT will slow down and expand. The turbine rotor acts as a diffusor. To maintain constant pressure through the duct it is necessary to increase the duct diameter immediately downstream of the WT rotor.
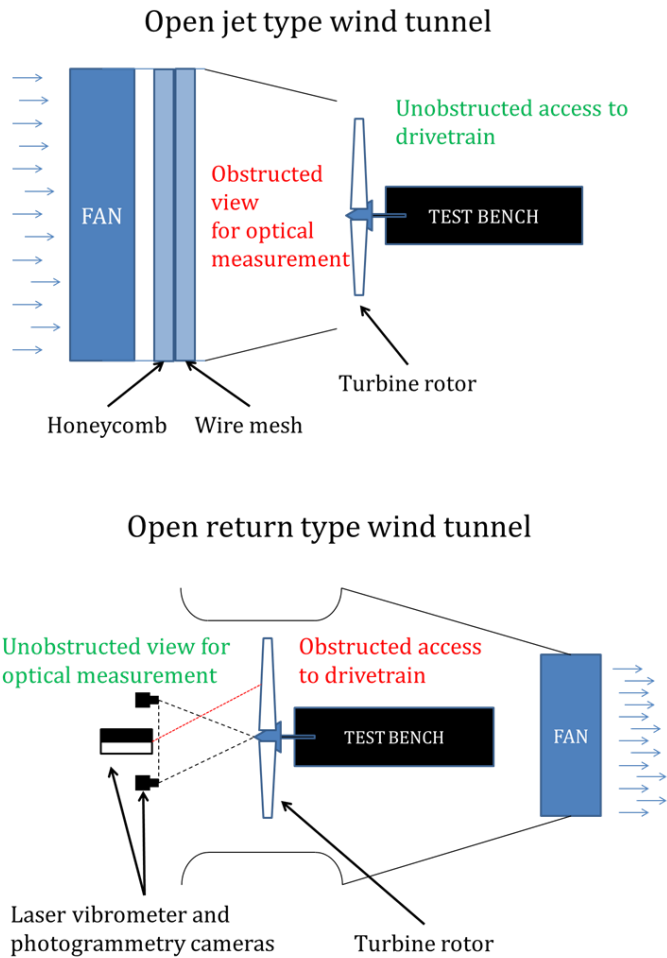
Figure 2-3: Open jet and open return concepts for the wind tunnel.

Wingfan Africa CC, supplier of industrial fans, was consulted for the selection of a fan. Several improvements of the duct wind tunnel layout in Figure 2-3 were suggested. The duct geometry is simplified by selecting a fan with a diameter similar to that of the WT, which implies a constant diameter between the inlet and the fan. A constant diameter is not only simpler to manufacture but also causes a smaller pressure drop through the duct. A diffusor is included behind the fan for pressure recovery and increasing the efficiency. Figure 2-4 shows the subsequent layout of the duct.

15
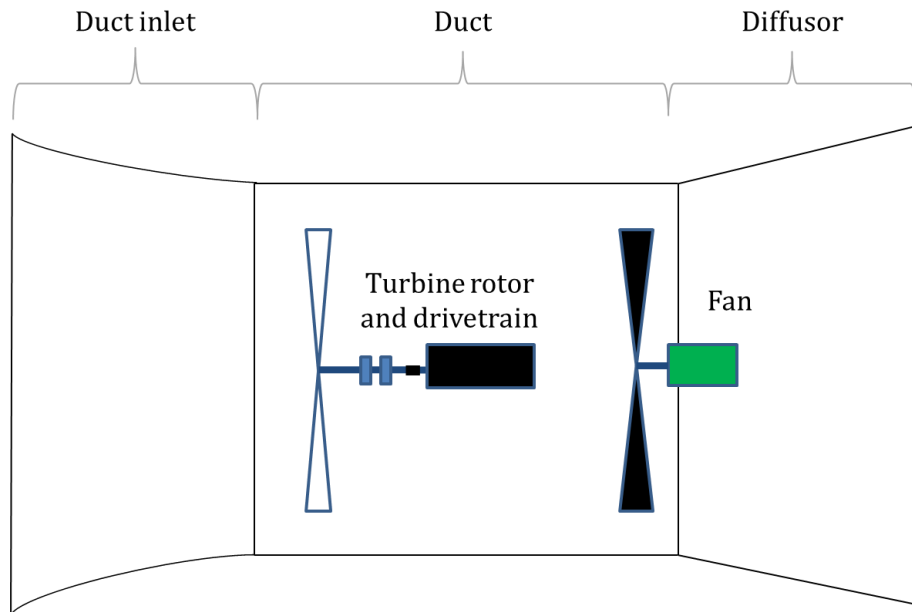
Figure 2-4: Final duct concept.

2.2.3 Fan

The fan creates a pressure drop across the WT by displacing air from the back of the wind tunnel. Sufficient air flow is required for the wind speed to be above the cut-in wind speed of the WT. The Kestrel e160i is designed to operate in wind speeds between 2.5 and 13 m·s^{-1}. A maximum wind speed of 10 m·s^{-1} was chosen. This speed is well above the cut-in wind speed and in the higher end of the turbine's operating range.

The duct inlet has a cross-sectional area of 2.38 m^2 at the WT. An air flow of 23.8 m^3·s^{-1} is required to provide a wind speed of 10 m·s^{-1}.

Fritz Eksteen, consultant with Wingfan Africa, made use of Select 6 fan-selection software (WingFan Ltd. & Co. KG, 2014). The required performance parameters that were provided to the software are the air flow of 23.8 m^3·s^{-1}, fan diameter in the region of 1.74 m, and a static pressure drop of 100 Pa. The static pressure drop of 100 Pa was estimated according to the geometry of the duct and the obstructions in the duct. The software analysed the given parameters and returned possible designs.

Table 2-2 summarises the details of the selected fan. Refer to Appendix D for the fan's performance curves. Note that the fan is rated to displace 21.4 m^3·s^{-1} which is less than the required 23.8 m^3·s^{-1} and will only provide a wind speed of 9.3 m·s^{-1}. The number of blades and

the rotational speed in Revolutions Per Minute (RPM) , also given in the table, are important for the system dynamics.

Table 2-2: Specifications of the selected fan and operating point.

	Value
No. of blades	3
Rotational speed [RPM]	960
Air flow, [m³·s⁻¹]	21.4
Static pressure, [Pa]	120
Power, [kW]	7
Diameter, [m]	1.8

Another consideration was the static pressure that the fan had to overcome due to flow obstruction. An estimate of 100 Pa was made by the Wingfan Africa consultant, based on experience. The estimation was controlled with the duct-design rules found in the 1993 ASHRAE manual; a static pressure drop of 95 Pa was calculated. However, the selected fan overcomes a static pressure drop of 120 Pa which provides a 20% margin for error in the estimation.

2.2.4   Gearbox

The WT rotor of the Kestrel e160i is designed to drive the generator directly, without speed multiplication or reduction. However, to allow for gear damage studies, a gearbox is included in the drivetrain.

Gear pairs are often replaced during gear damage studies. Two requirements on the gear stage stem from this procedure: firstly, gears need to be readily available so that it can be replaced after being damaged and secondly, the gearbox disassembly and reassembly need to be effortless. A gearbox is required that does not necessitate the disassembly of the drivetrain.

It was decided to design and manufacture a gearbox to meet the requirements set out above. A horizontally split casing, as shown on the left in Figure 2-5, provides access to the gears without removing shafts. Gears are allowed to be removed without removing bearings, with the shaft configuration shown on the right hand side of the figure.

Spur gears from the 4th gear of a Yamaha YZ250F motorcycle transmission were chosen. Specifications of the gears are summarised in Table 2-3. These gears are obtainable from motorcycle spare part traders, allowing replacement during gear damage studies. Shaft dimensions were chosen accordingly and the designs were analysed to determine whether it will be able to withstand the loads.

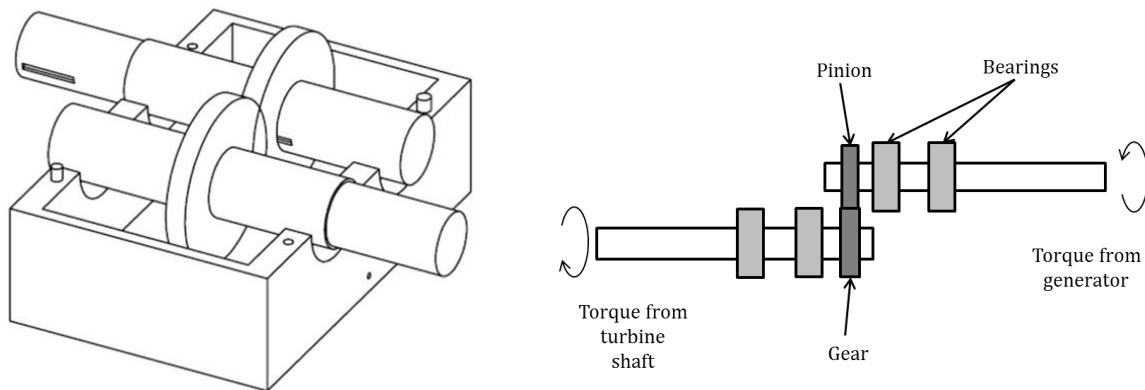Orthographic and isometric drawings of the assembled gearbox are shown in Appendix B.

Figure 2-5: Horizontal split casing (left) and improved shaft configuration (right)

Table 2-3: Specifications of the transmission.

		Gear	Pinion
	No. of teeth	22	18
	Pitch diameter, [mm]	55	45
	Ratio	1.2̇	
	Rated transmitted power, [kW]	3	

2.2.5   Resistor bank

Electric energy is dissipated as heat through two rheostats (R_1 and R_2) which are connected in parallel. One of the rheostats is shown in Figure 2-6. A voltage divider circuit, consisting of two resistors (R_3 ad R_4) connects or disconnects one of the rheostats (see Figure 2-6). Resistance of the two rheostats are fixed. When connected in parallel the effective resistance is $R = (1/R_1 + 1/R_2 + 1/R_3 + 1/R_4)^{-1}$.

The voltage divider circuit provides a voltage which is proportional to the voltage across the rheostats. The maximum output voltage of the generator is 120 V, and a maximum of

approximately 10 V is delivered to the data acquisitioning system. This is connected to the National Instruments data acquisitioning system.
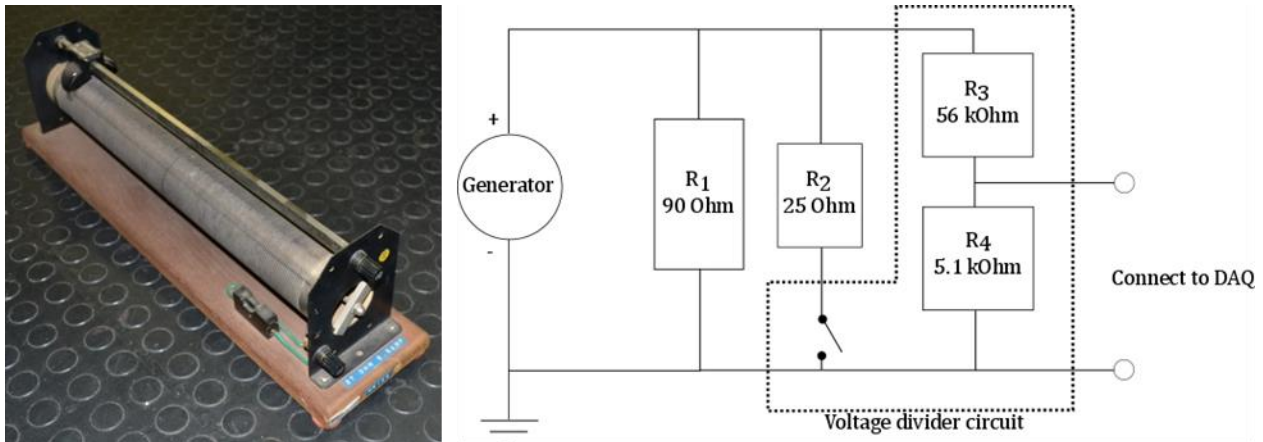

Figure 2-6: Rheostat and electric circuit.

2.3 Illustrations and drawings

Figure 2-7 shows the overall dimensions of the assembled setup. Note that it is close to five metres in length and three metres in width. The centre of rotation is ~1.64 m from ground level, which brings the maximum height of the setup close to three metres as well. Refer to Appendix B for another drawing and a list of components. In the drawing the door-panel of the duct is removed to make visible the drivetrain components.

Figure 2-8 (a) is a photo of the turbine from the front. The turbine is seen in position, where the bell-mouth inlet meets the duct. The WT is in line with the narrowest part of the inlet. The clearance between the blade tips and the inlet wall is approximately 50 mm. The inlet surface is smooth for minimum flow friction and disturbances. A steel frame (galvanised finish) supports the inlet separately from the test bench and duct.

From the back, in Figure 2-8 (b), notice that there is no diffuser behind the fan. Although a diffusor may increase the efficiency of the fan, it proved to be unnecessary for achieving the desired flow. The blue frame visible on the picture supports the aluminium duct. Figure 2-9 shows the support frame closer. Notice that the weight of the aluminium duct is supported by a horizontal angle-section along the length, (a) and (b). The hinges that allow the side of the duct to pen are visible on (b).
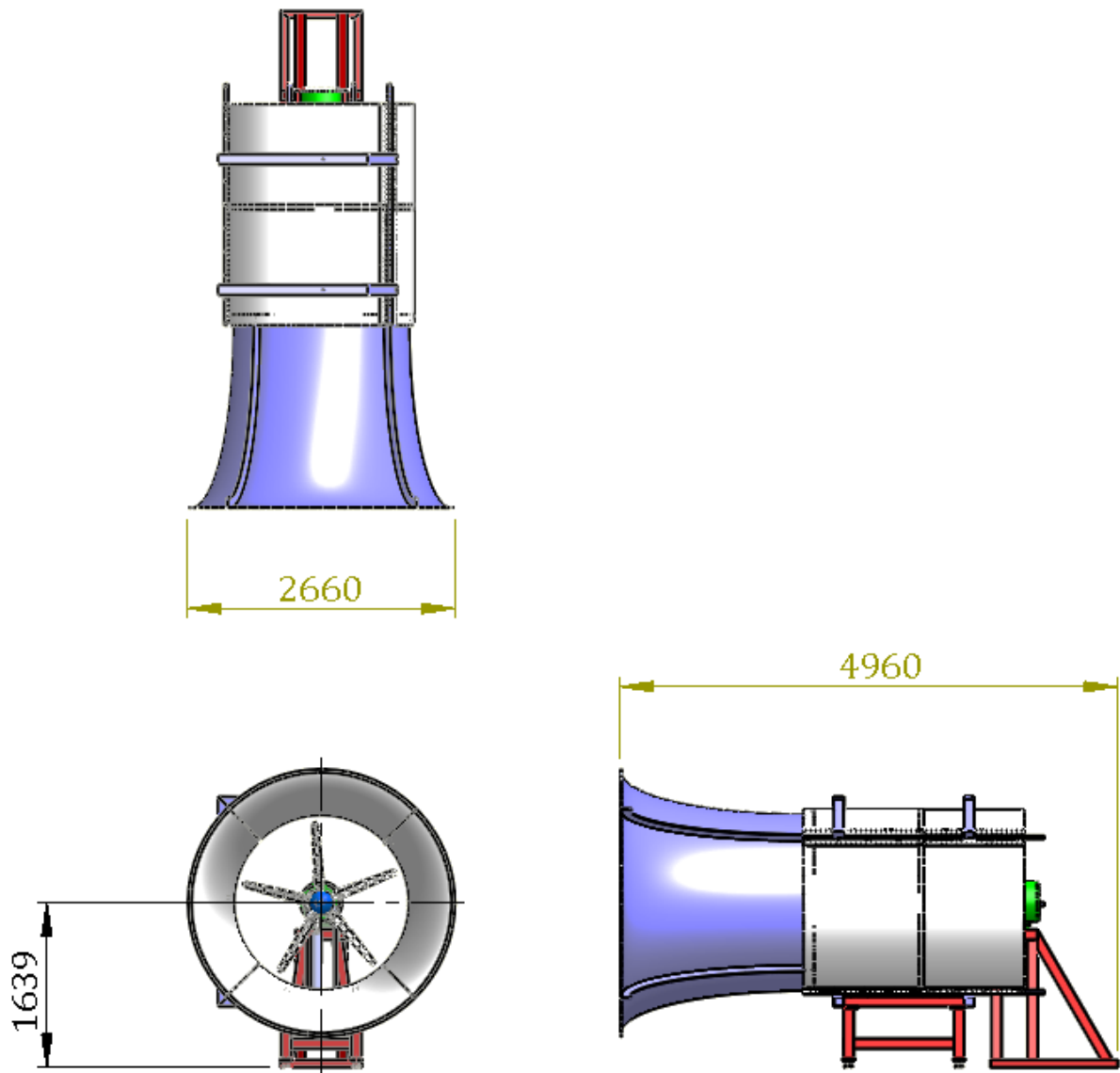
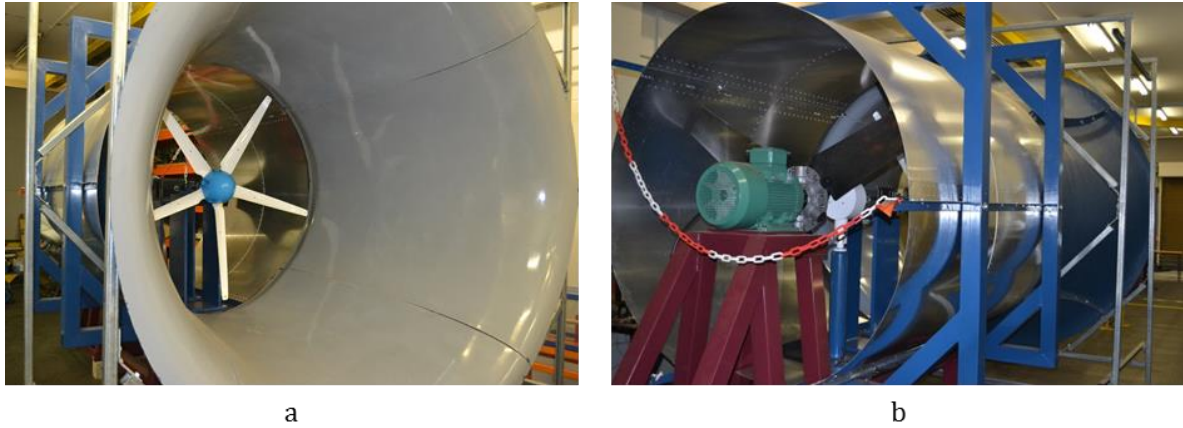Figure 2-7: Three view with overall dimensions of the test setup.

<center>a   b</center>

Figure 2-8: Photos of the complete setup from the inlet (a) and from the outlet.
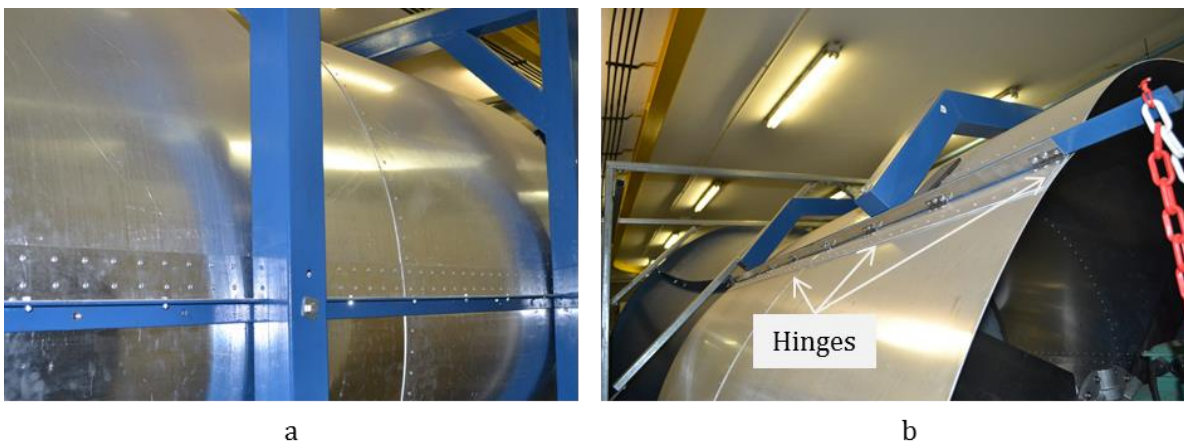

<center>a   b</center>

Figure 2-9: Support frame of the duct, on the closed side (a) and at the hinge (b).

Figure 2-10 shows the drivetrain from the back, when the door is open. The turbine, gearbox and generator are connected, while the fan (at the right of the picture) is separated from the drivetrain.
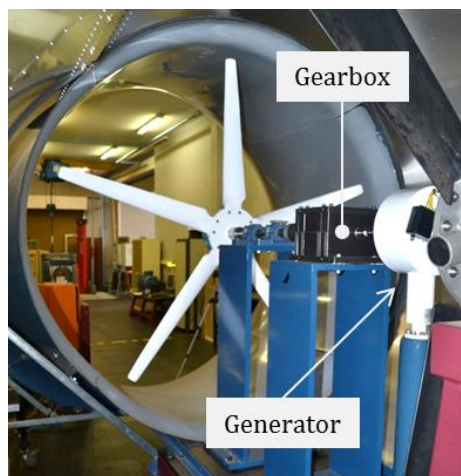

Figure 2-10: Photo of the drivetrain from the back.

3 Modelling

3.1 Background

Consider Figure 3-1 which shows the components of the WT drivetrain. The figure indicates the rotating components which are modelled in this chapter. These are modelled as torsional dynamics models, which estimate the shapes and frequencies of the vibration modes. Two modelling approaches are followed: lumped masses and finite elements. The LMM is used to obtain approximate values of the first few modes of torsional vibration. Whereas the LMM is limited to estimate torsional mode shapes and frequencies, a FEM captures more detail of the drivetrain and provides estimates of the lateral bending modes as well as torsional modes. It is used not only to verify the LMM, but also to gain accurate estimations of the higher torsional modes.

3.2 Lumped mass model

Rotational inertia and torsional stiffness of drivetrain components are used to develop a lumped mass representation of the WT drivetrain. Figure 3-2 illustrates the discretisation of the drivetrain. The drivetrain is discretised into eight rotating bodies with rotational inertia, I_1 - I_8. These bodies are located at the centres of mass of the components with the larger rotational inertia: the WT rotor, couplings, gears and the generator rotor.

1. Wind turbine rotor
2. Low-speed shaft
3. Coupling
4. Gearbox input shaft
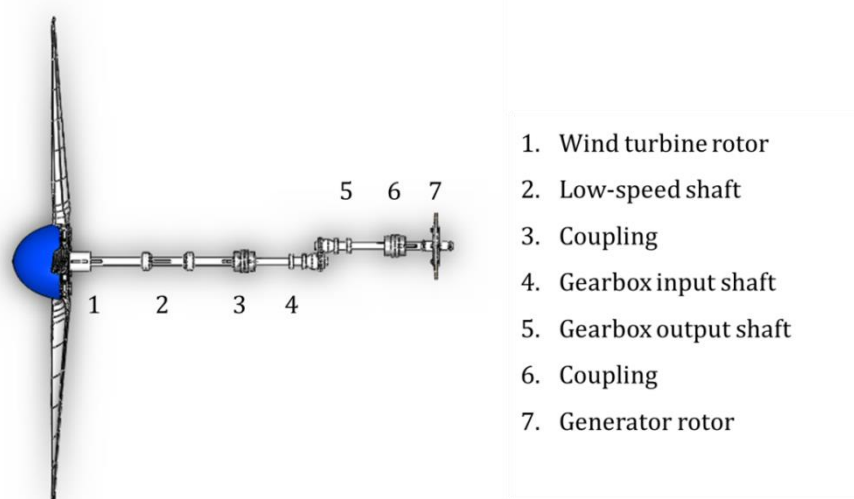5. Gearbox output shaft
6. Coupling
7. Generator rotor

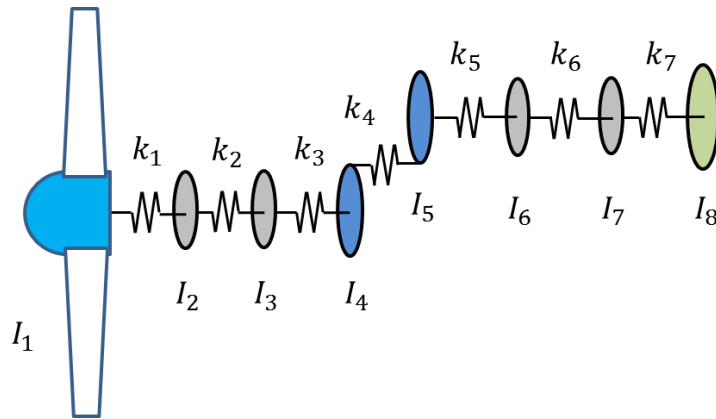Figure 3-1: Parts of the WT drivetrain.

Figure 3-2: Illustration of the LMM.

Inertia of the drivetrain components is estimated with Solidworks in a few simple steps: Firstly the dimensions and mass of the physical components are measured. Then detailed solid models are created. The software's mass properties tool was used to estimate the volume of each solid model. Mass density of each component was calculated with the estimated volume and the measured mass. Provided with the correct mass density, the mass properties tool was used to estimate the rotational inertia around the three principal axes with its origin at the centre of mass.

Since the generator is sealed, dimensions and mass of the generator rotor were not measured. Solid models of the inside components were created from the detail drawings supplied by the manufacturer. Mass densities that are specified by the manufacturer for the generator components were used.

Elasticity in the drivetrain is represented by seven springs. Six of the springs, k_1 to k_3 and k_5 to k_7, represent the torsional stiffness of the shafts and the couplings. The remaining spring, k_4, is a linear spring that represents the stiffness of the gear mesh.

Torsional stiffness of the shafts was estimated analytically with equation (3-1). In order to use the equation, the shafts were assumed to be solid cylinders with the dimensions as given in Table 3-2 with explanation in Appendix B. The following material properties for steel were used: a Young's modulus E = 200 GPa and Poisson's ratio ν = 0.3.

$$k = \frac{GJ}{L} \tag{3-1}$$

23

Table 3-1: Constant diameter equivalents of the drivetrain components.

Shaft	Length [mm]	Diameter [mm]
Turbine	450	25.0
Gearbox low-speed	106	20.1
Gearbox high-speed	105	20.1
Generator	52	24.0

The torsional stiffness of the couplings was measured experimentally. However, a quasi-static approach was followed, where the relative angular displacement of the coupling flanges was measured while applying incremental moments to one of the coupling flanges. The mean stiffness of the coupling flange was used. However, in the actual drivetrain, there is a pre-load torque on each coupling during rotation. The dynamic torsional stiffness of the coupling needs to be considered, which is not provided in the catalogue.

The gear mesh stiffness was estimated with an empirical relation in accordance with ISO 6336 (Appendix A). Uncertainty arose from the limited applicability of the standard. The standard assumes a straight gear tooth whereas the actual gear teeth are tapered. The face width of the gear at the root was used.

Table 3-2 describes the parameters of the LMM. The second column from the right presents the estimate of the rotational inertia or stiffness of the components.

Table 3-2: Description of the model parameters and estimates thereof.

Parameter	Description	Value	Unit
	Rotational inertia of …		
I_1	the WT rotor and half of the turbine shaft.	0.3180	$kg \cdot m^2$
I_2	half of the turbine shaft and half of the coupling.	0.4600×10^{-3}	$kg \cdot m^2$
I_3	half of the coupling and half of the small diameter section of the low-speed gearbox shaft.	0.3400×10^{-3}	$kg \cdot m^2$
I_4	all of the low-speed gearbox shaft except half of the small diameter section.	0.4034×10^{-3}	$kg \cdot m^2$
I_5	all of the high-speed gearbox shaft except half of the small diameter section.	0.2323×10^{-3}	$kg \cdot m^2$
I_6	half of the coupling and half of the small diameter section of the high-speed gearbox shaft.	0.3416×10^{-3}	$kg \cdot m^2$
I_7	half of the coupling and half of the small diameter section of the generator rotor.	0.3484×10^{-3}	$kg \cdot m^2$
I_8	all of the generator rotor except half of the small diameter section.	0.4261×10^{-2}	$kg \cdot m^2$

24

	Stiffness of ...		
k_1	the turbine shaft in torsion.	6.556×10^3	N·m·rad⁻¹
k_2	the low-speed coupling in torsion.	526	N·m·rad⁻¹
k_3	the low-speed gearbox shaft in torsion.	9.080×10^5	N·m·rad⁻¹
k_4	the gear mesh.	2.083×10^4	kN·m⁻¹
k_5	the high-speed gearbox shaft in torsion.	9.081×10^5	N·m·rad⁻¹
k_6	the high-speed coupling in torsion.	560	N·m·rad⁻¹
k_7	the generator shaft in torsion.	5.451×10^5	N·m·rad⁻¹

Equations of motion for the lumped mass system are formulated following the Lagrangian approach (Rao, 2011). Start with equation (3-2),

$$M\ddot{q} + C\dot{q} + Kq = T \qquad (3\text{-}2)$$

where

- $q = [\theta_1, \theta_2, \theta_3, \theta_4, \theta_5, \theta_6, \theta_7, \theta_8]^T$ are the degrees-of-freedom of the system in a column vector. Descriptions for the degrees-of-freedom are given in Table 3-3.
- M is the mass matrix of which the entries are rotational inertia.
- C is the damping matrix.
- K is the stiffness matrix.
- T is the vector that specifies the external torque applied to any of the bodies of rotation.

Table 3-3: Degrees-of-freedom of the LMM.

DOF	Angular displacement of the ...
θ_1	Turbine
θ_2	coupling on the turbine shaft
θ_3	coupling on the low-speed gearbox shaft
θ_4	22 tooth gear
θ_5	18 tooth gear
θ_6	coupling on the high-speed gearbox shaft
θ_7	coupling on the generator shaft
θ_8	generator armature

Since damping is assumed to be negligible, the equation of motion reduces to equation (3-3).

$$M\ddot{q} + Kq = T \qquad (3\text{-}3)$$

25

Equations of motion (EOM) for each of the rotating bodies are derived from free-body diagrams. The equations are given in Table 3-4.

Table 3-4: Equations of motion.

Degree-of-freedom	EOM
Turbine	$I_1\ddot{\theta}_1 = k_1(\theta_2 - \theta_1) + T_{aero}$
Turbine shaft	$I_2\ddot{\theta}_2 = -k_1(\theta_2 - \theta_1) + k_2(\theta_3 - \theta_2)$
Low-speed gearbox shaft	$I_3\ddot{\theta}_3 = -k_2(\theta_3 - \theta_2) + k_3(\theta_4 - \theta_3)$
22 teeth gear	$I_4\ddot{\theta}_4 = -k_3(\theta_4 - \theta_3) - k_4r_1^2\theta_4 - k_4r_1r_2\theta_5$
18 teeth gear	$I_5\ddot{\theta}_5 = k_4r_1r_2\theta_4 + k_4r_2^2\theta_5 + k_5(\theta_6 - \theta_5)$
High-speed gearbox shaft	$I_6\ddot{\theta}_6 = -k_5(\theta_6 - \theta_5) + k_6(\theta_7 - \theta_6)$
Generator shaft	$I_7\ddot{\theta}_7 = -k_6(\theta_7 - \theta_6) + k_7(\theta_8 - \theta_7)$
Magnetic rotor	$I_8\ddot{\theta}_8 = -k_7(\theta_8 - \theta_7) - T_{EMF}$

Mass and stiffness matrices, as well as the external torque vector are derived from the equations of motion, equations (3-4) and (3-5). The external torque vector T is a column vector, equation (3-6). T_{aero} is the aerodynamic torque on the turbine, causing the rotations of the drivetrain. T_{EMF} is created by the electromagnetic field and opposes the rotation of the drivetrain.

$$M = \begin{bmatrix} I_1 & & & & & & & \\ & I_2 & & & & & & \\ & & I_3 & & & & & \\ & & & I_4 & & & & \\ & & & & I_5 & & & \\ & & & & & I_6 & & \\ & & & & & & I_7 & \\ & & & & & & & I_8 \end{bmatrix} \tag{3-4}$$

$$K = \begin{bmatrix} k_1 & -k_1 & & & & & & \\ -k_1 & k_1+k_2 & -k_2 & & & & & \\ & -k_2 & k_2+k_3 & -k_3 & & & & \\ & & -k_3 & k_3+k_4r_1^2 & -k_4r_1r_2 & & & \\ & & & -k_4r_1r_2 & k_4r_2^2+k_5 & -k_5 & & \\ & & & & -k_5 & k_5+k_6 & -k_6 & \\ & & & & & -k_6 & k_6+k_7 & -k_7 \\ & & & & & & -k_7 & k_7 \end{bmatrix} \tag{3-5}$$

$$T = [T_{aero} \quad 0 \quad 0 \quad 0 \quad 0 \quad 0 \quad 0 \quad -T_{EMF}]^T \tag{3-6}$$

26

Vibration modes

An eigenvalue analysis of the mass and stiffness matrices produces the natural frequencies and mode shapes of torsional vibration. MATLAB's built-in eigenvalue solver, `eig.m` is used.

Figure 3-3 shows the vibration modes as calculated with the LMM. It is plotted as the participation of each degree of freedom relative to the maximum displacement. Note that, as expected, the first is a rigid body mode at 0 Hz. The gear stage with ratio of $1.\dot{2}$ causes the rotational displacements of DOFs 5 to 8 to be greater than DOFs 1 to 4, which explains the step in relative angular displacement. The second is at 32.35 Hz and the maximum angular displacement is that of the generator rotor. Maximum angular displacement moves to the low-speed gearbox shaft for the third mode, at 168.6 Hz. During the fourth mode the maximum deflection will be that of the gear tooth, at 624.7 Hz. Modes five to eight are at frequencies 1.131 Hz, 6.551 kHz, 12.96 kHz and 15.84 kHz.

The LMM provides mode shapes and frequencies of the first seven torsional vibration modes.
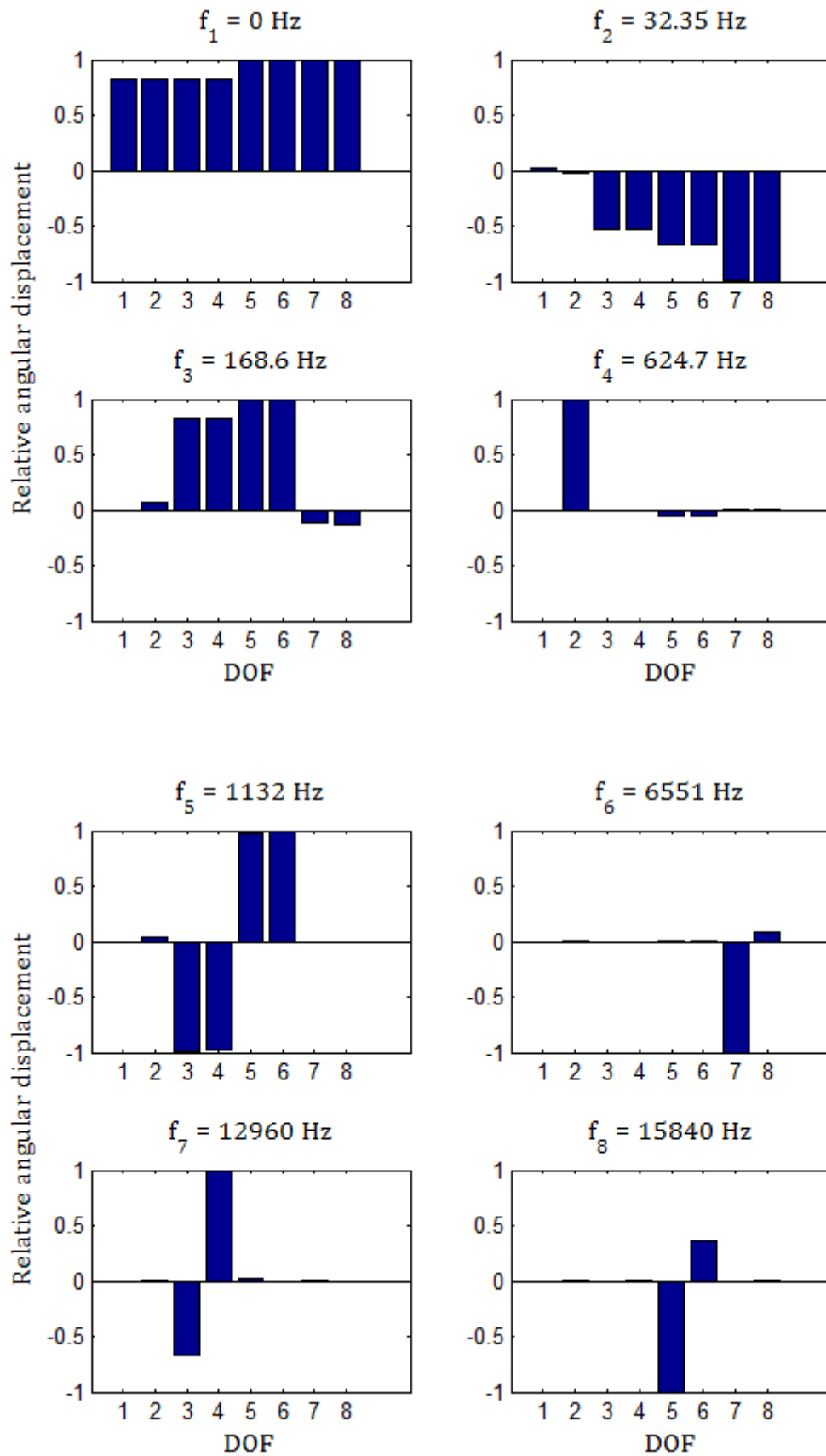
Figure 3-3: Mode shapes and natural frequencies of torsional vibration modes.

3.3 Finite element model

FEM requires accurate solid models and material properties of the drivetrain components. Such a model is able to not only estimate the torsional modes, but also the bending modes of the drivetrain. However, the estimation of the bending modes requires accurate estimates of the lateral stiffness of couplings and bearings, which is not in the scope of the current investigation. Many other components are simplified in order to reduce the number of finite elements. Proper boundary conditions represent the constraints on the drivetrain, such as bearings.

MSC Patran is used to prepare a FEM of the drivetrain and MSC Nastran is used to solve for the eigenvalues of the drivetrain. MSC Patran/Nastran was chosen because it was available and the author had prior experience with this software, even though there is commercial software which is better suited for rotor dynamic investigations.

3.3.1 Geometry and mesh

Figure 3-4 shows the mesh on the solid model of the drivetrain. Notice that detailed components such as the turbine rotor, bearings, couplings, gears and magnetic rotor are removed. Other features that were removed are:

- Fillets and rounds
- Grub screws
- Key grooves
- Retaining ring grooves
- Centre holes

All solid components are meshed with tetrahedral elements. An element edge length of 5 mm is specified. MSC Patran automatically refines the mesh where necessary.
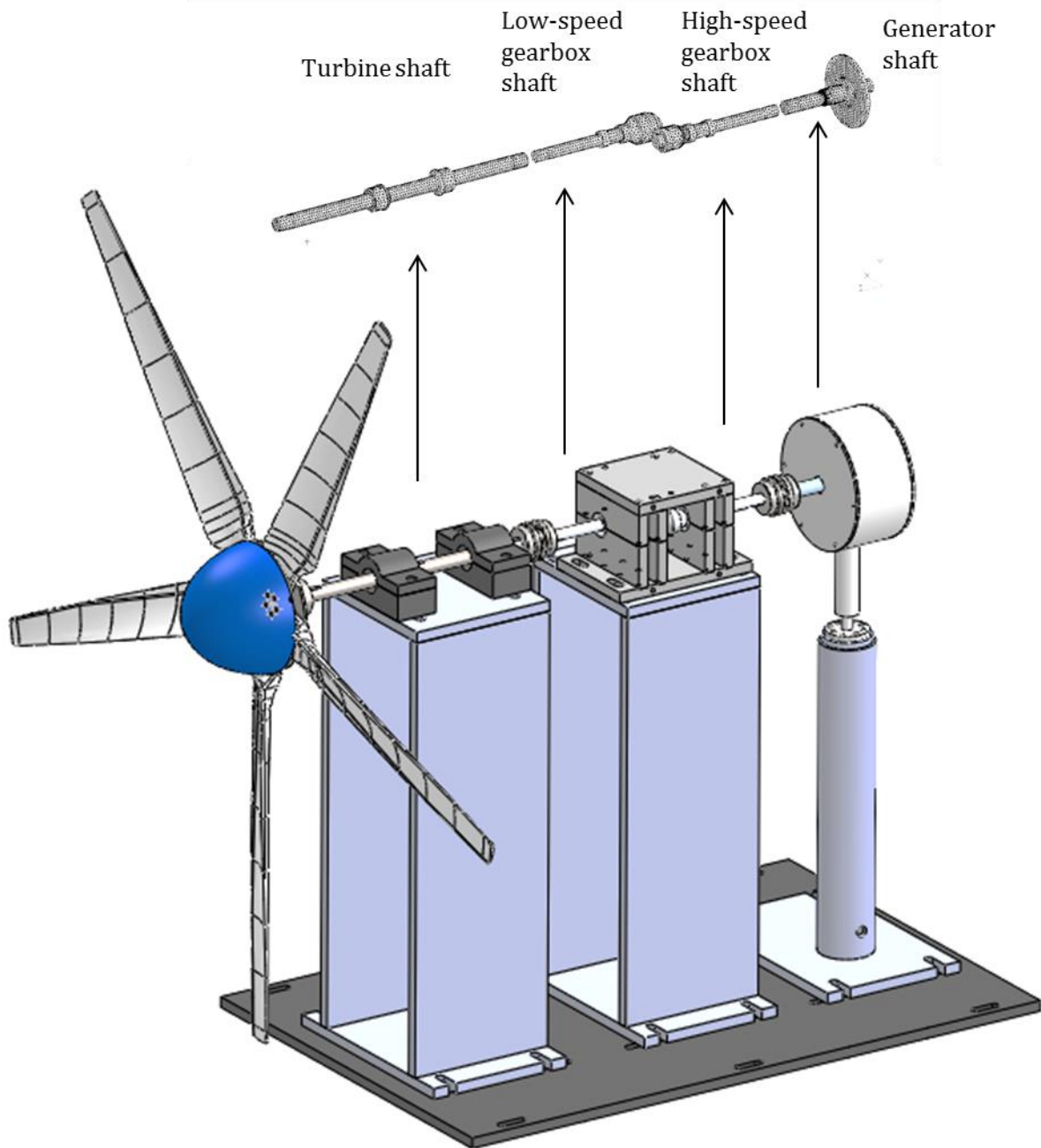
29

Figure 3-4: Mesh on the solid model of the drivetrain.

Several multipoint constraints (MPCs) are specified, shown in blue on the tetrahedral mesh in Figure 3-5. MPCs connect one dimensional bush elements and zero-dimensional mass elements to the tetrahedral mesh. Bush elements are also connected to the tetrahedral mesh through MPCs. All MPCs are rigid elements, in MSC Patran it is the RBE2 type.

Figure 3-5: Multipoint constraints on the mesh of the drivetrain.

The intricate solid model of the turbine subassembly is replaced by a zero-dimensional mass element, with similar mass and inertial properties. The mass element is placed at the centre of mass of the subassembly. An MPC connects the mass element to the tapered surface onto which the turbine boss fits. Figure 3-6 shows a part of the mesh of the turbine shaft. On the left hand side the MPCs are hidden and on the right hand side the MPCs are displayed in blue lines.

TURBINE MASS REPRESENTATION
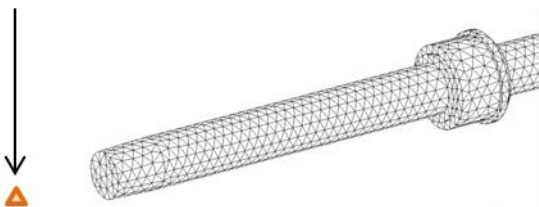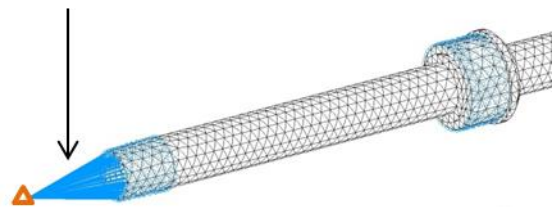
Figure 3-6: Mesh of the turbine shaft and the mass element that represents the turbine mass properties.

The bearings on the turbine shaft are self-aligning bearings. Figure 3-7 shows how the turbine shaft is constrained to represent these bearings. MPCs are used. Centre-nodes rigidly connect all of the nodes on the bearing surfaces. In MSC Patran, an RBE2 element is used. Zero-displacement is specified for each centre node, while it is free to rotate.
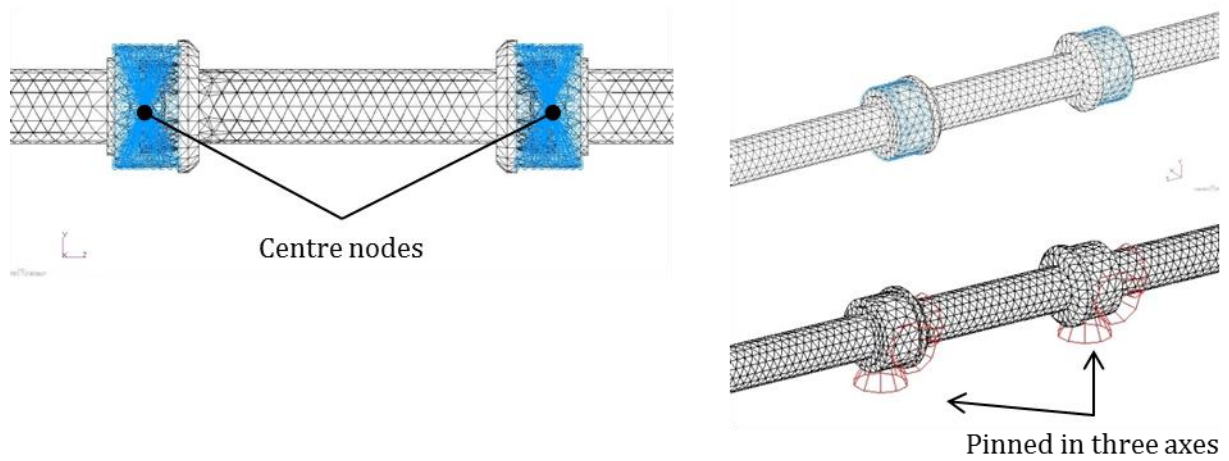
Figure 3-7: Multipoint constraints (top) and displacement constraints (bottom) representing the turbine shaft bearings.

Figure 3-8 shows how the gearbox shafts and the generator shaft are constrained to represent the bearings. At the locations of the bearings, the nodes on the surface are restricted from translating in a radial direction from the axis of rotation.
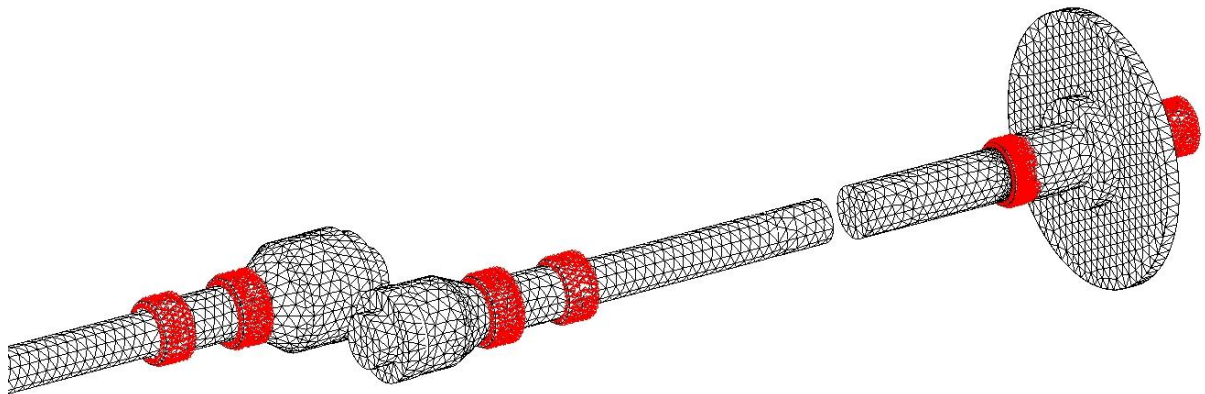

Figure 3-8: Constraining the gearbox shafts and the generator shaft.

Solid models of the coupling flanges are removed to reduce the number of elements and the complexity of the mesh, shown in Figure 3-9.

Zero-dimensional mass elements with similar mass and rotational inertia replace the coupling flanges. These mass elements are located at the centres of mass of each coupling flange. MPCs connect each mass element rigidly to the nodes on the surface of the shafts where the coupling

32

flanges fit on the shafts. MPCs also connect one-dimensional bush elements to the centre nodes. Torsional stiffness of the bush element is specified to match that of the coupling.
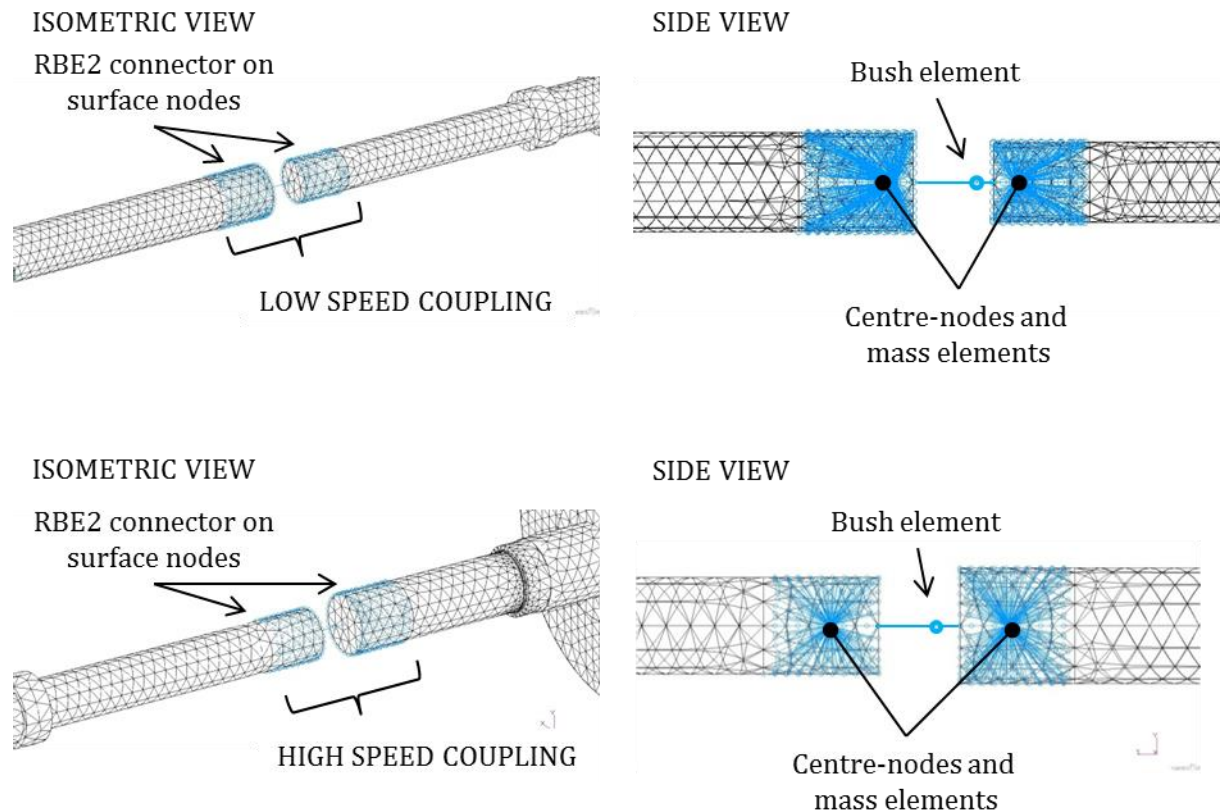

Figure 3-9: Couplings modelled as mass and bush elements connected to the mesh through MPCs.

Gears are replaced by solid disks with similar mass properties. The gear mesh stiffness is modelled as a linear spring, acting tangential to the pitch circle of both gears and at the pitch diameter. The linear spring is represented by a one dimensional bush element that is connected to the centre nodes of two MPCs, seen in Figure 3-10.

Note that the MPCs rigidly connect the surface nodes on the tetrahedral mesh. It is assumed that there is a rigid connection between the gear and the shaft and that all of the elasticity of the gear mesh can be represented with a linear spring.
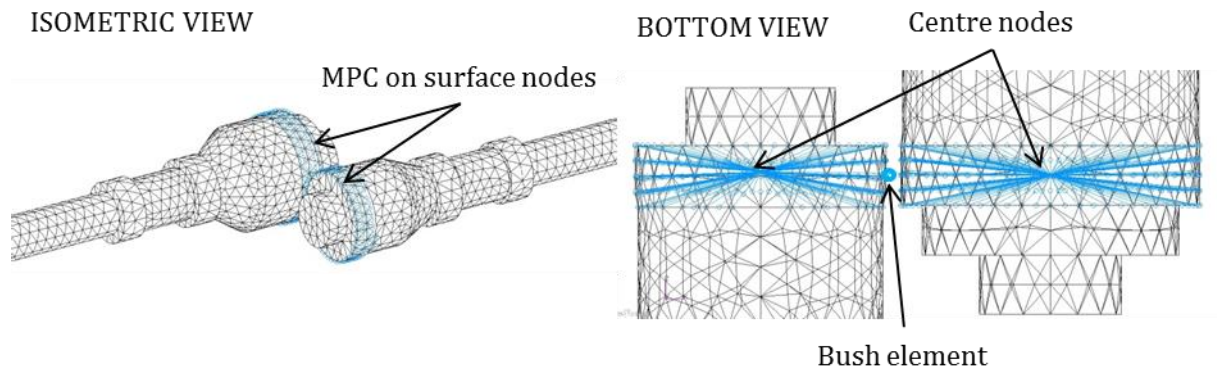
33

Figure 3-10: Gear mesh modelled as a bush element connected to the tetrahedral mesh through MPCs.

Similar to the turbine, the mass and rotational inertia of the magnetic rotor is represented with a zero-dimensional mass element and connected to the tetrahedral mesh through a rigid element MPC. Figure 3-11 shows the tetrahedral mesh of the generator shaft. The blue area on the left indicates the rigid elements connecting the surface to which the magnetic rotor is fixed to a centre node at the location of the magnetic rotor's centre of mass.
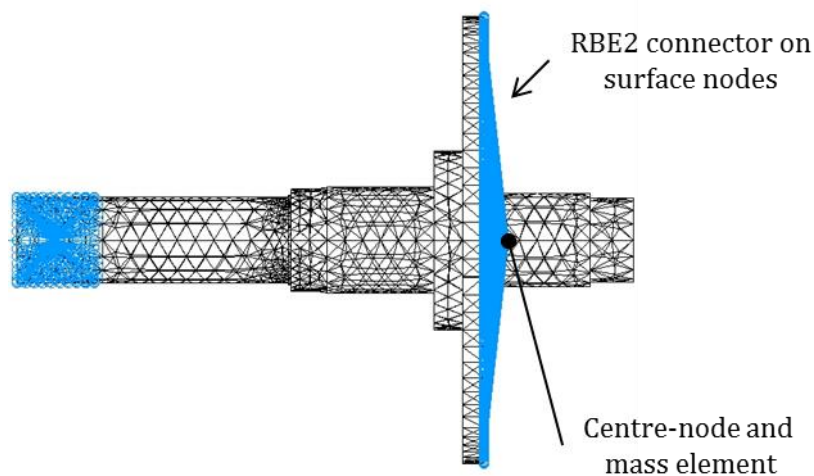

Figure 3-11: Magnetic rotor mass connected with a rigid element to the generator shaft.

3.3.2 Properties

Measured mass of the drivetrain components are given in Appendix B.

Table 3-5 shows the material properties that are used, in the consistent set of units for the finite element software. Nominal values for steel are used for Young's modulus and Poisson's ratio. Mass density was measured, as described in section 3.2, and rounded to the closest multiple of 100×10^{-12} Mg·mm^3.

Table 3-5: Material properties.

Part	Young's modulus, E [GPa]	Poisson's ratio, ν	Mass density, ρ [kg·m³]
Turbine shaft	200	0.3	7800
Gearbox shafts	200	0.3	7600
Generator shaft	200	0.3	7400

Mass and inertia properties of the turbine subassembly, couplings and the magnetic rotor are available from the mass properties tool in SolidWorks. These are the components that are replaced with zero-dimensional mass elements. Table 3-6 summarises the measured mass of the components and the estimated rotational inertia around three principal axes.

Table 3-6: Mass and inertia properties of the turbine, coupling flanges and the magnetic rotor.

Part	Mass [kg]	Rotational inertia [kg·m²]		
		I_{zz}	I_{xx}	I_{yy}
Turbine	5.681	0.3152	0.1616	0.1616
Coupling flange 1	0.5220	0.3175e-3	0.2129e-3	0.2137e-3
Coupling flange 2	0.5412	0.3200e-3	0.2093e-3	0.2098e-3
Coupling flange 3	0.5530	0.3221e-3	0.2100e-3	0.2095e-3
Coupling flange 4	0.5486	0.3231e-3	0.2261e-3	0.2250e-3
Magnetic rotor	817.7e-3	3.907e-3	1.966e-3	1.966e-3

Table 3-7 summarises the spring stiffness properties of the bush elements that model the stiffness of the couplings and the gear mesh. Note that there are six values of stiffness specified for each bush element: three values are linear along the principal axes and the remaining three are the rotational stiffness around these principal axes.

In the table, consider the stiffness of the bush element that represents the gear mesh. The element is oriented so that the linear spring constant along the z-direction is tangential to the pitch circle of the gear. The linear spring constants along the x and y directions and all the rotational spring constants are negligibly low.

In the same table, consider the spring constants of the couplings. Note that the linear spring constants are chosen so that the shaft ends are not free to translate without reaction at the couplings. Rotation around the x and y axes are much higher to model the coupling's resistance to rotate about axes other than the axis of shaft rotation.

Table 3-7: Bush element properties for the gear mesh stiffness and the couplings.

Part	Linear spring constant [kN·m⁻¹]			Rotational spring constant ×10⁻³ [kN·m·rad⁻¹]		
	x	y	z	rx	ry	rz
Gear mesh	1	1	2.08×10^4	0.001	0.001	0.001
Coupling 1	1×10^3	1×10^3	1×10^3	10 000	10 000	526
Coupling 2	1×10^3	1×10^3	1×10^3	10 000	10 000	556

3.3.3 Results

A normal modes analysis was run (MSC Nastran SOL103). Ten normal modes were calculated with the properties described in paragraph 3.3.2. The first is a rigid body mode, as expected. The frequencies and descriptions of the second to ninth modes, which include lateral and torsional vibration modes, are given in Table 3-8. Note that two gear mesh stiffness values are investigated. The values are 2.08×10^4 and 5×10^4 kN·m⁻¹. The lower value correspond to the instances when only a single pair of gear teeth are in contact, and the higher value correspond to the instances when two pairs of gear teeth are in contact.

Table 3-8: Frequencies and descriptions of the first ten non-rigid modes.

Mode description	Frequency [Hz]		
	$k_{gear\ mesh} = 2.08\times10^4$	$k_{gear\ mesh} = 5\times10^4$	% Difference
First torsional mode.	28.88	28.89	0.035
First bending mode pair.	37.66, 37.67	37.66, 37.67	0
Second torsional mode.	169.9	169.9	0
Second bending mode pair.	226.7, 226.8	226.7, 226.8	0
Third bending mode pair.	288.6, 288.8	288.6, 288.8	0
Third torsional mode.	693.0	693.2	0.014

Figure 3-12 illustrates the first three torsional modes of vibration. Colours indicate the relative rotational displacement, colder colours indicate less rotation and red indicates maximum rotation. For the first torsional mode the turbine shaft is stationary and the maximum rotation is that of the generator shaft and rotor, shown in red and yellow. For the second mode of vibration gearbox shafts rotate the most, and for the third torsional mode it is on the turbine shaft that the maximum rotation is found. This agrees well with the mode shapes calculated with the LMM.

36

Compare the torsional vibration mode frequencies of the FEM to that of the LMM. Notice that the first two modal frequencies agree well. The FEM estimates a much higher third torsional mode than the LMM.
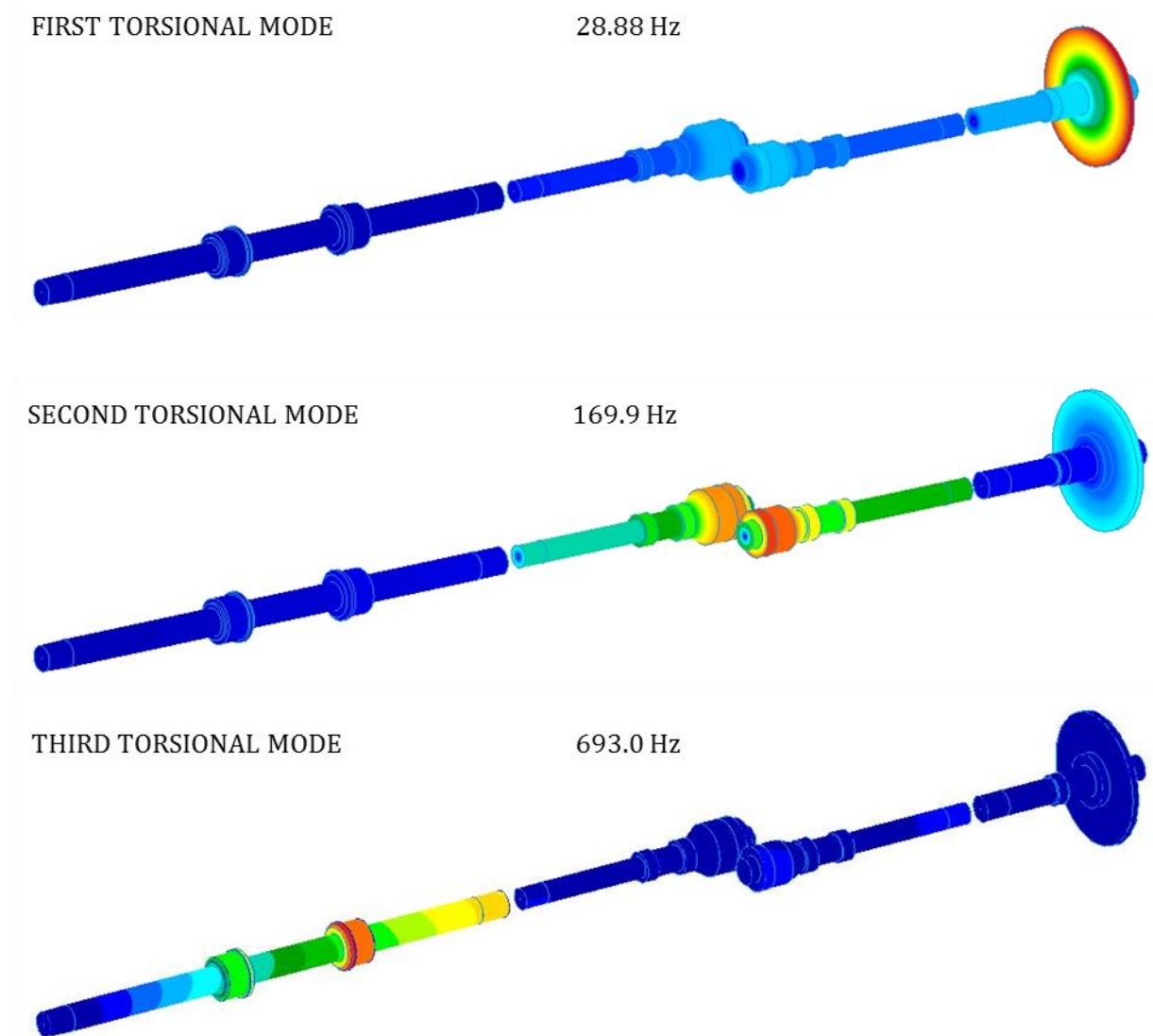
FIRST TORSIONAL MODE   28.88 Hz

SECOND TORSIONAL MODE   169.9 Hz

THIRD TORSIONAL MODE   693.0 Hz

Figure 3-12: Fringe plot of the first three torsional vibration modes.

3.4 Model verification

The LMM is verified by the FEM by comparing modal frequencies and torsional mode shapes. The LMM is able to correctly represent the first six mode shapes, but fails to determine the higher modes. See Table 3-9. As previously, the rotations of the drivetrain components are represented as bars with length relative to the component with maximum rotation. Length of a certain bar can also be seen as the relative amount of kinetic energy in that DOF. Notice that both models predict the same distribution of kinetic energy for Modes 1 to 6, which is not the case for the two remaining modes.

Mode 1 is a rigid body mode. The LMM correctly predicts equal rotation of components on the same side of the gear stage, with the generator-side rotating $1.\dot{2}$ times (the gear ratio) that of the turbine side. On the other hand, FEM mode 1 shows a larger difference in rotation. This is a numerical error which can be eliminated by using more significant numbers (three significant numbers were used to create the plot as these were readily available from the results display of the FEM software). See Appendix F.

Consider the ends of the four shafts as four DOF pairs: 1 - 2, 3 - 4, 5 - 6, and 7 - 8. Assumptions necessary for the discretisation of the drivetrain cause the shafts of the LMM to have a lower stiffness than the same shafts in the FEM. In every case, for the first eight torsional modes, the FEM predicts that the ends of a shaft rotate in the same direction. However, the LMM predicts that DOF pairs 7-8, 3-4, 5-6 rotate in opposite directions in Modes 6, 7 and 8, respectively.

Comparison of modal frequencies also suggests that the LMM is less capable than the FEM to determine the higher modes. See Table 3-9 and Figure 3-14. Notice the increasing difference in modal frequencies as the mode number increases.

In conclusion, both the LMM and the FEM are useful for estimating mode shapes and modal frequencies. The FEM is more accurate to calculate the higher modes due to a higher degree of discretisation, and therefore better geometrical representation. The LMM is useful for initial calculation of the modal frequencies and mode shapes. Even though the LMM is limited to calculating the lower-order modes, it is less time-consuming to create and to change.
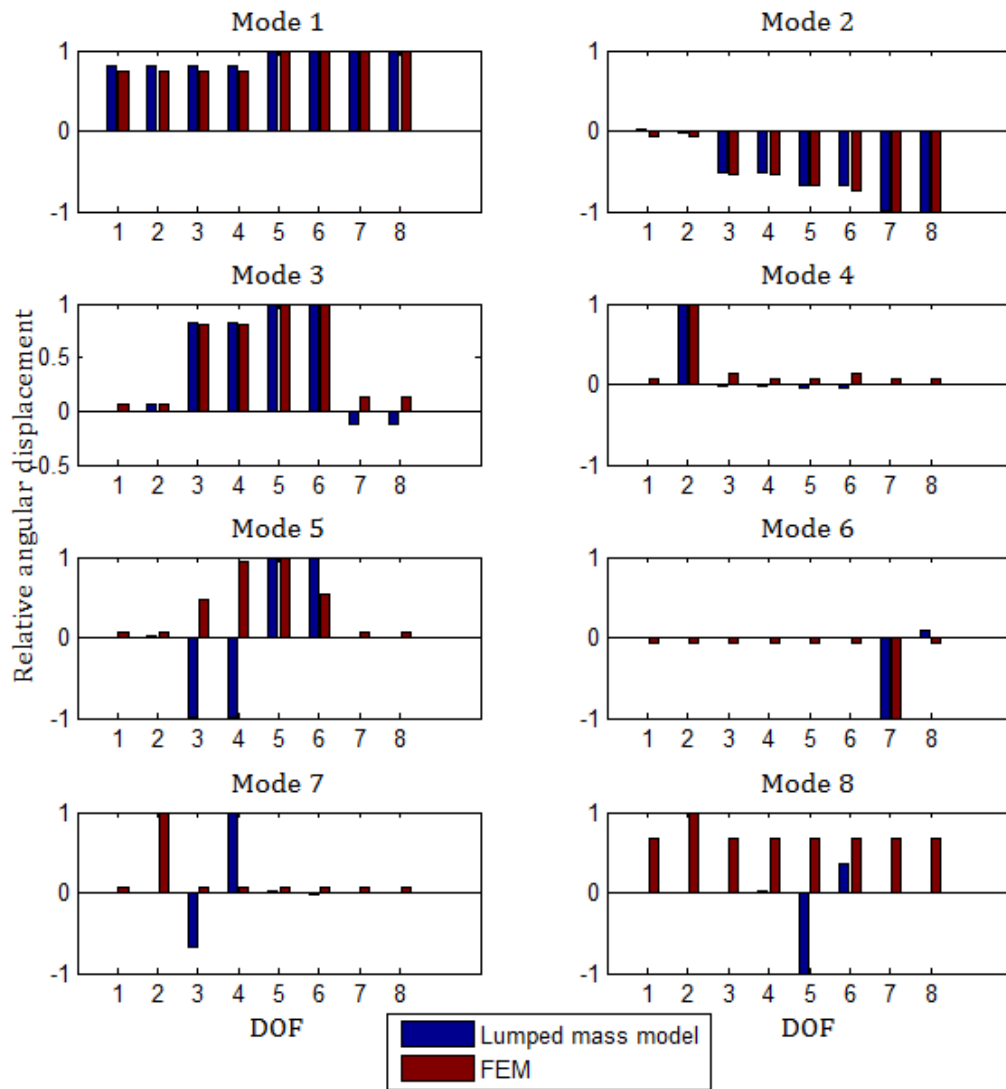
38

Figure 3-13: Visual comparison of the mode shapes.

Table 3-9: Frequencies of the first eight torsional modes.

Torsional mode	Modal frequency [Hz]							
	1	2	3	4	5	6	7	8
Frequency LMM	0	32.35	168.6	624.7	1132	6551	12960	15840
Frequency FEM	0.2740	28.88	169.9	693.0	1514	1646	2531	4772
Difference [%]	-	12.01	0.750	9.855	25.26	298.0	412.1	232.0
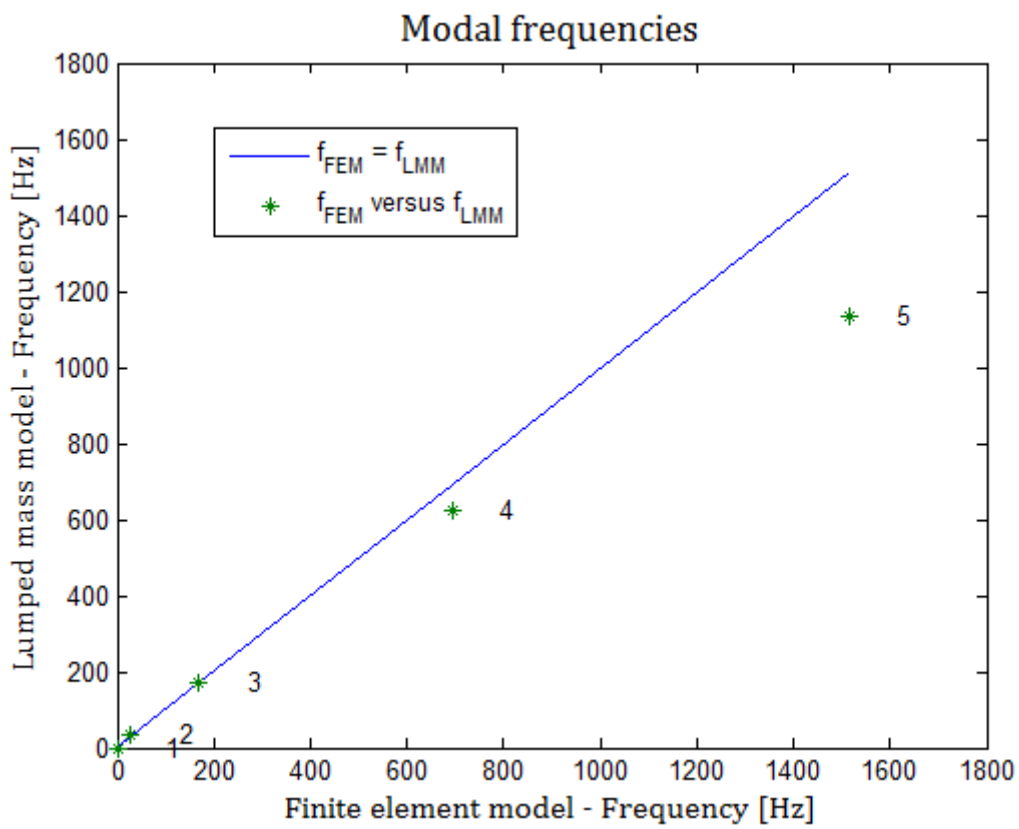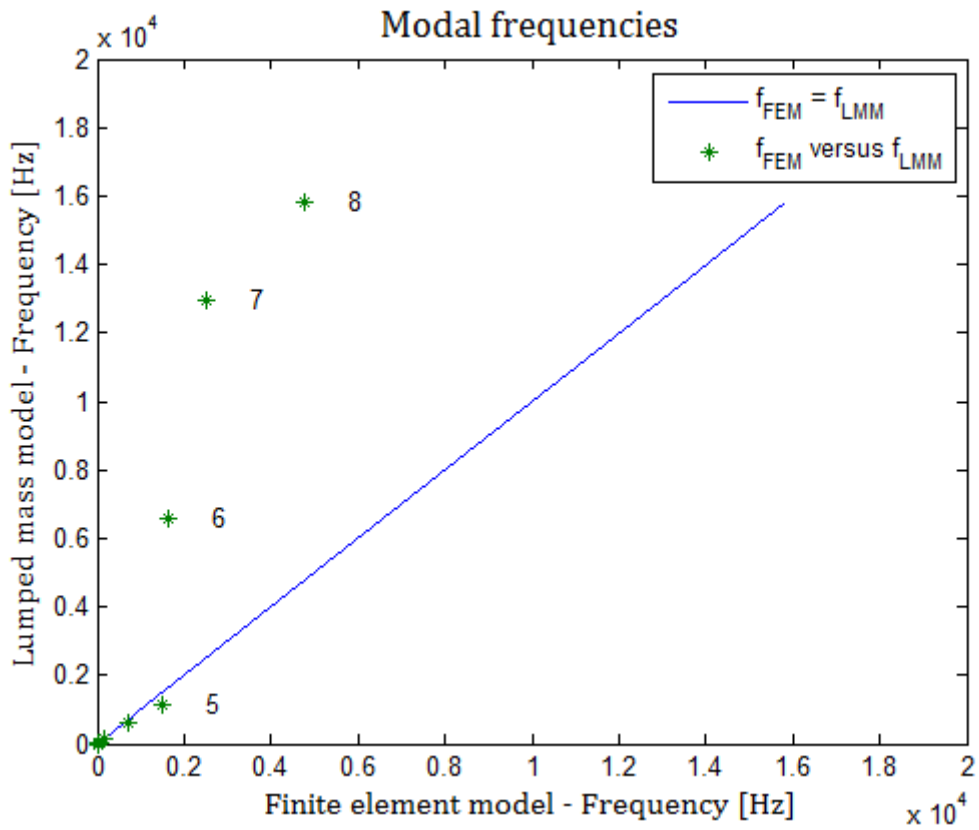
Figure 3-14: Comparison of all the torsional modal frequencies (top) and the first five (bottom).

4 Experimental dynamics

4.1 Introduction

In the previous section it is shown how modal frequencies are estimated with the use of two mathematical models, LMM and FEM. The LMM is able to estimate torsional modes while the FEM estimates bending modes as well. Frequencies and mode shapes of the lowest eight torsional modes are estimated and there is a good correlation between the lowest eight frequencies and mode shapes.

Since the mathematical models are parametric, it can be updated by comparison with experimental results. Experimentally measured frequencies and shapes are required. This chapter describes an experimental investigation of the wind turbine drivetrain; instrumentation, procedure and results are presented.

At the end of the chapter, the mathematical models of the previous chapter are revisited, this time with information on the measured torsional dynamics.

4.2 System dynamics

The experimental setup described in section 2 is a system which consists of the drivetrain components and its support structure. When the torsional vibration of the drivetrain components is measured it is kept in mind that the dynamics of the support structure exhibits on the measurements as well. Modal tests of the support structure were performed (described in Appendix G) and the findings were considered during the interpretation of data.

Another consideration to keep in mind is the physical characteristics of the drivetrain. The implication of the physical characteristics is torsional vibration at multiples of the rotation speed, and the associated harmonics.

Looking at the drivetrain, the following physical characteristic frequencies should be expected:

1. Rotation frequency, f, due to imbalance and rubbing.
2. In this case, the rotation frequency of the secondary section of the drivetrain, $1.\dot{2}f$.
3. Passing frequency of the five turbine blades past the support, $5f$, due to aerodynamic interference.

41

4. Meshing frequency of the 22 gear teeth on the low-speed side of the gearbox, $22f$.
5. Passing frequency of permanent magnets past stator coils in the generator, $1.\dot{2} \times 26f$.

Figure 4-1 illustrates some vibration modes of components that are in contact with the wind turbine drivetrain. Other vibrations are the natural vibration modes of test-setup components. Vibrations that are considered are those of the pedestals, wind turbine blades, and lateral vibration of shafts.
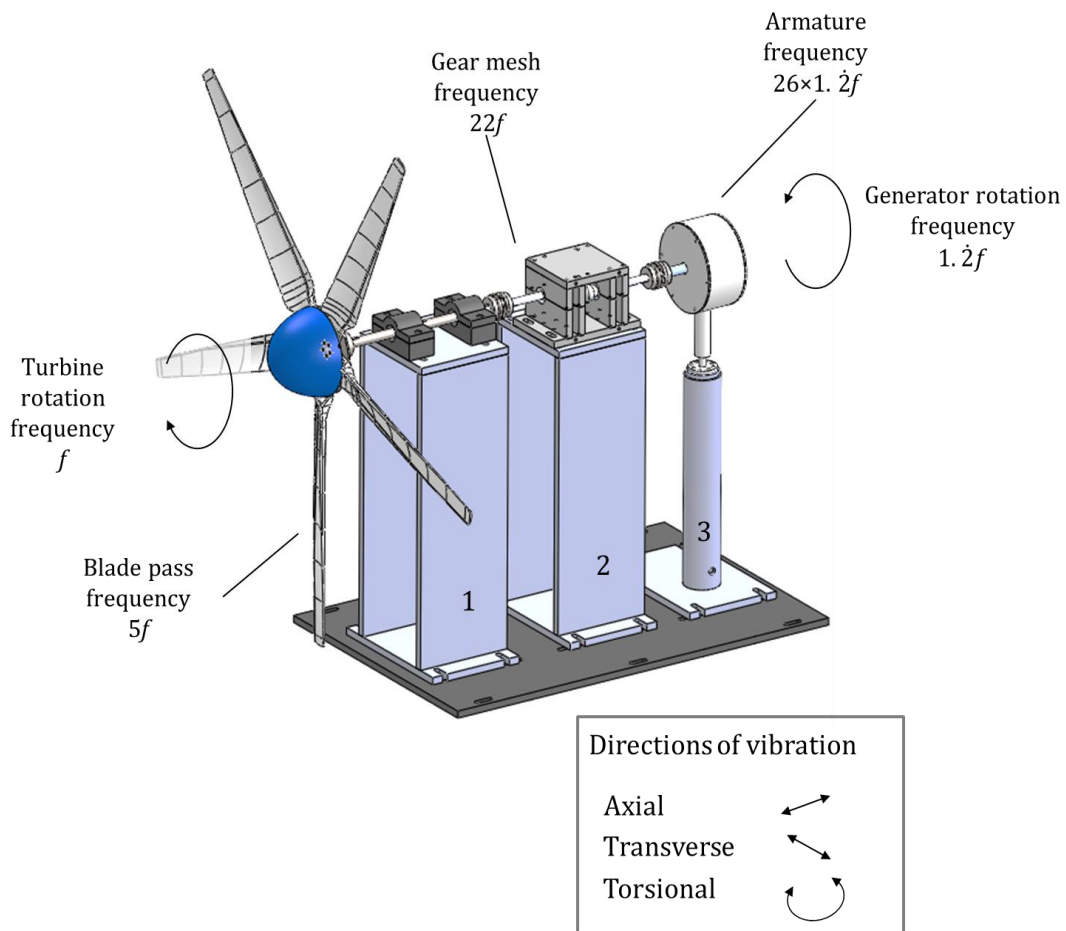

Figure 4-1: Vibration of the test-bench system.

To illustrate the armature frequency (point number 5 in the list before Figure 4-1) it is necessary to understand the internal components of the generator. Figure 4-2 is an exploded view of the internal components of the generator. Note that there are 26 permanent magnets in the rotor which pass the 12 stator coils to generate electricity. Consequently each magnet penetrates and leaves 26 magnetic fields during each rotation; hence a frequency of 26 times the rotation frequency is expected.
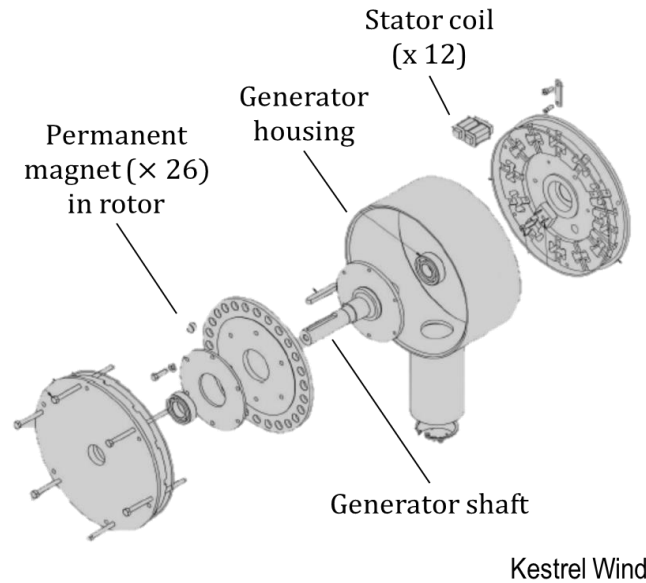
Figure 4-2: Exploded view of the generator.

Resonance frequencies were determined with Frequency Response Functions (FRFs). The FRFs are the results of modal impact tests. The tests entailed measuring the vibration of a structure after impacting the structure. Accelerometers were used to measure the vibration (response) of the structure, while a modal hammer equipped with a force transducer was used to excite the structural vibration.

Table 4-1 is a summary of the system frequencies illustrated in the figure above, that are expected to become visible during torsional dynamics measurement. Drivetrain characteristic frequencies are multiples of the design rotational frequency, which depends on both the power provided to the fan and the electrical load on the generator. The top section of the table assumes a turbine rotation frequency of 6.5 Hz and presents the corresponding frequencies and their harmonics. Peaks are expected at these frequencies in the data.

The characteristics of the fan described in 2.2.3 are also presented in the table. The rotation speed of the fan is 960 RPM, which equals 16 Hz. The fan was operated at approximately 70 % of the full rotational speed, which equals 11.2 Hz. Consider that the fan consists of three blades which passes close to the pedestal on which the fan is mounted. It is expected that the rotational speed of the fan will be affected when each blade passes the pedestal, resulting in airflow dynamics at the blade pass frequency of 3×11.2 Hz = 33.6 Hz.

43

The bottom section of the table presents empirical data of the natural frequencies of the setup vibration. Refer to Appendix G for the equipment and procedures of obtaining the natural frequencies. The left-hand-side column describes the vibration source or type; the middle column presents the frequencies at which peaks were noticed on the dataset referred to in the right-hand-side column. Peaks are expected to appear in the frequency spectra of the rotational vibration at the frequencies which are presented in the table. These peaks may be distinct or smeared, and can be expected to appear only if the relevant vibration mode is excited. These should not be mistaken to be natural frequencies of vibration.

Table 4-1: System characteristic and natural frequencies.

Description	Frequency [Hz]		
Drivetrain characteristic	**Fundamental**	**2nd harmonic**	**3rd harmonic**
Turbine design speed, f	6.500	13.00	19.50
Generator shaft, $1.\dot{2}f$	7.944	15.89	23.83
Blade-pass frequency, $5f$	32.50	65.00	97.50
Gear mesh frequency, $22f$	143.0	286.0	429.0
Armature frequency, $26 \times 1.\dot{2}f$	206.6	413.1	619.7

Fan detail	Frequency [Hz]	Datasheet
Blade pass frequency	33.6	Appendix D

Pedestal and direction of vibration	Resonant frequencies [Hz]	FRFs
Pedestal 1, Axial	10.00, 28.75, 35.00, 307.5, 653.8, 673.8, 780.0	Figure G-4
Pedestal 1, Transverse	91.25, 110.0, 120.0, 330.0,	
Pedestal 2, Axial	33.75, 247.5	
Pedestal 2, Transverse	6.250, 22.50, 30.00, 91.25, 105.0, 112.5, 127.5, 166.3, 311.3, 355.0, 405.0, 460.0, 600.0, 697.5, 717.5, 773.8	
Pedestal 3, Axial	47.50, 136.3, 160.0, 682.5, 760.0	
Pedestal 3, Transverse	17.50, 88.75, 125.0, 495.0, 582.5, 626.3,	

Blade vibration	Resonant frequencies [Hz]	FRFs
Rotation-plane	2.500, 23.75, 30.00, 33.75, 102.5, 215.0,	Figure G-8
Orthogonal to rotation-plane	286.3, 297.5, 408.8, 417.5, 437.5, 483.8	

Shaft in lateral vibration	Resonant frequencies [Hz]	FRFs
Turbine shaft	51.25, 97.50, 113.8, 218.8, 292.5, 460.0, 533.8	Figure G-10
Low-speed gearbox shaft	195.0, 747.5	
High-speed gearbox shaft	187.5, 697.5, 798.8	
Generator shaft	68.75, 341.3, 373.8, 633.8, 660.0, 668.8	

Before the measured data are presented, two phenomena noticed in the data are discussed. That is in subsections 4.2.1 and 4.2.3. Afterwards, in subsection 4.2.4, follows frequency spectra of rotational speed vibration according to the positions at which it was measured.

45

4.2.1   Instrumentation and procedure

Figure 4-3 shows the six locations at which rotational speed was measured. Number 2 indicates the position of a key groove in the shaft, across which a tachometer was placed. Shaft encoders were placed at all the remaining positions, measured with an optical sensor.
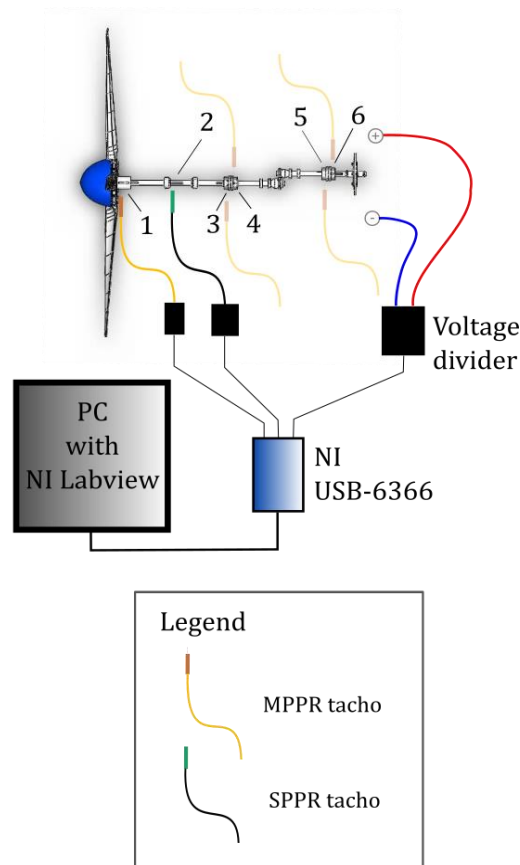

Figure 4-3: Torsional vibration measurement instrumentation.

Key groove tachometer

The first instrument is the single pulse per revolution tachometer (SPPR tacho) which was kept stationary at position 2. Figure 4-4 shows the proximity probe of the SPPR tacho in position, at the key groove in the centre of the turbine shaft. Rotational speed is determined from the time it takes for the key groove to pass, which corresponds to a single rotation. Average rotational speed for each rotation is calculated. Instantaneous rotational speed is not obtained with this instrument and no torsional dynamics is measured with it. This instrument was used only to control that the turbine is rotating as expected during the measurements.

46
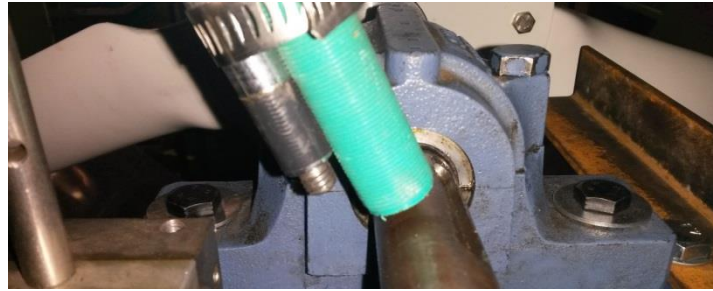
Figure 4-4: Proximity probe of the SPPR tacho.

Shaft encoder

Instead of acquiring a commercial encoder kit, available equipment and a newly developed algorithm was used to measure instantaneous rotational speed. This, the second instrument, is a multi-pulse per revolution tachometer (MPPR tacho), which was placed at position 1, 3, 4, 5, and 6 in Figure 4-3. Figure 4-5 shows the MPPR tacho at position 6, which is the coupling flange on the generator shaft. Note that a black-and-white 'zebra-strip' divides the flange circumference into approximately 1 mm segments. The optical probe, visible in the right-hand side picture with thread, is positioned close to the zebra-strip. It is an Optel Thevon optical sensor.
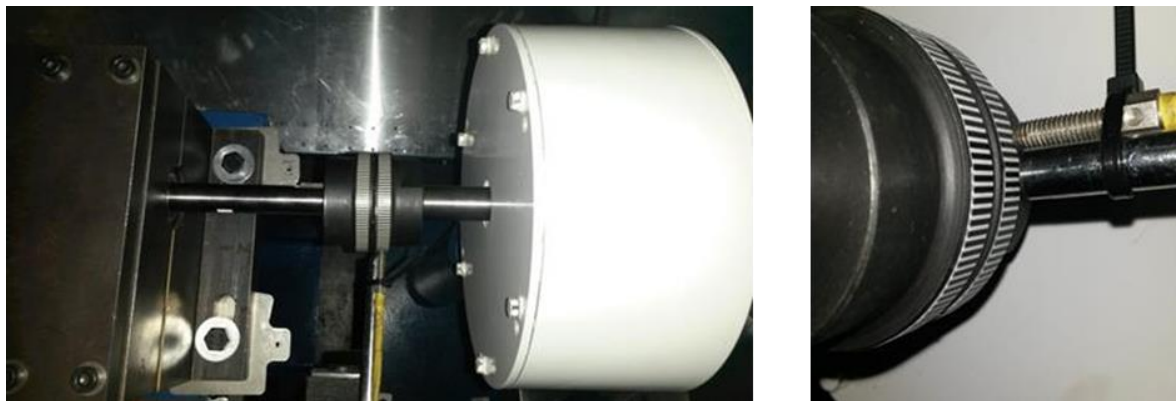
Figure 4-5: MPPR tacho at position 6.

Since the black and white stripes of the zebra-strip are not geometrically equally wide, signal processing is required. Shaft encoder compensation developed by Diamond et al. (2016) was used. This algorithm compensates for the variation of zebra-strip widths by comparing the signals recorded over a set number of revolutions and then statistically determining the actual arrival times (the time of transition from one segment to the next). The result is a multiple pulse per revolution tachometer signal. Further processing produces an instantaneous angular velocity signal with a selected sampling frequency, in this case 10 kHz.
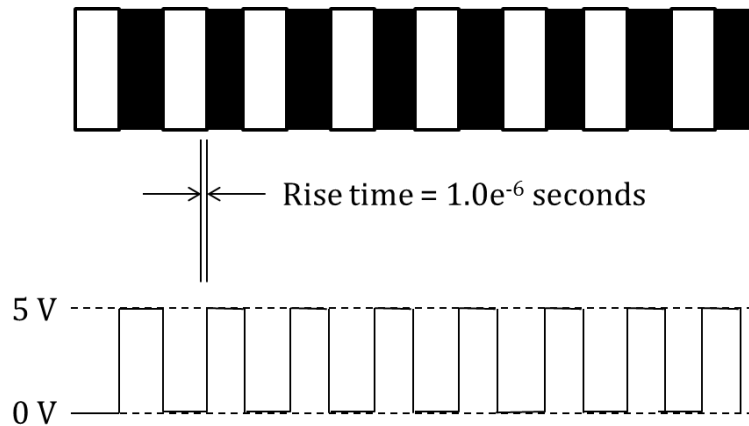
Figure 4-6: Output of the MPPR tacho compared to the zebra-strip.

Voltage measurement

A third instrument is created by measuring the voltage difference across the stator windings of the generator. Refer back to Figure 4-3, which shows the electrical connection between the generator and a 'voltage divider'. The circuit diagram of the voltage divider can also be seen in Figure 2-6. It is designed to have an output between 0 and 10 V, proportional to the voltage across the stator. This voltage is a function of the rotational speed and the physical interaction of the rotor and stator. The generator outputs a periodic power signal of which the shape varies in proportion to the instantaneous rotational speed. This power signal is analysed with a Fast Fourier algorithm to obtain its fundamental frequencies.

Data recording

Output from all three instruments was recorded on a PC through a National Instruments (NI) USB-6366 data acquisitioning (DAQ) system. NI Labview was used as an interface to start and stop recordings, selecting the sampling rate, and transferring the recorded signals to .MAT file-format for signal processing. A sampling rate of 1 MHz was selected. This rate is well within the capability of the DAQ system. Figure 4-6 shows the 0 – 5 V output from the MPPR tacho compared to the passing of the black-and-white segments. Notice that a maximum of $1.0e^{-6}$ seconds may pass from one segment to the next until the signal indicates this change. However, the rotational speed recorded with the zebra-strip is limited to the passing of black-and-white segments. The strip at position 1 has 94 back-and-white segments, whereas positions 3 to 6 have 108 segments. The number of segments corresponds to the number of rotational speed pulses that are available per revolution.

48

4.2.2 Peaks at harmonics of 32.8 Hz and 33.34 Hz

All of the rotational speed measurement data sets in the rest of this section show peaks at harmonics of 32.8 Hz. See Figure 4-7.
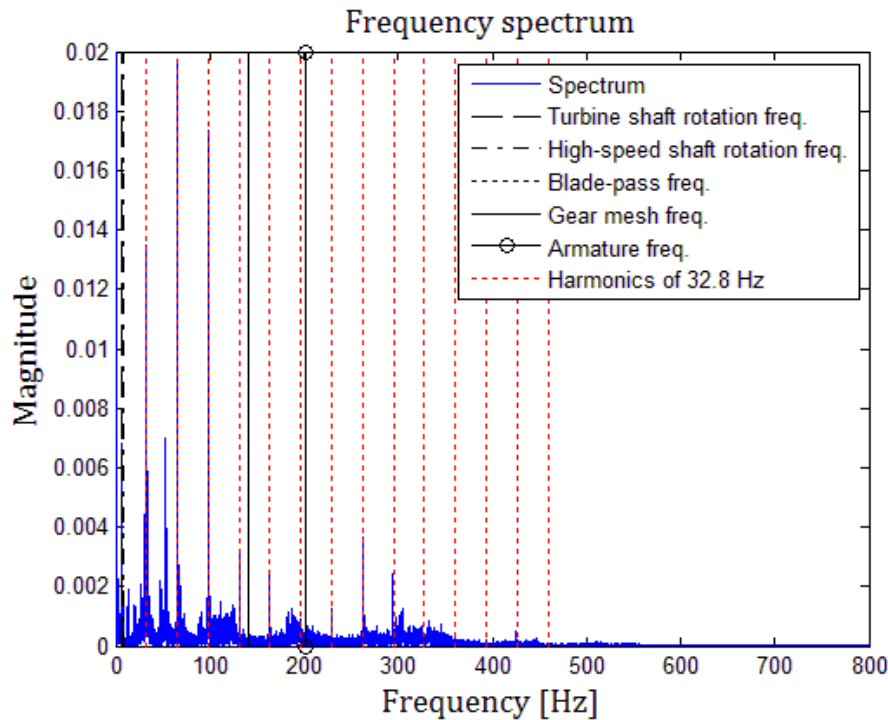

Figure 4-7: Example of a rotational frequency spectrum with several peaks visible at harmonics of 32.8 Hz.

However, the voltage measurement data shows peaks at harmonics of 33.34 Hz, for example Figure 4-8. Essentially the peaks are around 33 Hz, corresponding to the blade pass frequency of the fan (see 4.2). Fluctuations of this frequency cause fluctuations in the pressure difference across the wind tunnel, which influences the rotation speed of the wind turbine and drivetrain. This explains how similar peaks different to all of the other system frequencies appear in the measured data. Now that the origin is known these peaks are treated as an external influence and not mistaken as drivetrain characteristic frequencies. In one way these peaks are different to all the other peaks in the frequency spectra: the peaks are not smeared and without sidebands. This observation confirms that the peaks are not part of the wind turbine drivetrain and rather from an external source.
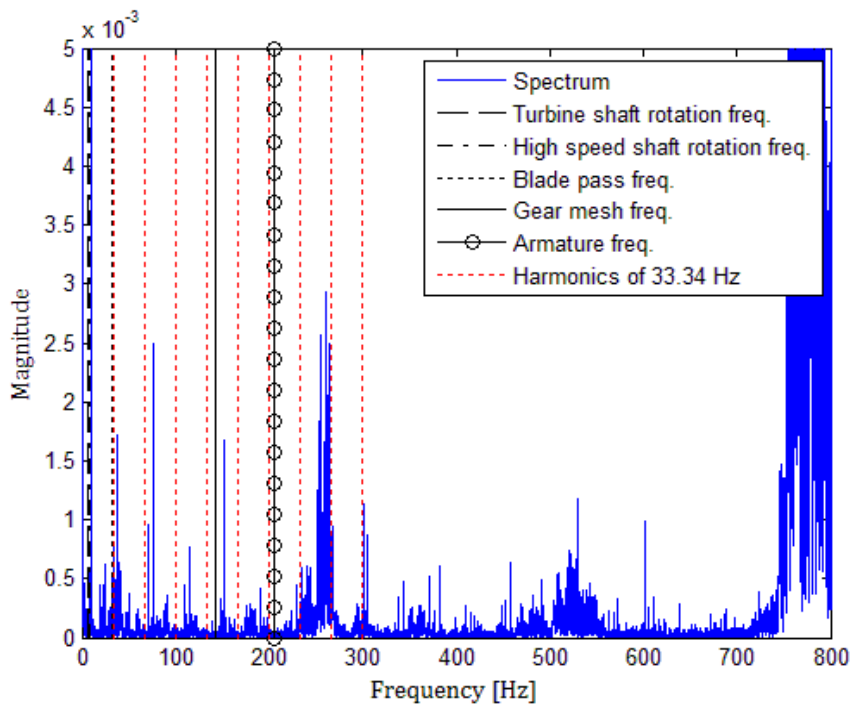
Figure 4-8: Example of a voltage spectrum with several peaks visible at harmonics of 33.34 Hz.

4.2.3 Sinusoidal fluctuations in the data

Figure 4-9 shows an example of sinusoidal fluctuations in the rotational speed. This is observed on the signals that were measured on two particular shafts: the high-speed gearbox shaft, and the generator shaft. Pay attention to the sinusoidal-shaped increase in rotational frequency between the 6th and 12th seconds.
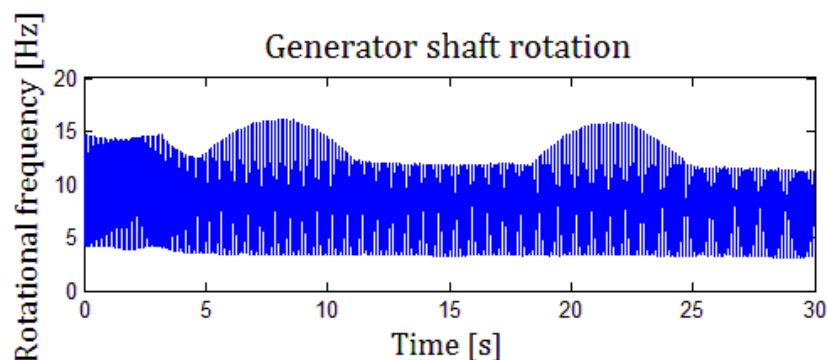

Figure 4-9: Measurement data which clearly illustrate the sinusoidal fluctuations in the data.

A close examination of the measured signal, Figure 4-10, shows that there are unnatural 'spikes' on the peaks of the measured signal. These spikes represent an increase in rotational frequency from approximately 10 to 15 Hz in a fraction of a second. Also notice that the rotational

50

frequency signal follows a sinusoidal shape. The sinusoid has a frequency of approximately 8.3 Hz and amplitude of 8 Hz.
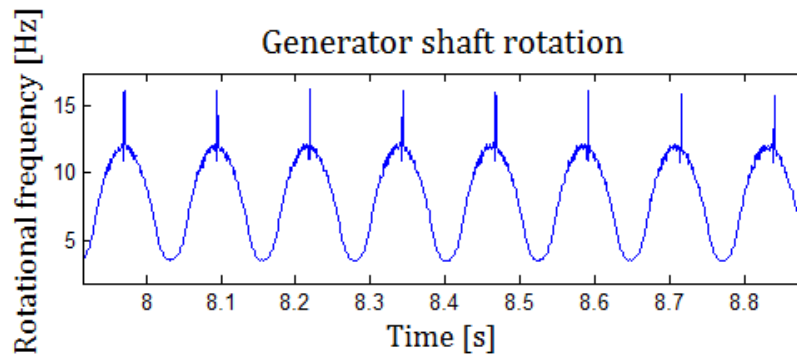

Figure 4-10: Enlargement of the measurement data that shows the unnatural 'spikes'.

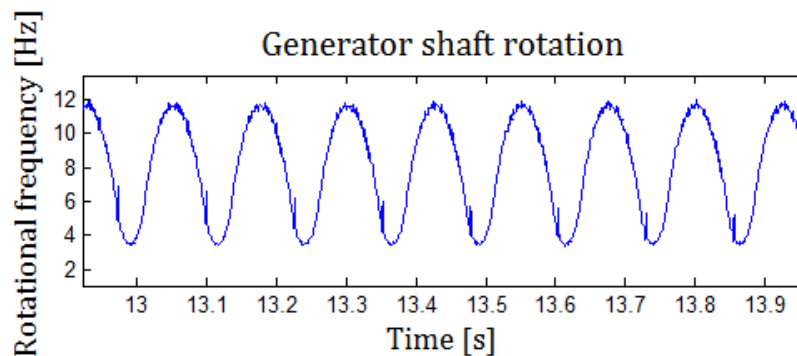Figure 4-11 shows the same spikes, this time in the troughs of the measured signal.

Figure 4-11: Enlargement of the measurement data that shows the same unnatural 'spikes'.

Investigation proves that the spikes originate from a numerical error since it is physically not possible for the drivetrain to undergo such rapid changes in rotational frequency. Also, the sinusoidal shape of the signal is not representative of the actual behaviour of the shaft, but rather of the shaft encoder geometry (the segment lengths which are calculated during compensation). See Figure 4-12, which compares shaft encoder geometries of all the shafts. Normal shaft encoder geometries are those of the turbine, turbine shaft and low-speed gearbox shaft encoders, where most segment lengths are similar with one longer segment where the encoder overlaps. Even if the sinusoidal shape of the segment lengths were an effect of the printed zebra-strip encoder, it is not supposed to influence the shape of the measured rotational speed. The error may have been caused by the different kind of zebra-stripe tape that was used, or a coding error that was not resolved.
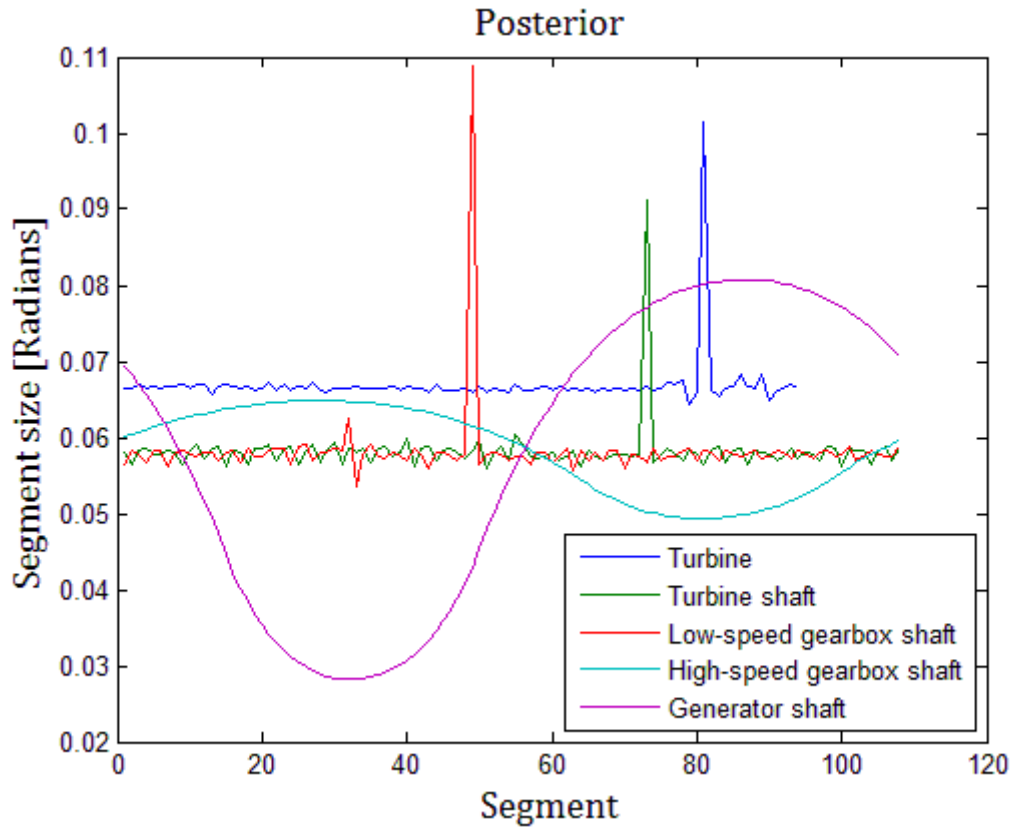
51

Figure 4-12: Comparison of the shaft encoder geometries calculated at various measurement locations.

From the comparison in Figure 4-12, it is clear that the calculated shaft encoder geometries of the high-speed gearbox shaft and the generator shaft are erroneous. This observation explains the shape of the rotational frequency. Fluctuations on the data are non-physical (therefore not propagating through the whole of the drivetrain), and the result of erroneous compensation of the shaft encoder geometries. Due to the erroneous compensation, the affected data are deemed unreliable and is not regarded any further for this investigation. In the following subsection however, some of the abovementioned data is presented and can be compared with other datasets.

4.2.4 Results summary

When measuring rotational speed with the shaft encoder, samples are taken each time when a pair of black-and-white stripes passes the optical sensor. Afterwards, during compensation, a higher time-resolution signal is obtained by interpolating with a high-order polynomial between the samples. The time-resolution of this new signal becomes the sampling frequency

52

and depends on the computing resources available to perform the interpolation. In this case, a sampling frequency of 10 kHz was selected.

Nyquist's criterion requires that the sampling frequency should be at least double the fundamental frequency of the period signal of interest. In this case the Nyquist frequency is 5 kHz. Therefore, vibration modes with frequencies up to 5 kHz can be identified from the data. However, in most data sets there are no peaks with significant magnitude above 500 Hz.

Although the LMM estimates the first four torsional mode frequencies below 5 kHz, due to the fact that the FEM estimates the first eight torsional mode frequencies to be below 5 kHz, the chosen range of interest is 0 – 5 kHz. Refer to Table 3-9 in section 3.4.

4.2.5 Rotational speed measurement

In this subsection experimental data of rotational speed are presented. The results show that drivetrain characteristic frequencies such as the rotational frequency, blade pass frequency and the magnetic pole frequency are visible when measuring the rotational speed with the multi-pulse per revolution tachometer.

Datasets in this subsection are presented according to the component in the drivetrain at which it was measured. There are five positions at which a shaft encoder was placed. These positions are:

> Position 1: Turbine
> Position 2: Turbine shaft
> Position 3: Low-speed gearbox shaft
> Position 4: High-speed gearbox shaft
> Position 5: Generator shaft

Position 1: Turbine

Figure 4-13 shows the measured rotational frequency signal and its frequency spectrum. As expected, the rotational frequency changes slightly with time due to the variations in the air speed. When looking at the frequency spectrum, note that all the peaks with significant magnitudes are below 500 Hz. An enlarged view of a portion of the frequency spectrum is shown in a following figure.
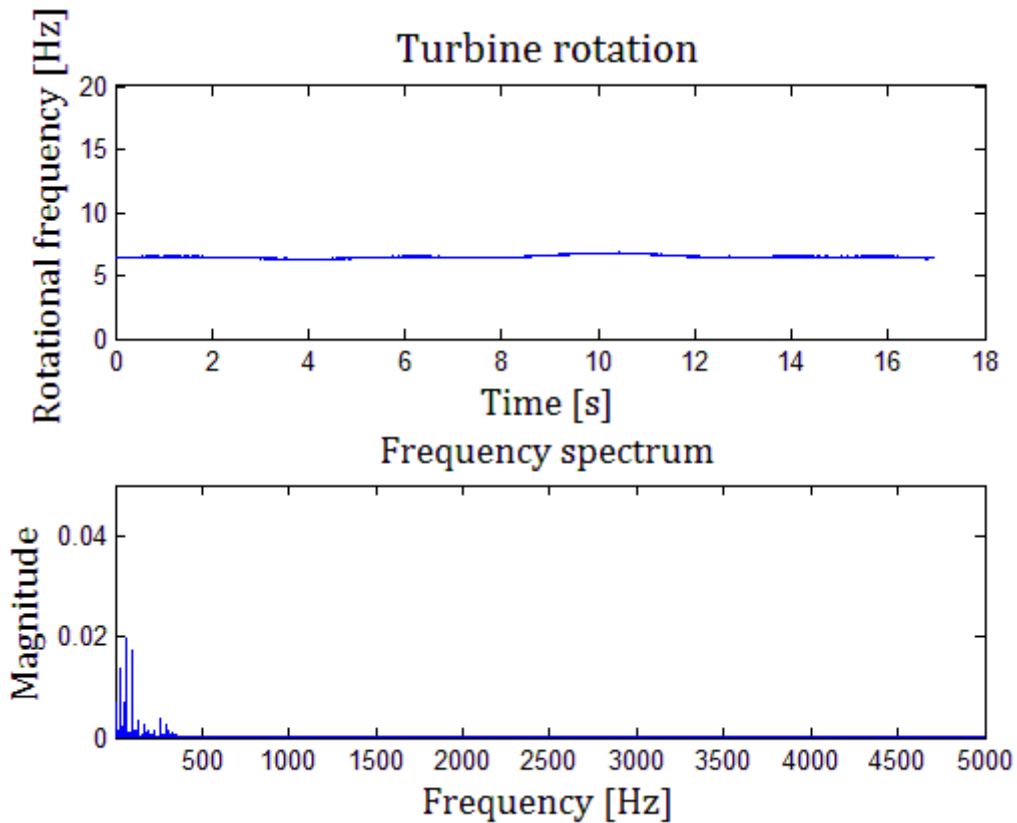
53

Figure 4-13: Turbine rotation measured with a maximum electrical load.

Figure 4-14 below shows a cropped portion of the first 800 Hz of the frequency spectrum. The following characteristic frequencies, marked with vertical lines, have corresponding peaks: the two shaft rotation frequencies, the blade-pass frequency, and the armature frequency. Peaks are smeared due to the slight variations in the rotational frequency which is due to the nature of the airspeed. The peak at the armature frequency is not as prominent as the lower frequency peaks due to the damping through the drivetrain. There is modulation of the blade pass frequency (which is five times the turbine rotational frequency) and the harmonics of the shaft rotation frequency. At the gear mesh frequency there is no peak. This characteristic dynamic frequency is damped out by the drivetrain components, especially the rubber couplings. Note that the fan blade pass frequency of 32.8 Hz and its harmonics are clearly present.
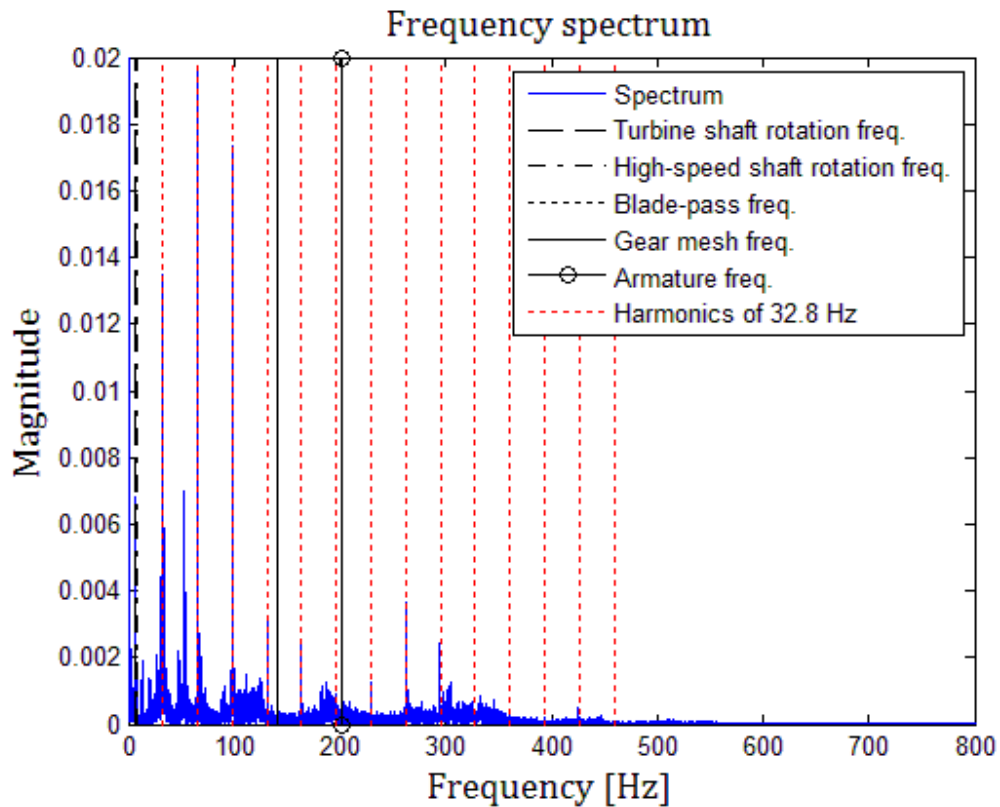
54

Figure 4-14: Enlarged view of the frequency spectrum of the rotation frequency measured at the turbine.

Peaks at frequencies that correspond closely to the estimated frequencies of the following vibration modes are also visible on the spectrum: Mode 2 (26.76 Hz), Mode 3 (163.7 Hz), and Mode 4 (670 Hz).

All characteristic drivetrain frequencies except the gear mesh frequency and three torsional vibration frequencies are visible when measuring the rotational frequency on the turbine, Position 1.

Pedestal, rotor blade and shaft vibration modes show as peaks on the above frequency spectrum. These peaks are close to the frequencies presented in Table 4-1. Vibration modes of the following components are identified at the frequencies given in brackets: Transverse and axial vibration of Pedestal 1 (90.56 Hz, 111.2 Hz, 33.75 Hz, and 247.5 Hz), rotor blade vibration in the rotation plane (2.441 Hz, 33.75 Hz) and orthogonal to the rotational plane (294.7 Hz) of the turbine blade and the vibration of the turbine shaft (111.1 Hz).

55

Position 2: Turbine shaft

The next measurement location is on the turbine shaft, at the other end of the shaft than the turbine is. An encoder was placed on the coupling flange, similar to the coupling shown in Figure 4-5. Figure 4-15 below shows the rotational frequency signal and its frequency spectrum. As for the previous measurement location, the significant peaks are below 500 Hz, even though the higher modes have frequencies above this frequency. Higher modes do not show on the frequency spectrum.
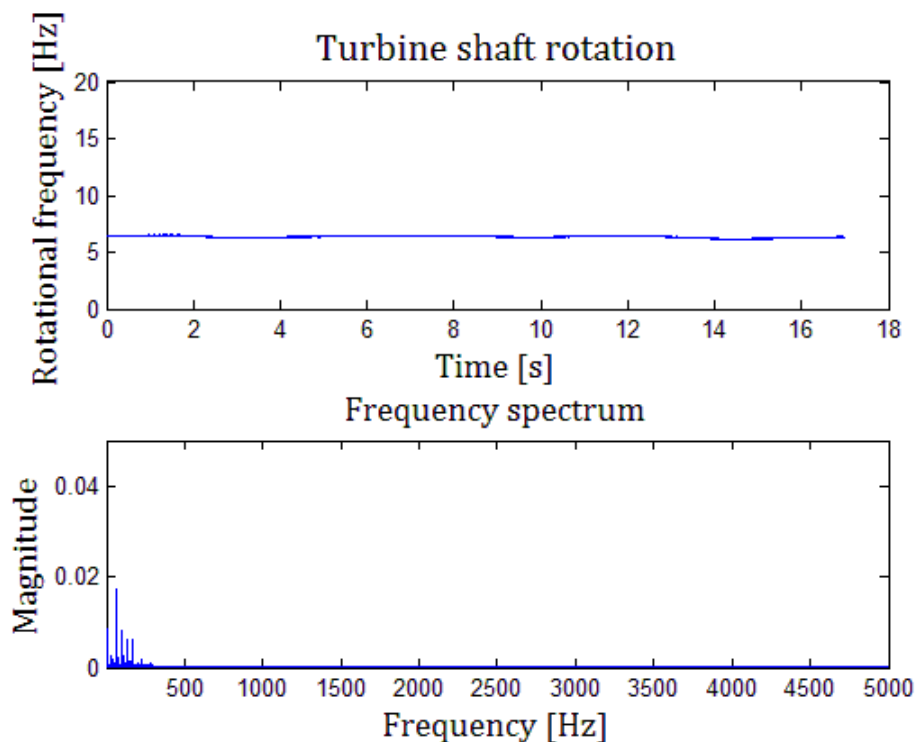

Figure 4-15: Turbine shaft rotation measured with a maximum electrical load.

In Figure 4-16, which is an enlargement of the frequency spectrum, note the characteristic drivetrain frequencies for which there are prominent peaks. There are prominent peaks at both shaft rotation frequencies, at the blade pass frequency and at the armature frequency. At the gear mesh frequency there is no peak, which shows that the vibration due to the gear mesh is also damped by the drivetrain components. There are peaks at some of the harmonics of 32.8 Hz, which is the blade pass frequency of the fan.

Very important, there are clear peaks at frequencies close to the frequencies of the following torsional vibration modes: Mode 2 (26.44 Hz), Mode 3 (164.1 Hz), and Mode 4 (758.2 Hz).

56

Position 2, on the turbine shaft is a useful measurement location as torsional mode frequencies and some of the drivetrain characteristics can be identified when measuring at this location.

On the frequency spectrum below, the following vibration modes are identified as peaks: transverse vibration of pedestal 1 (92.09 Hz), axial vibration of pedestal 2 (188.5 Hz, 111.2 Hz), turbine blade vibration in the rotation plane (2.67 Hz, 23.12 Hz, 29.53 Hz, and 102.0 Hz) and orthogonal to the rotational plane (283.5 Hz and 297.2 Hz). Vibration of the shafts is not recognised as peaks on the spectrum.
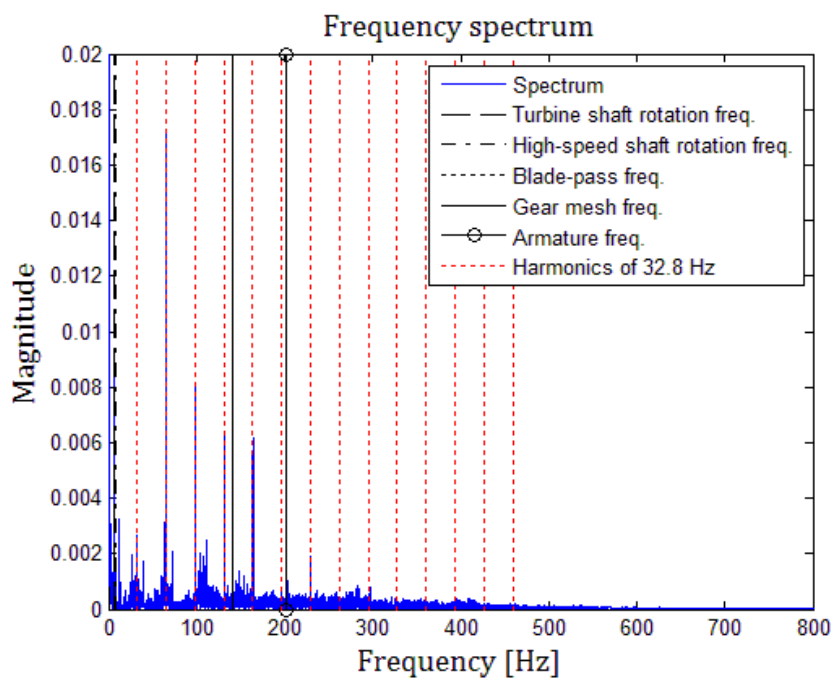
Figure 4-16: Enlarged view of the frequency spectrum of the rotation frequency measured at the turbine shaft.

Position 3: Low-speed gearbox shaft

The third position at which the rotational frequency was measured with the use of a shaft encoder is the low-speed shaft of the gearbox. Figure 4-17 is the rotational frequency signal recorded at this position as well as the frequency spectrum of this signal. Looking at the frequency spectrum in this figure it is clear that, as previously, the significant peaks are below 500 Hz.
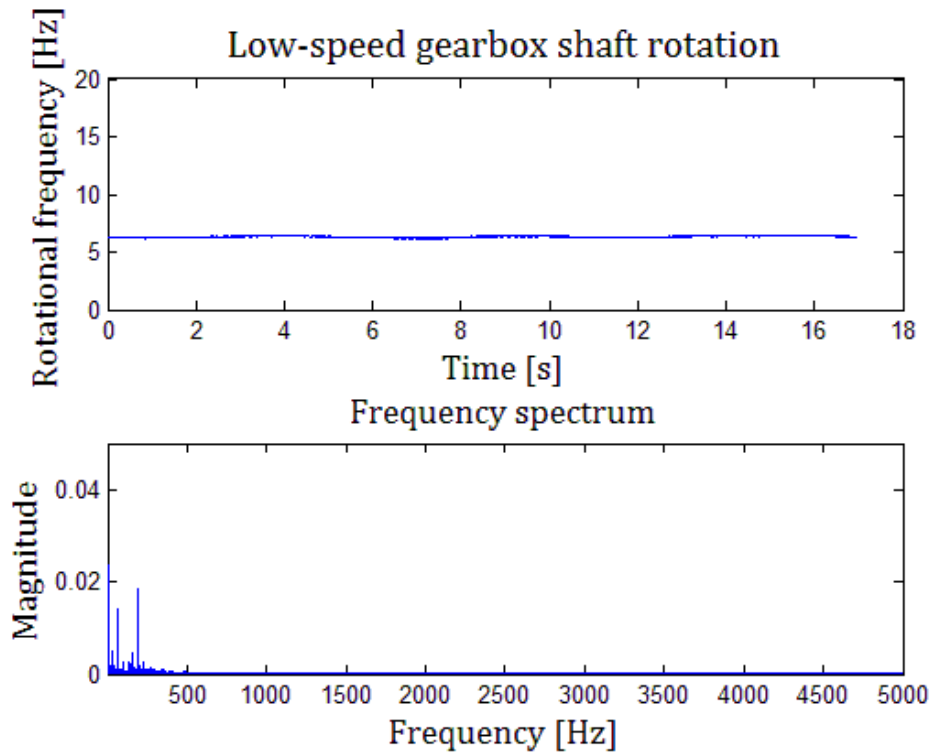
Figure 4-17: Low-speed gearbox shaft rotation measured with a maximum electrical load.

Below, Figure 4-18 is an enlargement of the lower 800 Hz of the frequency spectrum. On this spectrum there are peaks at the following characteristic drivetrain frequencies: shaft rotation frequencies and harmonics, turbine blade pass frequency, and the armature frequency. There is no clear peak at the gear mesh frequency. However, the harmonics of the shaft rotation frequencies close to the gear mesh frequency are larger than the peaks at the surrounding harmonic frequencies due to modulation. Several peaks show on harmonics of 32.8 Hz, the fan blade pass frequency.

In summary, measurement on the low-speed gearbox shaft provided the following information: shaft rotational frequencies, blade pass frequency, gear mesh frequency, armature frequency and the following frequencies of torsional vibration: Mode 2 (26.40 Hz), Mode 3 (163.1 Hz), and Mode 4 (756.8 Hz).

Axial and transverse vibration of pedestal 2 (33.42 Hz, 91.25 Hz, 105.6 Hz, and 405.0 Hz) is recognised on the vibration spectrum. On this spectrum a single vibration mode of the low-speed gearbox shaft is seen as a peak (195.0 Hz).
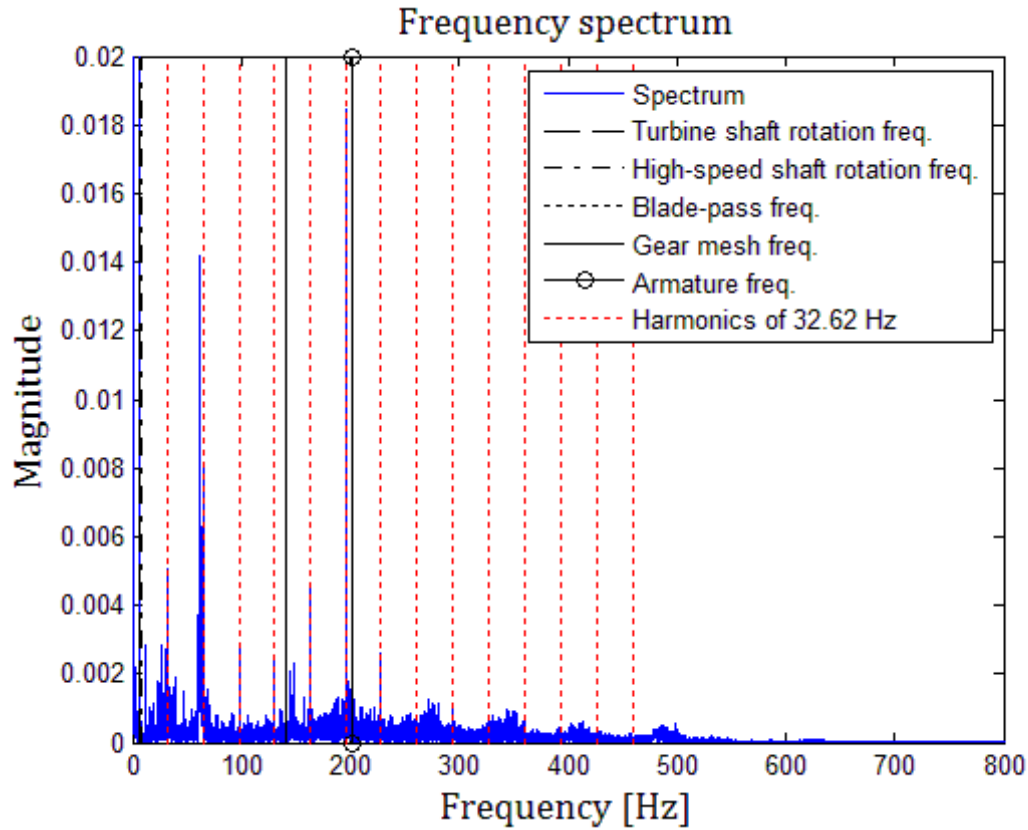
Figure 4-18: Enlarged view of the frequency spectrum of the rotation frequency measured at the low-speed gearbox shaft.

Position 4: High-speed gearbox shaft

Figure 4-19 below shows the rotational frequency signal measured on the high-speed gearbox shaft. As noted earlier, erroneous calculated shaft encoder geometry causes a sinusoidal shaped rotational frequency and discontinuities in the signal, which is physically highly unlikely. An enlarged frequency spectrum is also presented and discussed.
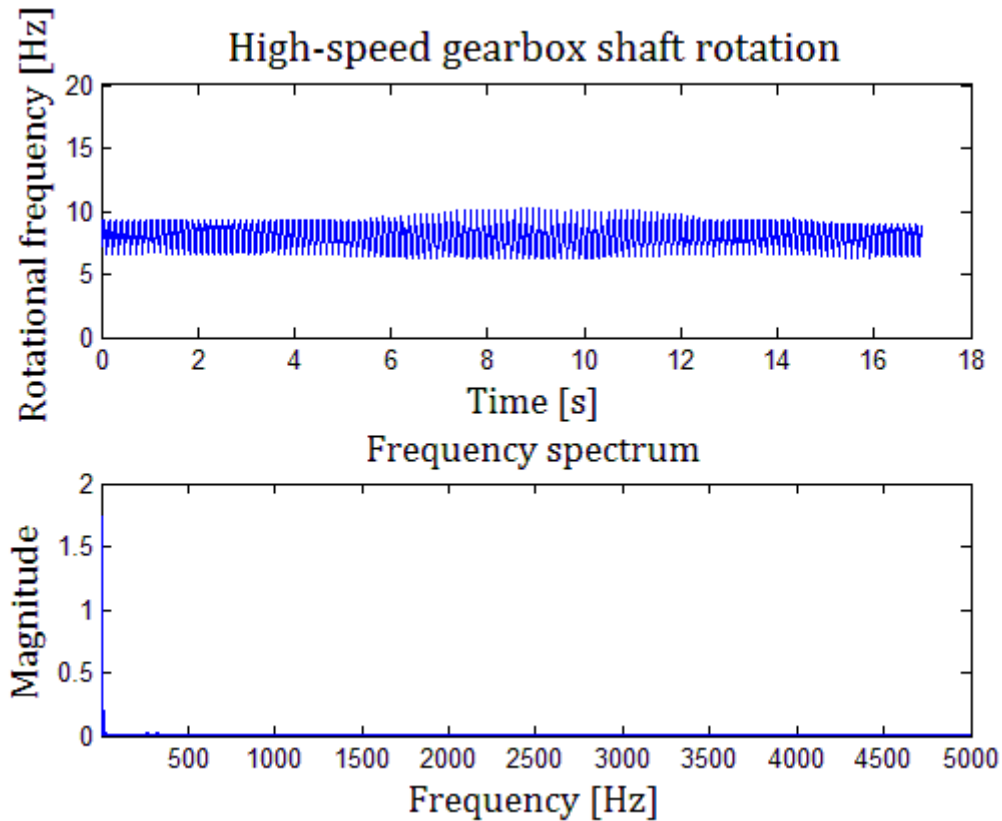
59

Figure 4-19: High-speed gearbox shaft rotation measured with a maximum electrical load.

Figure 4-20 is an enlargement of the frequency spectrum of the rotational frequency spectrum. Note that there are several peaks, as expected on the frequency spectrum of any signal with harmonic content. There are peaks that correspond to the 'average' rotational frequency, which cannot be established for certain due to malformed signal. Similar to the previous datasets, peaks occur at the harmonics of both the shaft rotational frequencies. In this case the smaller peak is in front of (at a lower frequency than) the larger peak. This is explained by the damping in the components between the measurement location and the low-speed shafts of the drivetrain. In the previous datasets the smaller peak was behind (at a higher frequency than) the larger peak.
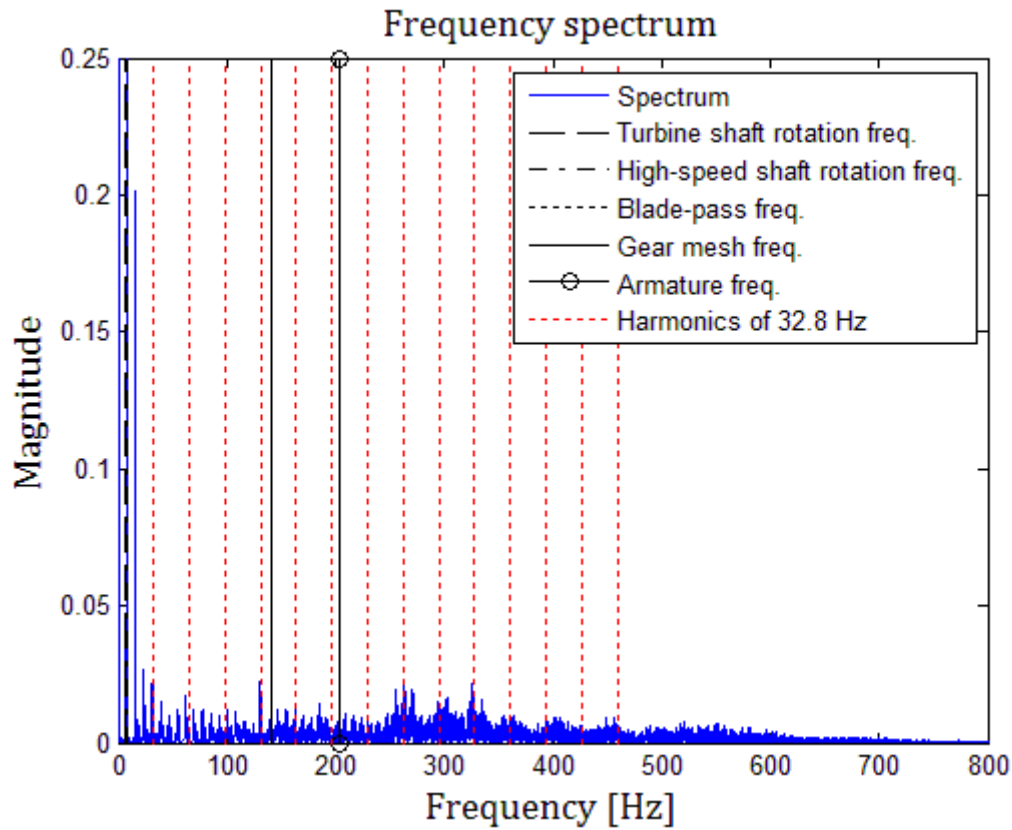
Figure 4-20: Enlarged view of the frequency spectrum of the rotation frequency measured at the high-speed gearbox shaft.

Position 5: Generator shaft

The fifth position at which rotational frequency was measured is directly on the generator shaft. The same error as in the previous dataset occurred which eliminates the usefulness of the recorded data. Figure 4-21 shows the signal and its frequency spectrum.
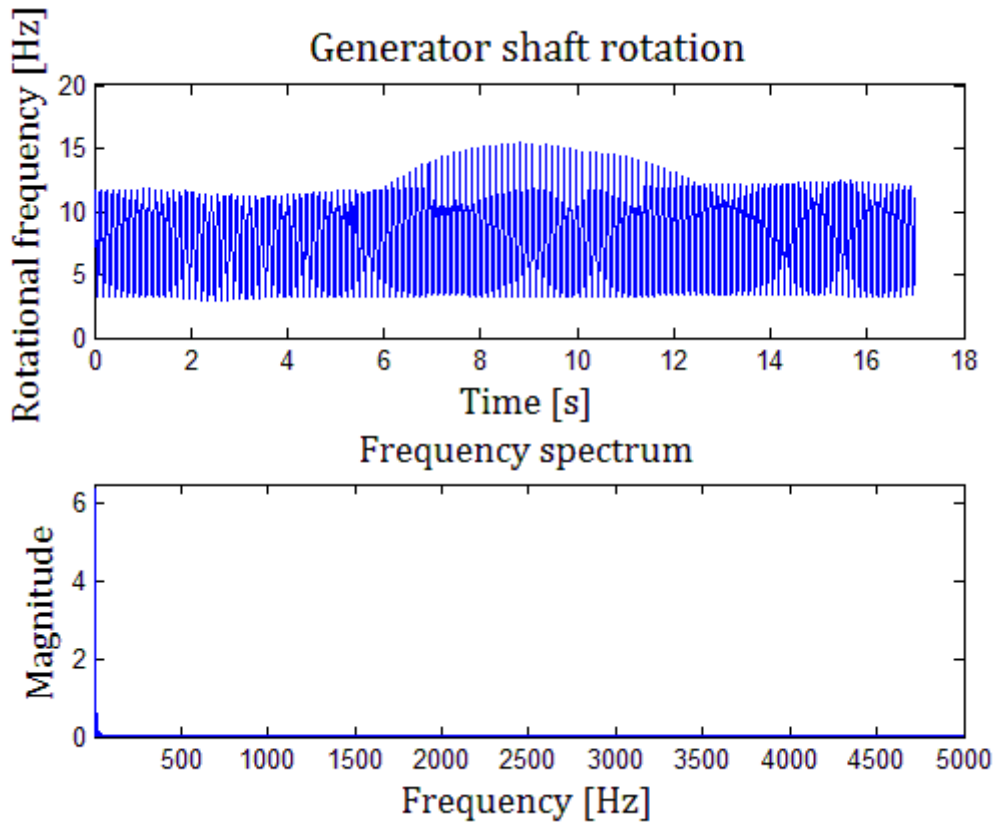
Figure 4-21: Generator shaft rotation measured with a maximum electrical load.

Below, in Figure 4-22 is an enlargement of the frequency spectrum. There is no correlation between the frequencies of the peaks in the spectrum and the drivetrain characteristic frequencies or the frequencies of the torsional vibration modes. This signal also lost physical relevance due to the erroneous shaft encoder geometry.
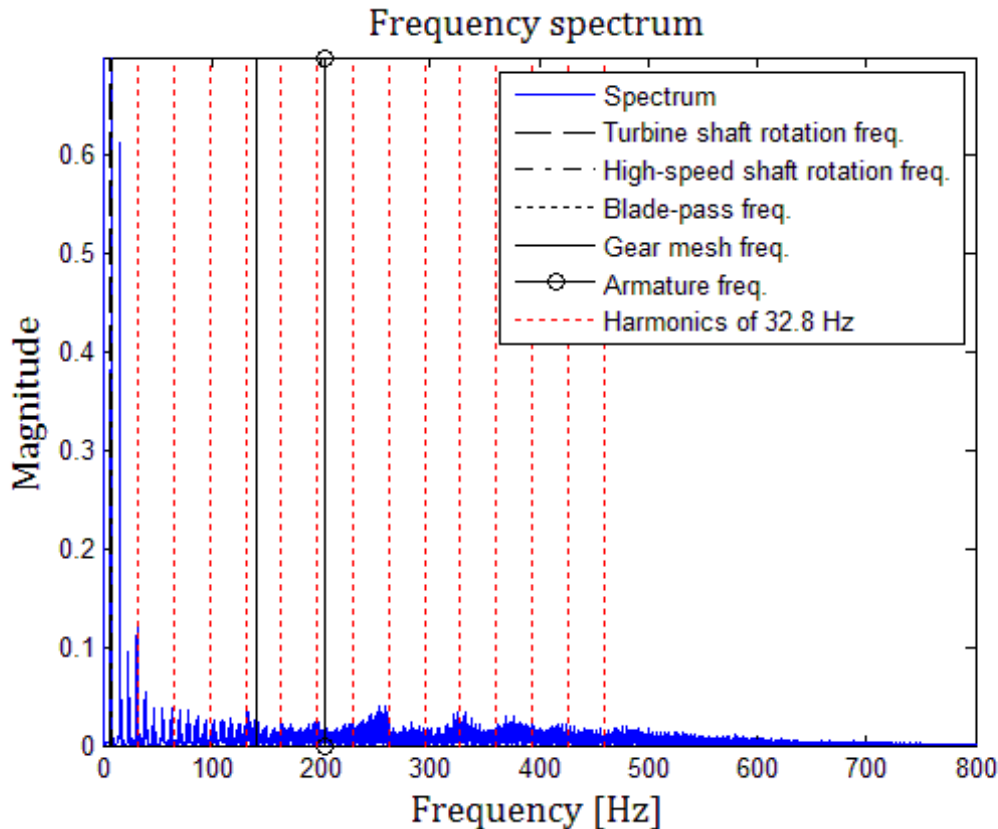
62

Figure 4-22: Enlarged view of the frequency spectrum of the rotation frequency measured at the generator shaft.

4.2.6 Voltage measurement

This subsection contains experimental data of the power signal generated. As for the rotational speed, the drivetrain characteristic frequencies such as the rotational frequency, blade pass frequency and the magnetic pole frequency can be identified from the power signal. Voltage samples were measured at a frequency of 2 MHz. To reduce the size of the datasets, the signals are resampled at a frequency of 10 kHz, using the `resample` function in MatLab. This function uses an antialiasing filter during compensation. As with the shaft encoder; the Nyquist frequency of the power signal is half of the resampling frequency, which equals 5 kHz.

Data from the following three load cases are presented:

Load case 1: Maximum power
Load case 2: Minimum power
Load case 3: Step in power

63

Voltage, *V*, not power, *P*, was measured. Current, *I*, depends on *V* and the load resistance, *R*. However, *V* and *P* are directly proportional through the following relation:

$$P = I \times V$$

Also, *V* is directly proportional to the rotational frequency of the generator.

Table 4-2 below precedes the presentation of the actual data and is a summary of the observations made from the data. Three load cases were selected: maximum, minimum and stepped electrical load. Electrical load is inversely proportional to the electrical resistance.

Table 4-2: Summary of the drivetrain characteristic frequencies and torsional natural frequencies identified in the data.

	Max. load	Min. load	Step load
Turbine shaft rot. freq.	6.447	8.278	
High-speed shaft rot. freq.	7.896	10.11	Peaks shift on the frequency axis due to the variation in rotational frequency. Spectrogram dominated by the torsional vibration due to the armature.
Blade pass freq.	32.31	40.28	
Gear mesh freq.	142.1	180.7	
Armature freq.	205.3	263.1	
First natural freq.	26.78	26.51	
Second natural freq.	166.7	163.7	
Third natural freq.	687.6	784.3	
Fourth natural freq.	1233	-	
Fifth natural freq.	1857	1566	
Sixth natural freq.	2471	2352	
Note 1	Strong peaks at harmonics of 33.34 Hz.		
Note 2	Peaks at every 100 Hz.		

Load case 1: Maximum power

The first load case that was investigated is the case of minimum electrical resistance which corresponds to the maximum amount of power generated. Figure 4-23 below shows the power signal and its frequency spectrum. Note that the signal slowly moves up and down as the rotational speed fluctuates. The fluctuation in power is attributed directly to the fluctuation in the rotational speed of the drivetrain, due to the dynamic behaviour of the air driving the WT. This dynamic behaviour is the effect of the interaction of the moving air with facility and its surroundings. The signal's 'broad' shape is the result of the physical generator characteristics; permanent magnets induce current in the stationary coils as it moves past the coils, resulting in

64

a 'hill and valley' shaped signal. On the frequency spectrum, note the peaks at the harmonics of the armature frequency. These peaks are the largest peaks, as expected due to the fact that the signal is physically created by the interaction of the armature and the generator rotor.
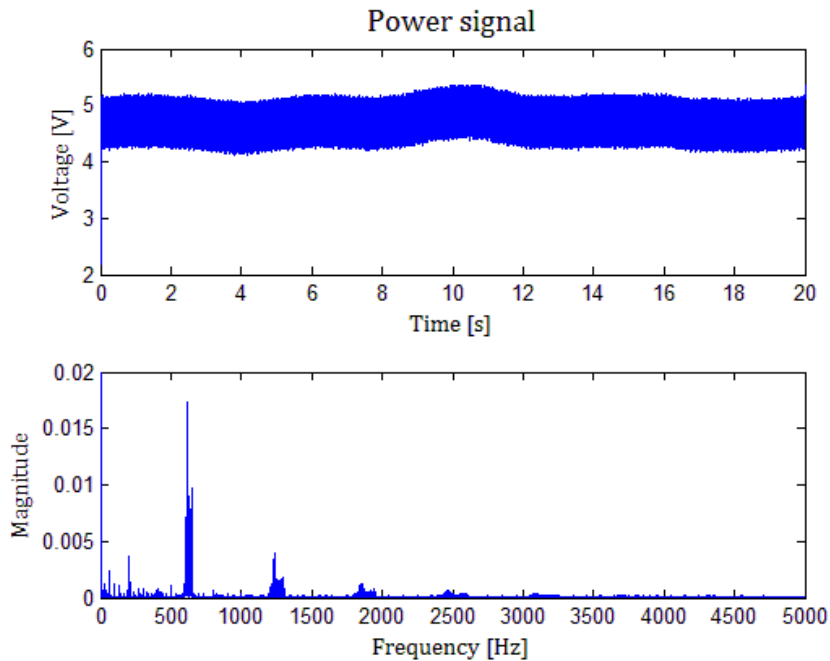

Figure 4-23: Voltage signal and the frequency spectrum when maximum power is generated.

An enlargement of the frequency spectrum, Figure 4-24, shows that there are peaks at all of the drivetrain characteristic frequencies. That is the shaft rotation frequency, the blade pass frequency, the gear mesh frequency and the armature frequency. Also note the peaks at the harmonics of 33.34 Hz.

There are peaks, although slightly smeared, at frequencies corresponding to the frequencies of the following torsional vibration modes: Mode 2 (26.78 Hz), Mode 3 (166.7 Hz), and Mode 4 (687.6 Hz), Mode 5 (1233 Hz), Mode 6 (1857 Hz), and Mode 7 (2471 Hz).

In the frequency spectrum below, peaks show at the following vibration modes: transverse and axial vibration of pedestal 3 (48.45 Hz, 85.49 Hz, 134.3 Hz, 160.0 Hz, 626.3 Hz), and vibration modes of both the gearbox shaft (185.0 Hz, 700.0 Hz, 800.0 Hz) and the generator shaft (67.60 Hz, 343.8 Hz, 633.8 Hz, 663.3 Hz).
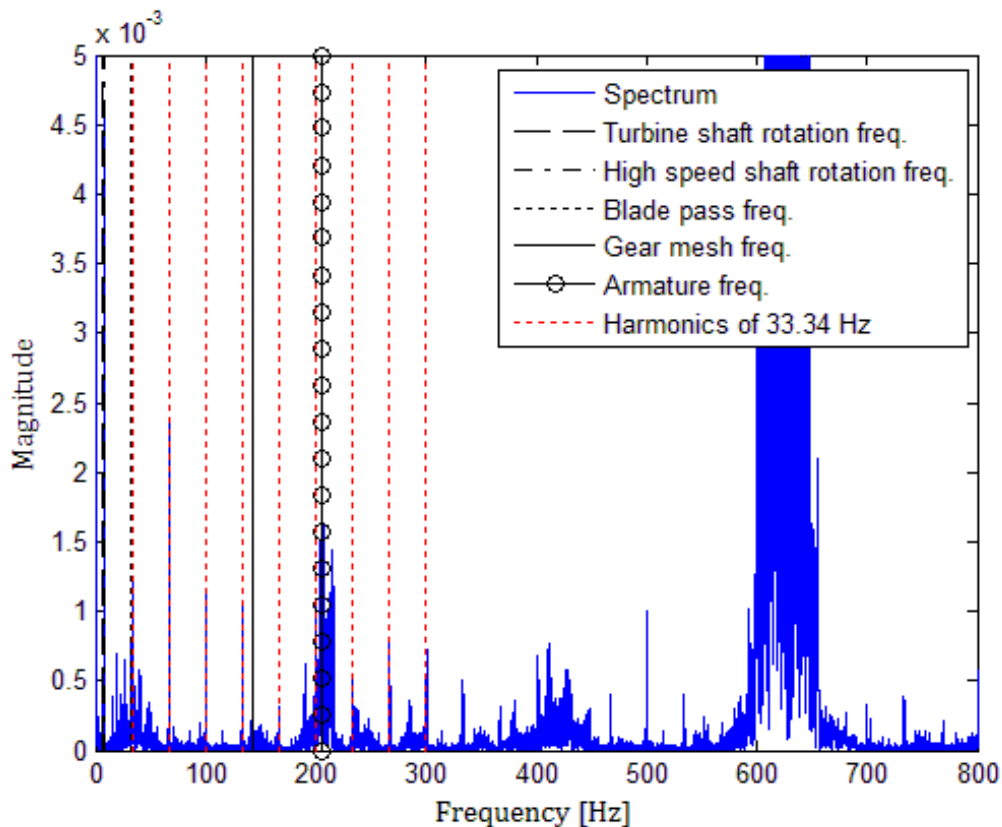
Figure 4-24: Enlarged view of the frequency spectrum measured during maximum power.

Load case 2: Minimum power

In the next instance, the electrical resistance was set to the maximum. Figure 4-25 shows the recorded signal and its frequency spectrum. Note the increased generated voltage due to an increased rotational frequency. There is an increase in the characteristic frequencies which is directly proportional to the increase in rotational speed due to the changed load condition. Note that there are large peaks at the harmonics of the armature frequency, with first harmonic being at approximately 260 Hz. It appears as if there are sidebands for all of these peaks, which can be explained by the geometry of the generator rotor (see Figure 4-2). This rotor consists of 26 magnets positioned around the centre shaft.
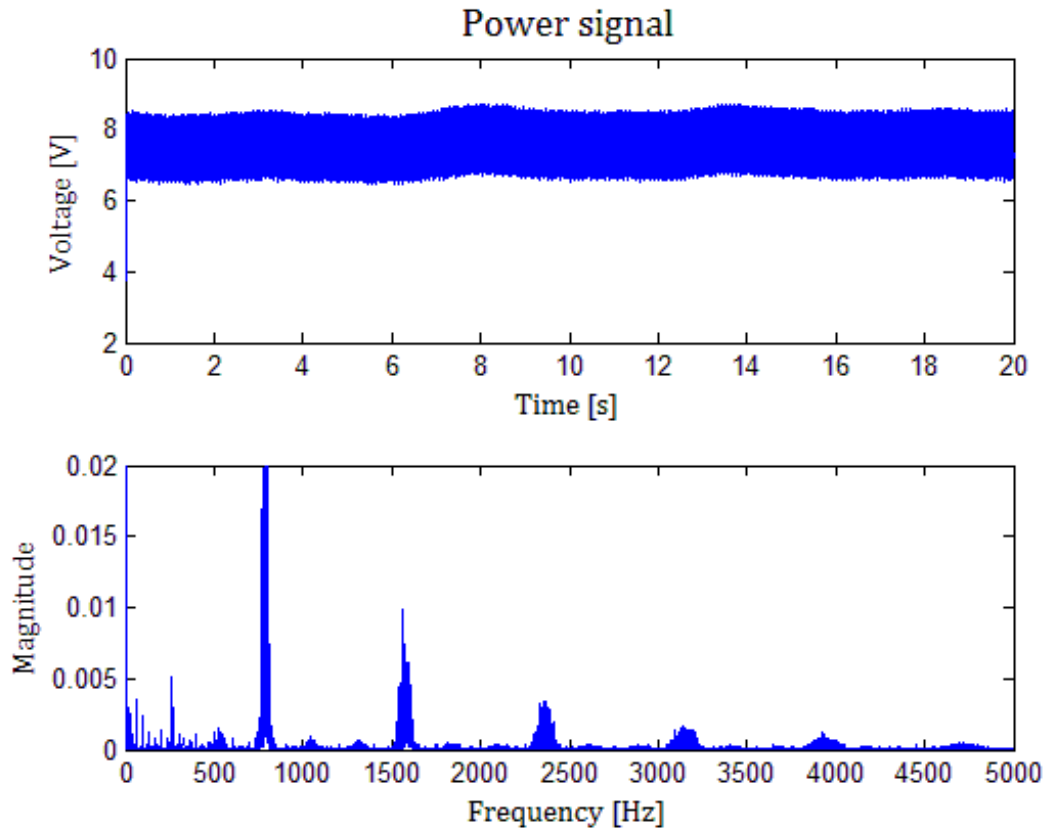
66

Figure 4-25: Voltage signal and the frequency spectrum when minimum power is generated.

Figure 4-26 is an enlargement of the lower 800 Hz of the frequency spectrum. There are clear peaks, though not the largest peaks, for each of the drivetrain characteristic frequencies. Peaks are found at the following frequencies which correspond to the frequencies of torsional vibration modes: Mode 2 (26.51 Hz), Mode 3 (166.7 Hz), Mode 4 (784.3 Hz), Mode 6 (1566 Hz), and Mode 7 (2352 Hz). Note that there are again peaks at the harmonics of 33.34 Hz, which indicates that this vibration is independent of the rotational frequency of the generator. This observation confirms that there is an external source for the peaks at these frequencies, and possibly the fan blade pass frequency as discussed in subsection 4.2.2.

Axial and transverse vibration modes of pedestal 3 (47.38 Hz, 685.8 Hz, 761.3 Hz, 16.56 Hz, 85.56 Hz, 492.0 Hz and 581.4 Hz) show as peaks on the frequency spectrum. Lateral vibration modes of the gearbox shaft (184.5 Hz and 800.0 Hz) and the generator shaft (69.16 Hz and 666.9 Hz) also show as peaks on the frequency spectrum.
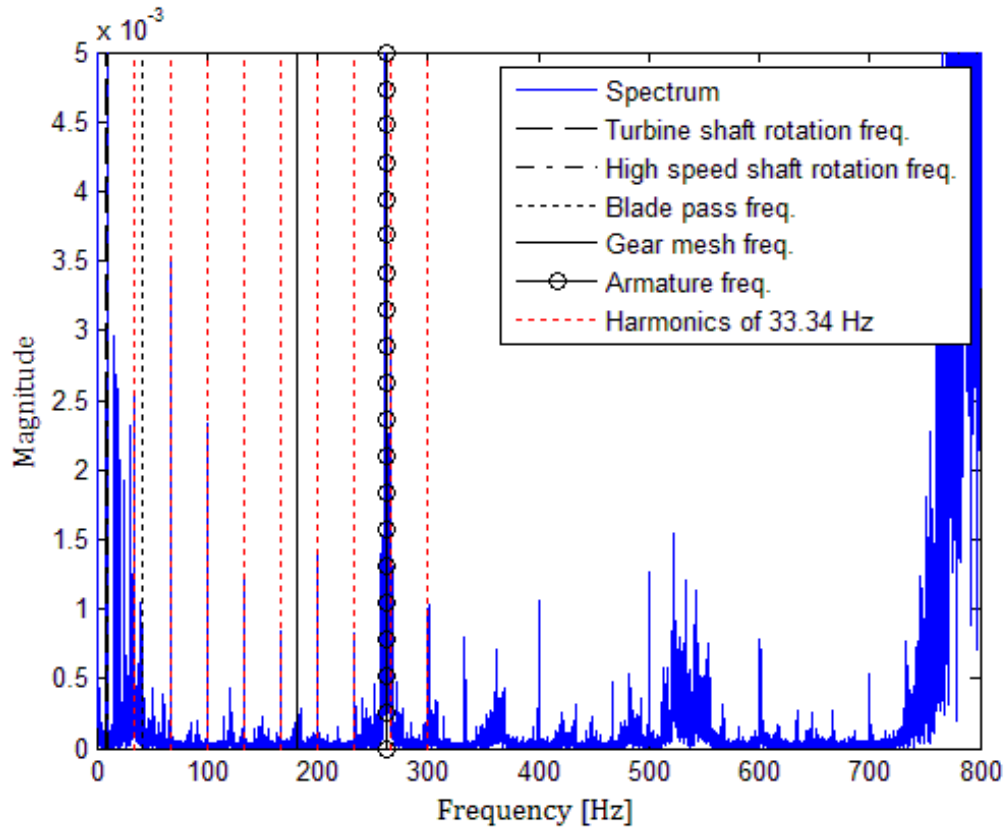
67

Figure 4-26: Enlarged view of the frequency spectrum measured during minimum power.

Load case 3: Step in power

The following investigation was that of a step in the load. After approximately three seconds of measurement, the electrical resistance was suddenly increased from the minimum to the maximum. Shown below in Figure 4-27 is the measured voltage signal. Notice the sudden increase in generated voltage at three seconds, the overshoot and oscillations in speed due to fluctuating air speed.
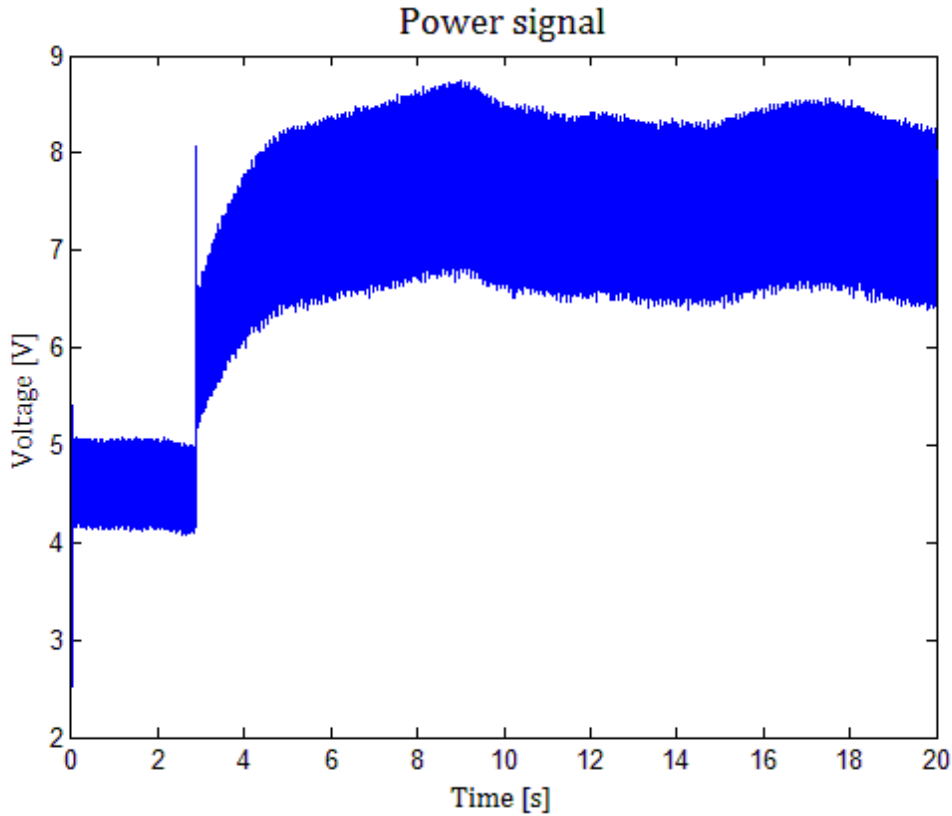
Figure 4-27: Voltage signal and the frequency spectrum when the generated power suddenly increases.

A spectrogram is most suitable for illustrating the frequency spectrum of the measured voltage signal above. Figure 4-28 below shows a spectrogram of the signal above. Windows of 0.1 seconds (1000 data points) which overlapped 0.09 seconds (900 data points) were specified to the MatLab function `spectrogram`, which returned the data points shown in the figure. The function uses a short time Fourier transform function to calculate several frequency spectra for the time dependent signal. Notice the distinct change at three seconds of measurement. Most prominent are the armature frequency at approximately 200 Hz and its harmonics. Unfortunately none of the other drivetrain characteristic frequencies are distinguishable on the spectrogram.
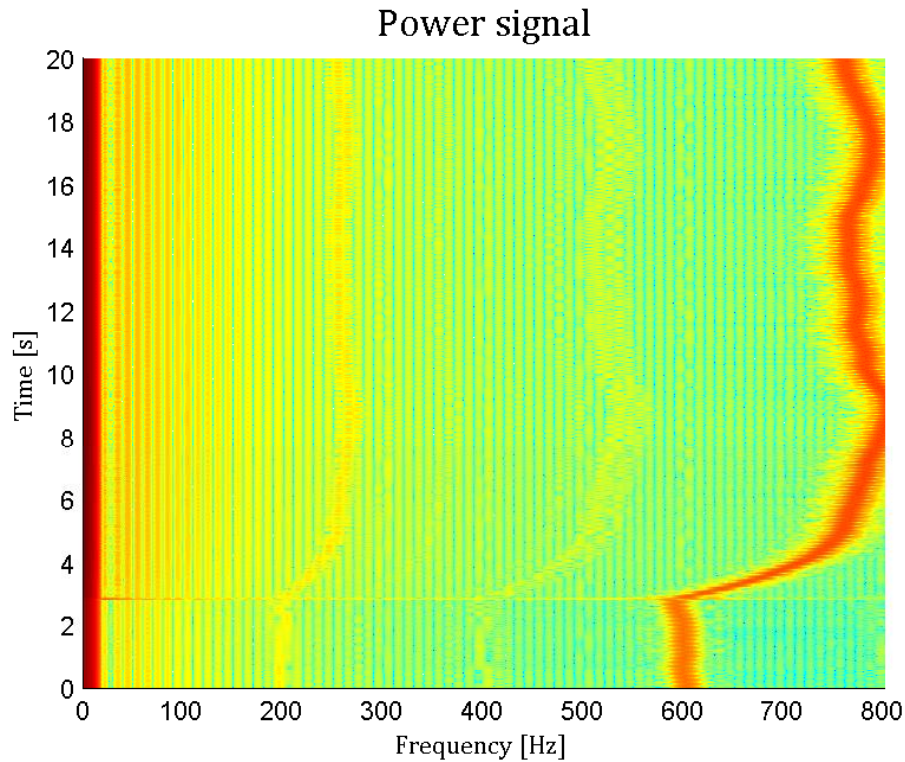
69

Figure 4-28: Spectrogram of the power signal when the electrical resistance is suddenly increased from minimum to maximum.

Figure 4-29 is another spectrogram. In this case the electrical resistance was decreased from maximum to minimum after three seconds of measurement. As in Figure 4-28, only the armature frequency is distinguishable. Since the magnitude of the torsional vibration due to the armature is much larger than all the other torsional dynamics, this characteristic vibration is most prominent on the spectrogram. Note by the background colour that there are more energy in the lower 200 Hz of the signal.
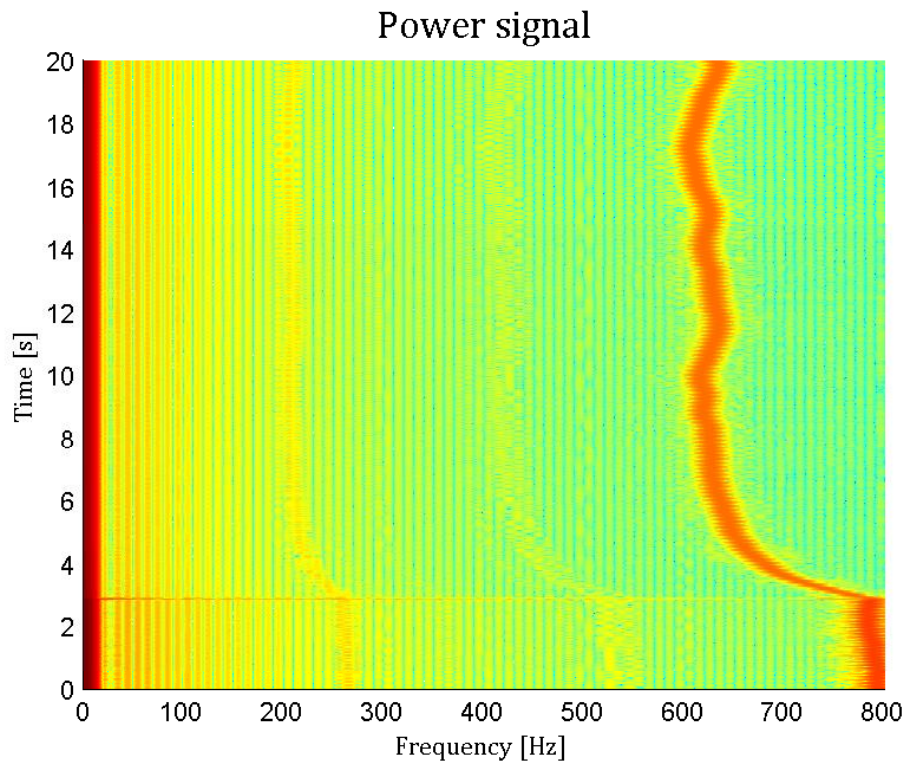
Figure 4-29: Spectrogram of the power signal when the electrical resistance is suddenly decreased from maximum to minimum.

4.3 Results summary

Rotational frequency analysis provided peaks at the natural frequencies of vibration of the first three torsional vibration modes. Power signal analysis showed clear peaks up to the sixth torsional vibration mode (excluding the rigid body mode).

A summary is made of the frequencies that were identified in Table 4-3. The table contains the following information:

1. Frequencies at which peaks were identified close to the expected frequencies of the torsional vibration modes. Both for rotational frequency and power signals the same was done.
2. Average natural frequency and the standard deviation in the right-hand side columns. Equal weight is given to rotational speed and power signal data.

71

Table 4-3: Natural frequencies identified from the measured vibration spectra.

Mode	Freq. (FEM estimation) [Hz]	Rotational frequency			Power signal		Avg.	Std. dev.
		Turbine	Turbine shaft	Low-speed gearbox shaft	Max. load	Min. load		
1	0.274							
2	28.88	26.76	26.44	26.4	26.78	26.51	26.55	0.202
3	169.9	163.7	164.1	163.1	166.7	163.7	164.1	1.192
4	693.0	670.0	625.5	632.4	687.6	784.3	680.0	66.94
5	1514				1233		1233	
6	1646				1857	1566	1712	205.8
7	2531				2471	2352	2412	84.15
8	4772							
No Significant Peak								

The table above shows that there is good agreement in the data measured at different drivetrain components. Comparing the frequencies obtained from the rotational frequency data with that obtained from the power signal data shows that there is also good agreement between the datasets measured with different instruments.

Regarding the characteristic drivetrain frequencies, the following is concluded:

1. Rotational frequencies of both shafts show as peaks on the frequency spectrum of all the rotational frequency signals.

2. Blade pass frequency shows as a peak on the frequency spectra of the rotational frequency of the first three measurement positions. It is uncertain if the vibration caused by passing blades propagates through the gearbox as the signals on the high-speed side of the drivetrain are not reliable.

3. Gear mesh frequency shows as a peak only on the frequency spectrum of the low-speed gearbox shaft's rotational frequency. Clear sidebands do not appear on the measured signals. Torsional vibration due to the meshing of the gears does not propagate through the rubber couplings.

4. Armature frequency, even though it is induced on one end of the drivetrain, shows as peak on the frequency spectra of both the turbine and the turbine shaft measurement locations. This frequency is also prominent on the frequency spectra of the power signals.

5. Without exception the frequency spectra of the power signals contained information about the abovementioned drivetrain characteristics and the torsional vibration modes.

Rotational frequency analysis and even more so the power signal analysis produced peaks at several vibration modes of the pedestals, the turbine blade and the drivetrain shafts. Natural frequencies of these components were determined experimentally beforehand and listed in Table 4-1. Several peaks in the frequency spectra of this section correspond to the listed frequencies. As expected, the natural frequencies of vibration of the components in contact with the measurement point are most prominent. In most cases these peaks could be distinguished from other peaks. By determining the natural frequencies of vibration of the pedestals, turbine blades and drivetrain shafts beforehand, it is possible to distinguish between peaks that represent these frequencies and peaks that represent drivetrain characteristic frequencies and torsional dynamics.

4.4 Model validation

The experimental results in 4.2 are now compared with the FEM estimations from 3.3. Only the first three torsional modes are considered (excluding the 0 Hz rigid body mode), since the values are drawn from at least five datasets. After comparison, the model is improved by finding model parameter values that will result in the minimum difference between the FEM and experimental results.

Table 4-4 below shows how the FEM estimations from 3.3.3 compare to the experimental results from 4.2.4. In the bottom row the difference is expressed as a percentage relative to the experimental results. Note that the FEM overestimated in every case, indicating a model that is too stiff. Interestingly the FEM estimations improve for the higher modes, from ~9 % to ~1 %.

Table 4-4: Accuracy of the initial FEM.

| Torsional mode | Modal frequency [Hz] | | | |
	1	2	3	4
Frequency FEM	Rigid body mode	28.88	169.9	693.0
Frequency Experimental		26.55	164.5	680.0
Difference [%]	-	8.776	3.283	1.912

Next the influence of two model parameters on the FEM estimations is investigated to determine whether a change in one or both of these parameter values reduces the differences shown in Table 4-4. See Figure 4-30 (a) below. The first parameter to consider is the stiffness of the gear mesh due to the uncertainty mentioned in section 3.3.2. According to the ISO standard, the upper and lower boundaries are respectively 2.08×10^5 N·mm^{-1} (single pair of gear teeth in

73

contact), and 5×10^5 N·mm^{-1} (double pair of gear teeth in contact). Initially the former was used as the gear mesh stiffness. Now, gear mesh stiffness values between 1×10^3 N·mm^{-1} and 1×10^9

N·mm^{-1} are evaluated and the corresponding frequencies of the second to fourth torsional modes are calculated. On the figure it is clear that, for the torsional modes in consideration, the change in gear mesh stiffness is only effective in significantly changing the fourth modal frequency (f_3). For each of the gear mesh stiffness values, the value which results in a minimum difference for each mode is found. The frequencies corresponding to this value is used as the new estimation and the difference is calculated. See Table 4-5 and compare with the difference in Table 4-4. Notice that there is improvement for all three modes, although not significant.

Another model parameter is considered. In section 3.2 it is described how the dynamic torsional stiffness of the couplings is unknown and therefore measured in a quasi-static manner. The measured values are 526 and 556 N·m·rad^{-1}. The FEM is evaluated for torsional stiffness values between 250 and 850 N·m·rad^{-1}. Figure 4-30 (b) shows the effect of the coupling stiffness on the estimated frequencies. A coupling stiffness of 500 N·m·rad^{-1} produces the best match, with frequencies of 27.99 Hz for the first vibration mode, 162.4 Hz for the second vibration mode, and 692.4 Hz for the third vibration mode. The new coupling stiffness produces a significant improvement of the FEM, lowering the maximum difference associated with the first mode by 3.4 %.

Torsional stiffness of the couplings is identified as the parameter that influences most the second to fourth natural frequencies. With large increments of 50 N·m·rad^{-1} the coupling torsional stiffness was adjusted and a solution was found within 5.7 % of the measured natural frequency. It may be possible to further improve the match between the FEM and the experiments by evaluating smaller coupling stiffness increments close to 500 N·m·rad^{-1}.
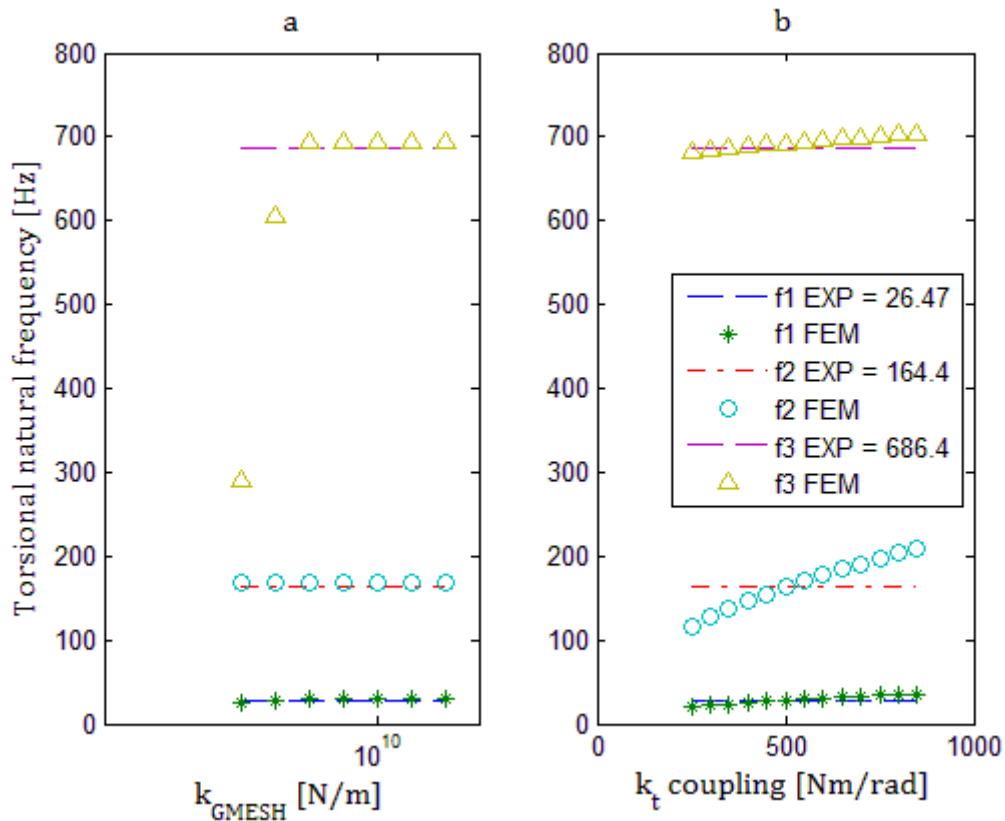
Figure 4-30: Response of the modal frequencies estimated by the FEM to the alteration of two stiffness parameters gear mesh (a) and coupling torsion (b).

Table 4-5: Accuracy of the FEM after updating certain model parameters.

	Modal frequency [Hz]			
Torsional mode	**1**	**2**	**3**	**4**
Frequency Experimental		26.47	164.4	686.4
Frequency FEM Gear mesh stiffness = $1\times 10^5\ N \cdot m^{-1}$	Rigid body mode	28.82	169.5	692.6
Difference [%]		8.878	3.102	0.9033
Frequency FEM Coupling stiffness = $500\times 10^3\ N \cdot m \cdot rad^{-1}$		27.99	162.4	692.4
Difference [%]	-	5.742	-1.217	0.8741

75

5 Conclusion

5.1 WT condition monitoring facility

This project is dedicated to the development of a WT experimental facility to allow continuous research in the renewable energy industry.

Design, manufacture and assembly of a WT condition monitoring facility are described. This facility consists of a 1.6 m diameter battery charging WT rated to produce 600 W of power, a Kestrel e160i. A single-stage speed-multiplication gearbox is included in the drivetrain, to extend the usefulness of the facility to gear damage studies. The drivetrain components are mounted on a test bench within a wind tunnel. A fan of 1.8 m diameter and 7 kW power rating creates the airflow in the wind tunnel to drive the WT.

Airflow created by the pressure drop of the fan drives the WT. Good condition of the airflow is required for two reasons: improved efficiency, and emulation of natural wind. Uniformity of the air velocity across the cross-section of the wind tunnel is ensured with an elliptical bell-mouth at the inlet of the tunnel. Initially a diffusor was going to be used at the outlet of the tunnel to recover pressure. However, it was found that a diffusor at the outlet of the tunnel is not necessary.

5.2 Torsional dynamics models

Condition monitoring of a rotating machine requires an understanding of the torsional dynamics of the drivetrain in consideration. Two mathematical models were used to estimate the torsional vibration frequencies and modes of the drivetrain, a purely torsional LMM and a three dimensional FEM. Using the FEM as reference, the LMM is able to accurately estimate the mode shapes of the first six modes – agreement was found between the modal frequencies and shapes. However, the frequencies calculated for modes 5 to 8 with the different models differ 9 % and more.

Then, using the FEM results, the estimated frequencies of the first three torsional modes were compared with the experimental measured frequencies. Initially the accuracy of the FEM is 9.1 % of the experimental results. Differences are ascribed to the following simplifications and assumptions inherent and necessary for the modelling:

76

1. Geometric simplifications.
2. Linear elastic material behaviour.
3. Representation of large inertia bodies as point masses.

In section 4.3 it is shown how the accuracy is improved to 5.7 % by updating the model parameters with the most uncertainty, namely the stiffness of the gear mesh and the torsional stiffness of the couplings. Trial and error searching of both parameters improved the model accuracy. However, the torsional stiffness of the couplings proved to influence the first frequency significantly, and even more so the second and third frequencies.

5.3   Torsional dynamics measurements

Two physical entities were measured with which the torsional vibration of the drivetrain could be determined: Firstly, rotational speed was measured with a multi-pulse per revolution tachometer. Secondly, generated power was measured by recording the voltage potential difference across the poles of the generator. Rotation speed and power signals were transformed to the frequency domain by using Matlab's FFT function to perform Fourier transforms. Peaks on the frequency domain signals indicated the characteristic frequencies of the drivetrain as well as the natural frequencies of vibration. Power signals proved to be more reliable in identifying torsional natural frequencies than the rotational speed signals.

The first method uses a black-and-white 'zebra-stripe' tape as a shaft encoder. A newly developed algorithm by Diamond et al. compensates for the irregularities in the widths of zebra-strip-sizes, or 'encoder geometry'. The algorithm is able to perform its compensation for a shaft that is not rotating at a constant speed, making it useful for the highly transient behaviour of wind turbines.

The second method uses the generated power signal. Periodic information in the power signal is identified with the help of Fourier transforms. It is shown how the generated power signal is useful for identifying the drivetrain characteristic frequencies as well as the torsional natural frequencies. One drawback of the power signal is the limitation on gaining an understanding of the vibration of the whole drivetrain, or mode shapes. Since the power signal is generated at the generator, typically on one end of the drivetrain, much of the drivetrain dynamics at the opposite end may be lost through damping between the components. It was shown how, with a simple voltage divider, a proportional voltage signal is recorded directly on the digital data logging device.

Short time Fourier transforms are determined with the built-in MatLab function `spectrogram`. Analysis of the transient power signal is done with the help of the resultant spectrogram. However, since the characteristic vibration of the armature is much larger in magnitude than all other drivetrain characteristic frequencies, the spectrogram is dominated by this one characteristic vibration.

When analysing gearbox defects, power signal analysis proved more reliable. However, since vibration due to meshing gears are large in the axial and radial directions, a more effective way to analyse gear faults is the use of an accelerometer directly on the casing of the gearbox.

Frequency spectra from both rotational frequency and power signal analysis showed peaks at some of the frequencies of vibration modes of the pedestals, turbine rotor and lateral vibration of the drivetrain shafts. It is advisable to determine these frequencies in situ to be able to distinguish between these frequencies and the vibration frequencies of interest such as the drivetrain characteristic frequencies and the torsional dynamics.

5.4 Contribution

This work contributed in the following ways to the wind turbine condition monitoring knowledge base:

1. A facility is designed and built, drawing from existing facilities. Requirements are specified for each of the components of the facility. Layout of the test setup is driven by the consideration that not only contact methods, but also optical instruments are commonly used for wind turbine investigations. The experimental setup was purpose-built to accommodate both methods. The concept can be implemented in various laboratory environments.
2. When measuring the rotational speed, the drivetrain performs in principle as expected. Drivetrain characteristics that are identified from the rotational frequency signals are the
   a. shaft rotation frequencies,
   b. blade pass frequency,
   c. armature frequency, and
   d. fan blade pass frequency.

   However, gear mesh frequency is less prominent. However, on the power signal, all of the expected drivetrain characteristic frequencies are identified. This study proves that

both measurement techniques are useful to investigate drivetrain characteristics and that power signal analysis is in some cases more useful than rotational speed analysis.

3. Measured drivetrain dynamics are as expected. A simple LMM and a more intricate FEM are formulated. The models correspond well in the lower modes as well as with the measured torsional dynamics. This work presents suitable assumptions and simplifications for developing such mathematical models.

5.5 Further work

The mathematical models of the WT drivetrain as developed in this study can be improved by including lateral vibration and the mass, damping and elastic characteristics of the support structure. Lateral modal analysis, combined with torsional modal analysis, may provide the necessary information to match both the natural frequencies and the mode shapes of mathematical models with that measured. Modal2 software, or similar, should be used to visualise modes.

During this study, as an estimate for the FEM, the torsional stiffness of the HRC couplings was measured in a quasi-static manner. However, during measurement, the couplings are subjected to dynamic loads. It is suggested that a torsional stiffness value for the model is found in a way that more closely resembles the loading condition of the couplings during experimental test.

It was observed that the torsional stiffness of the couplings is critical and, as should be expected, the torsional natural frequencies of the drivetrain are sensitive to this parameter. However, should the drivetrain be larger or even altered so that the couplings are more stiff relative to other drivetrain components, new 'critical parameters' may arise. Steel couplings may have a torsional stiffness close to that of the gear mesh, increasing the lowest torsional frequency. It is important then to identify these new critical parameters.

Future investigations can include the use of order tracking. Using order tracking to determine the torsional dynamics is more direct than using a shaft encoder and converting to time-domain signals. It is possibly more reliable.

References

Arsenault, T. J., Achuthan, A., Marzocca, P., Grappasonni, C., & Coppotelli, G. (2013). Development of a FBG based distributed strain sensor system for wind turbine structural health monitoring. *Smart Materials and Structures*, *22*(7), 75027. http://doi.org/10.1088/0964-1726/22/7/075027

Avdelidis, N. P., & Gan, T.-H. (2013). Non-destructive evaluation (NDE) of Composites: infrared (IR) thermography of wind turbine blades (pp. 634–648). http://doi.org/10.1533/9780857093554.4.634

Avitabile, P., Baqersad, J., & Niezrecki, C. (2014). Using digital image correlation and three dimensional point tracking in conjunction with real time operating data expansion techniques to predict full-field dynamic strain. In *11th International Conference on Vibration Measurements by Laser and Noncontact Techniques - AIVELA 2014: Advances and Applications* (Vol. 3, pp. 3–22). http://doi.org/10.1063/1.4879564

Barlow, J. B., Rae, W. H., & Pope, A. (2010). *Low-speed wind tunnel testing* (3rd ed.). John Wiley & Sons Ltd.

Detrick, K., Yang, J., & Ganeriwala, S. (2012). Wind Turbine Power Generation to Condition Monitoring : An Experimental Investigation Using the Wind Turbine Simulator, *2011*.

Diamond, D. H., Heyns, P. S., & Oberholster, A. J. (2016). Online shaft encoder geometry compensation for arbitrary shaft speed pro fi les using Bayesian regression. *Mechanical Systems and Signal Processing*, *81*, 402–418. http://doi.org/10.1016/j.ymssp.2016.02.060

Faulstich, S., Hahn, B., & Tavner, P. J. (2011). Wind turbine downtime and its importance for offshore deployment. *Wind Energy*, *14*(3), 327–337. http://doi.org/10.1002/we.421

Ganeriwala, S. N., Yang, J., & Richardson, M. (2011). Using Modal Analysis for Detecting Cracks in Wind Turbine Blades, (May), 10–13.

García Márquez, F. P., Tobias, A. M., Pérez, J. M. P., & Papaelias, M. (2012). Condition monitoring of wind turbines : Techniques and methods. *Renewable Energy*, *46*, 169–178. http://doi.org/10.1016/j.renene.2012.03.003

Girsang, I. P., Dhupia, J. S., Muljadi, E., Singh, M., & Pao, L. Y. (2013). Gearbox and drivetrain models to study dynamic effects of modern wind turbines. In *2013 IEEE Energy Conversion Congress and Exposition* (pp. 874–881). IEEE. http://doi.org/10.1109/ECCE.2013.6646795

GWEC. (2015). Global statistics. Retrieved May 8, 2015, from http://www.gwec.net/global-figures/graphs/

Haastrup, M., Hansen, M. R., Ebbesen, M. K., & Mouritsen, O. Ø. (2012). Modeling and Parameter Identification of Deflections in Planetary Stage of Wind Turbine Gearbox. *Modeling, Identification and Control*, *33*(1), 1–11. http://doi.org/10.4173/mic.2012.1.1

Helfrick, M. N., Pingle, P., Niezrecki, C., & Avitabile, P. (2009). Optical Non-contacting Vibration Measurement of Rotating Turbine Blades, (Dic), 1–5.

Kestrel Renewable Energy. (2014). E160i (600W). Retrieved June 5, 2015, from http://www.kestrelwind.co.za/content.asp?PageID=58

Kotzalas, M. N., & Doll, G. L. (2010). Tribological advancements for reliable wind turbine performance. *Philosophical Transactions of the Royal Society of London A: Mathematical, Physical and Engineering Sciences*, *368*(1929), 4829–4850. JOUR. Retrieved from http://rsta.royalsocietypublishing.org/content/368/1929/4829.abstract

Krüger, A. (2012). Transient Dynamic Finite Element Modelling of Flexible Rotor Systems with Nonlinear Fluid Film Bearings and Faults by, (December).

Mcmillan, D., & Ault, G. W. (2007). Quantification of Condition Monitoring Benefit for Offshore Wind Turbines, *44*(0).

Paulsen, U. S., Erne, O., Möller, T., Sanow, G., & Schmidt, T. (2009). Wind Turbine Operational and Emergency Stop Measurements Using Point Tracking Videogrammetry. Bethel.

Primus Wind Power. (2014). Air 40 Turbine. Retrieved June 5, 2015, from http://www.primuswindpower.com/wind-power-products/air-40-turbine/

Rao, S. (2011). Torsional vibration. In *Mechanical Vibrations*.

Scheepers, R. (2013). *A comparative study of Finite Element Methodologies for Torsional*

Vibration Response calculations of Bladed Rotors. University of Pretoria.

Shi, W., Kim, C.-W., Chung, C.-W., & Park, H.-C. (2013). Dynamic Modeling and Analysis of a Wind Turbine Drivetrain Using the Torsional Dynamic Model. *International Journal of Precision Engineering And Manufacturing*, *14*(1), 153–159. http://doi.org/10.1007/s12541-013-0021-2

Tchakoua, P., Wamkeue, R., Ouhrouche, M., Slaoui-hasnaoui, F., Tameghe, T. A., & Ekemb, G. (2014). Wind Turbine Condition Monitoring: State-of-the-Art Review, New Trends, and Future Challenges, 2595–2630. http://doi.org/10.3390/en7042595

Tchakoua, P., Wamkeue, R., Slaoui-Hasnaoui, F., Tameghe, T. A., & Ekemb, G. (2013). New Trends and Future Challenges for Wind Turbines Condition Monitoring, 238–245.

Tchakoua, P., Wamkeue, R., Tameghe, T. A., & Ekemb, G. (2013). A Review of Concepts and Methods for Wind Turbines Condition Monitoring, *2*(1).

Watson, S. J., Esu, O. O., Flint, J. A., & Lloyd, S. D. (2014). Integration of Low-cost Consumer Electronics for In-situ Condition Monitoring of Wind Turbine Blades. In *3rd Renewable Power Generation Conference (RPG 2014)* (Vol. 2014, p. 8.20-8.20). Institution of Engineering and Technology. http://doi.org/10.1049/cp.2014.0905

WingFan Ltd. & Co. KG. (2014). Select 6 Fan selection software.

Yang, B., & Sun, D. (2013). Testing, inspecting and monitoring technologies for wind turbine blades: A survey. *Renewable and Sustainable Energy Reviews*, *22*, 515–526. http://doi.org/10.1016/j.rser.2012.12.056

Yang, S., & Allen, M. S. (2012). Output-only Modal Analysis using Continuous-Scan Laser Doppler Vibrometry and application to a 20kW wind turbine. *Mechanical Systems and Signal Processing*, *31*, 228–245. http://doi.org/10.1016/j.ymssp.2012.04.012

Yang, W. (2015). Condition Monitoring the Drive Train of a Direct Drive Permanent Magnet Wind Turbine Using Generator Electrical Signals, *136*(May 2014), 1–8. http://doi.org/10.1115/1.4024983

Yang, W., Tavner, P. J., Crabtree, C. J., & Wilkinson, M. (2010). Cost-Effective Condition

82

Monitoring for Wind Turbines, *44*(April).

Zhou, H. F., Dou, H. Y., Qin, L. Z., Chen, Y., Ni, Y. Q., & Ko, J. M. (2014). A review of full-scale structural testing of wind turbine blades. *Renewable and Sustainable Energy Reviews*, *33*, 177–187. http://doi.org/10.1016/j.rser.2014.01.087

Appendix A.   Gear mesh stiffness with ISO 6336-1 (2006)

The international standard ISO 6336-1:2006 is titled 'Calculation of load capacity of spur and helical gears – Part 1: Basic principles, introduction and general influence factors'. Section 9 of this document suggests methods for calculating tooth stiffness parameters. It is mentioned that the accuracy of 'Method B', as it is designated in the standard, was verified by comparing it with measured results.

Physical properties (Table A-1) of the gear pair in consideration are used to estimate the tooth stiffness parameters.

Table A-1: Physical properties of the gear pair.

Physical property	Designation	Unit	Value	
			Gear	Pinion
Number of teeth	z_1, z_2	-	22	18
Normal module	-	mm	2.5	
Normal pressure angle	-	degrees	25	

Tooth stiffness parameter was then calculated according to the standard. Results of the procedure are presented in Table A-2. The calculated single stiffness for a gear tooth with the correct face width (10 mm) is 208.31×10^5 N·mm^{-1}. Gear mesh stiffness is represented by a linear spring with this stiffness.

Table A-2: Calculation of the approximate gear mesh stiffness according to ISO 6336-1.

Calculated property	Designation	Unit	Value
Minimum flexibility	q'	mm·μm·N^{-1}	0.067593
Theoretical single stiffness	c'_{th}	N·(mm·μm)$^{-1}$	14.795
Correction factor	C_M	-	0.80000
Gear blank factor	C_R	-	1.0000
Basic rack factor	C_B	-	1.8848
Single stiffness per unit face width	c'	N·(mm·μm)$^{-1}$	20.831
Single stiffness for 10 mm face width	-	kN·m^{-1}	2.0831×10^4

84

Appendix B.   Drivetrain properties

Mass is measured with a scale and rotational inertia of the solid model is estimated with the mass properties tool of SolidWorks. Table B-1 summarises the mass and rotational inertia values of the turbine subassembly, turbine shaft, and the bearings on the turbine shaft.

Table B-1: Mass and rotational inertia of drivetrain components.

Component	Mass [g]	Rotational inertia [g·mm²]
Turbine subassembly	5976	317 900 000
Turbine shaft	1862	143 900
Bearing adapter sleeve, inner race and one third of balls-and-cage	187.1	65 640

Mass and rotational inertia of all of the coupling flanges are different since all of these have different bore sizes. In Table B-2 is the mass and rotational inertia of each of the coupling flanges (including the tapered sleeve, grub screws and key), and the two rubber elements.

Table B-2: Mass and rotational inertia of coupling components.

Component	Mass [g]	Rotational inertia [g·mm²]
Coupling flange		
… on the turbine shaft	523.9	317 600
… on the low-speed gearbox shaft	542.2	320 100
… on the high-speed gearbox shaft	553.8	322 200
… on the generator shaft	548.6	323 100
Rubber element	18.31	9 409

Mass and rotational inertia of the gearbox shafts, gears, and bearing components are given Table B-3.

85

Table B-3: Mass and rotational inertia of gearbox components.

Gearbox component	Mass [g]	Rotational inertia [g·mm²]
Low-speed shaft	1 027	154 300
High-speed shaft	880.4	93 270
22 teeth gear	183.7	74 950
18 teeth gear	103.9	35 000
22 mm bearing without outer race	35.37	7 313
22 mm bearing balls-and-cage	14.29	3 950
25 mm bearing without outer race	40.23	10 160
25 mm bearing balls-and-cage	16.63	5 458

Finally, the same is specified for the components of the generator rotor, in Table B-4.

Table B-4: Mass and rotational inertia of the generator components.

Component	Mass [kg]	Rotational inertia [kg·m²]
Shaft	1.214	1.125e-3
Magnetic rotor subassembly	0.8177	1.966e-3
25 mm bearing without outer race and one third of balls-and-cage	0.01842	6.525e-6
20 mm bearing without outer race and one third of balls-and-cage	0.02026	6.608e-6

Stiffness of the shafts and couplings for the LMM

The dimensions are taken from portions of the shaft with the minimum diameter which have at least half of the shaft length. Portions with larger diameter sections are considered to be rigid. A summary of the lengths and diameters that were used, are given in Table 3-1.

Stiffness of the couplings was determined experimentally. In the experiment a torque was applied incrementally on the coupling while the corresponding angular displacement was measured. Incremental torque was applied with a lever-arm on which masses were suspended at a fixed distance from the centre of rotation. Angular displacement was measured with an Android-based smart-phone application 'Spirit level' which uses the device's built-in accelerometers to determine the device's orientation relative to an initial orientation. The stiffness of the rubber elements was found to be 526 and 556 N·m·rad^{-1}. The first value refers to the measured stiffness of the element of the coupling between the low-speed and gearbox input shafts and the second value is the measured stiffness of the other coupling.

86

Appendix C.   Drawings

Turbine boss detail
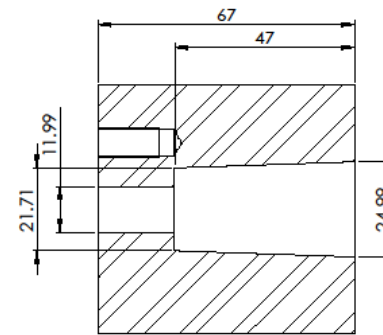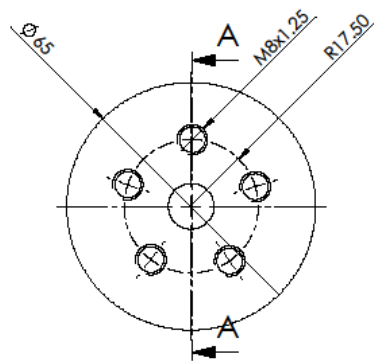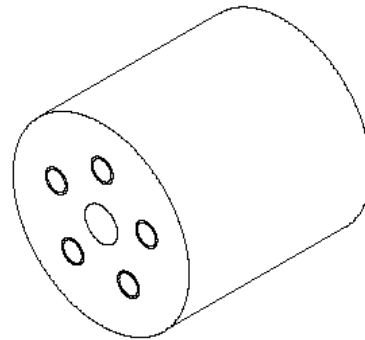
SECTION A-A

1.
2. I declare that this drawing is my own original work.
3. I am not using another student's work to hand in as my own.
4. I have not allowed, and will not allow, anyone to copy my work
   with the intention of passing it off as his or her own work.

TOLERANCES		
FROM - TO	+/-	
0 - 6	0.1	
6 - 30	0.2	
30 - 100	0.3	
100 - 300	0.5	
300 - 1000	0.8	
1000 - 3000	1.2	
3000 - PLUS	2.0	
ANGLES	1°	

ITEM NR	AANTAL	BESKRYWING
ITEM NO	QUANTITY	DESCRIPTION

VAN
SURNAME
STUDENTE NO
STUDENTE NR
PROJEKSIE
PROJECTION

VOORLETTERS
INITIALS
RIGTING
DISCIPLINE

UNIVERSITEIT VAN PRETORIA
UNIVERSITY OF PRETORIA

MATERIAAL
MATERIAL

ONDERDEEL NR
PART NR

TITEL
TITLE
TEKENING NR
DRAWING NR

A3

SKAAL 1:1
SCALE 1:1

DATUM
DATE

VOLTOOI TITELBLOK IN SWART INK/COMPLETE TITLEBLOK IN BLACK INK

Turbine boss Last saved 29 September 2016 10:32:21 PM

Test setup components

RIGHT HAND SIDE VIEW

ISOMETRIC VIEW

ITEM NO.	PART	DESCRIPTION	QTY.
1	WIND TURBINE ROTOR	KESTREL E160I	1
2	DUCT INLET	BELL MOUTH	1
3	DUCT FRAME	STEEL TUBE FRAME	1
4	DUCT	ALUMINIUM PLATE DUCT	1
5	GEARBOX	CUSTOM, SINGLE STAGE	1
6	WIND TURBINE GENERATOR	KESTREL E160I, 24V	2
7	FAN MOTOR	7.5 KW, 1000 RPM	1
8	FAN MOTOR FRAME	STEEL SECTION FRAME	1
9	DRIVETRAIN BENCH	STEEL WITH SLOTTED TOP	1

Gearbox components

ITEM NO.	PART	DESCRIPTION	QTY.
1	GEARBOX BASE	MILD STEEL, MACHINED	1
2	OUTPUT SHAFT	EN24	1
3	INPUT SHAFT	EN24	1
4	TOP BEARING HOUSING	MILD STEEL, MACHINED	4
5	BOTTOM BEAIRNG HOUSING	MILD STEEL, MACHINED	4
6	GEAR	YAMAHA STANDARD	2
7	GEARBOX TOP	MILD STEEL, MACHINED	1

Gearbox Last saved 10 October 2016 11:06:54 AM

Appendix D.   Fan data sheet

SELECT - Performance curves

Selected by Fritz Eksteen, Wingfan Africa
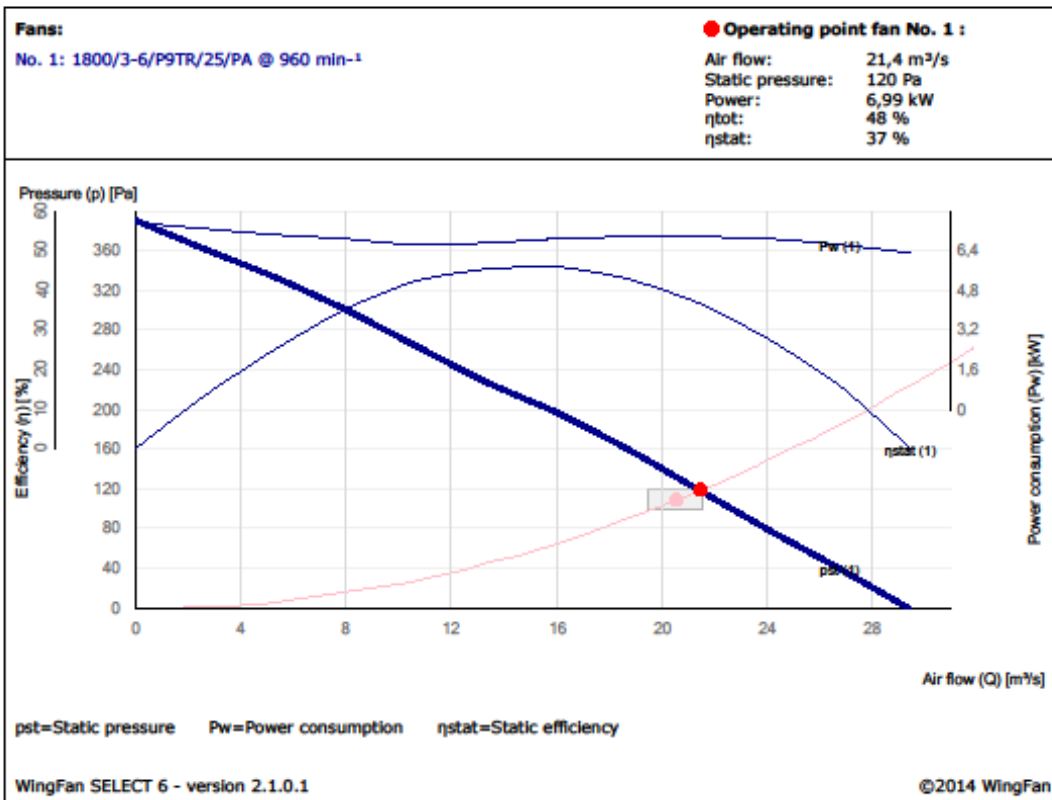**Tel: 0123451109, info@wingfan.com**

09/01/2015

Fan description:		**General:**		**Application data:**	
Diameter:	1.800 mm	Application:	Stationary cooler	Installation:	Nozzle
No. of blades:	3	Drive type:	Electric motor	Tip clearance:	0,5 %
Hub size:	6	Power freq.:	50 Hz	Rotation speed:	960 min⁻¹
Blade profile:	P9T	Poles:	free	Temperature:	25 °C
Rotation direction:	R			Altitude:	1.400 m
Pitch angle:	25°			Relative humidity:	30 %
Blade material:	PA	Simulation:	none	Air density:	1 kg/m³

Fans:

No. 1: 1800/3-6/P9TR/25/PA @ 960 min⁻¹

● **Operating point fan No. 1 :**

Air flow:	21,4 m³/s
Static pressure:	120 Pa
Power:	6,99 kW
ηtot:	48 %
ηstat:	37 %

pst=Static pressure   Pw=Power consumption   ηstat=Static efficiency

WingFan SELECT 6 - version 2.1.0.1   ©2014 WingFan

Appendix E. Model verification

Table E-1 below shows the mass properties of the low-speed gearbox shaft. The solid model properties are accurate, based on measured dimensions and mass. Note that the finite element model estimations agree well with the solid model which testifies of a close geometrical approximation by the finite element model.

Table E-1: Comparison of the finite element model properties with the solid model properties.

Low-speed gearbox shaft	Mass [Mg]	Rotational inertia [Mg·mm^2]		
		I_{zz}	I_{xx}	I_{yy}
Solid model	1.239e-3	0.2386	5.588	5.588
FEM	1.274e-3	0.2321	5.716	5.716
% difference	2.8	2.7	2.3	2.3

Appendix F. FEM mode shapes

The table below presents the displacement of certain components as calculated with the FEM, corresponding to degrees-of-freedom on the LMM. The mode shapes are illustrated graphically in sub-section 3.4.

Table F-1: Torsional mode shapes according to the FEM.

Component corresponding to DOF	Mode							
	1	**2**	**3**	**4**	**5**	**6**	**7**	**8**
	Displacement [mm]							
Turbine	5.20e-02	2.74E-02	7.36e-02	1.02e-01	1.01e-01	1.12e-01	4.73e-02	1.89e-01
LSC – turbine shaft	5.20e-02	2.74E-02	7.36e-02	1.53	1.01e-01	1.12e-01	7.1e-01	2.83e-01
LSC – low-speed gearbox shaft	5.20e-02	2.20E-01	8.83e-01	2.04e-01	7.08e-01	1.12e-01	4.73e-02	1.89e-01
22T gear	5.20e-02	2.20E-01	8.83e-01	1.02e-01	1.42	1.12e-01	4.73e-02	1.89e-01
18T gear	7.09e-02	2.74E-01	1.10	1.02e-01	1.52	1.12e-01	4.73e-02	1.89e-01
HSC – high-speed gearbox shaft	7.09e-02	3.02E-01	1.10	2.04e-01	8.09e-01	1.12e-01	4.73e-02	1.89e-01
HSC – generator shaft	7.09e-02	4.12E-01	1.47e-01	1.02e-01	1.01e-01	1.67	4.73e-02	1.89e-01
Generator rotor	7.09e-02	4.12E-01	1.47e-01	1.02e-01	1.01e-01	1.12e-01	4.73e-02	1.89e-01

Appendix G.   System dynamics

Subsection 4.2 is dedicated to the experimental investigation of system dynamics. This appendix explains and illustrates the particular experiments.

Pedestal

The drivetrain is mounted on three pedestals, each which may have vibration modes in the two horizontal directions. These pedestals may also vibrate torsional around the vertical. However, torsional vibration modes will only affect the drivetrain torsional dynamics if it manifests in significant horizontal movement of the pedestals. All these modes are considered. During a modal test, both horizontal and torsional modes were excited by impacting the pedestal either in its centre, or at an offset position. When analysing the data, all natural frequencies were grouped in one of two horizontal vibration modes, transverse or axial, by placing it in the direction where it produced a larger peak. Pictures of the test procedure follow below.

Figure G-1 shows the placement of a three-axis accelerometer on a plumber block on the first pedestal.
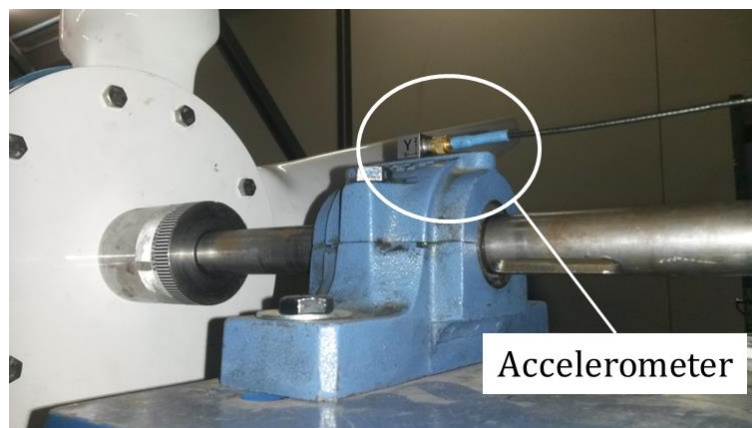
Figure G-1: Placement of an accelerometer on the first pedestal.

Pedestals (refer to Figure 4-1) were impacted at the locations and in the directions shown in Figure G-2.
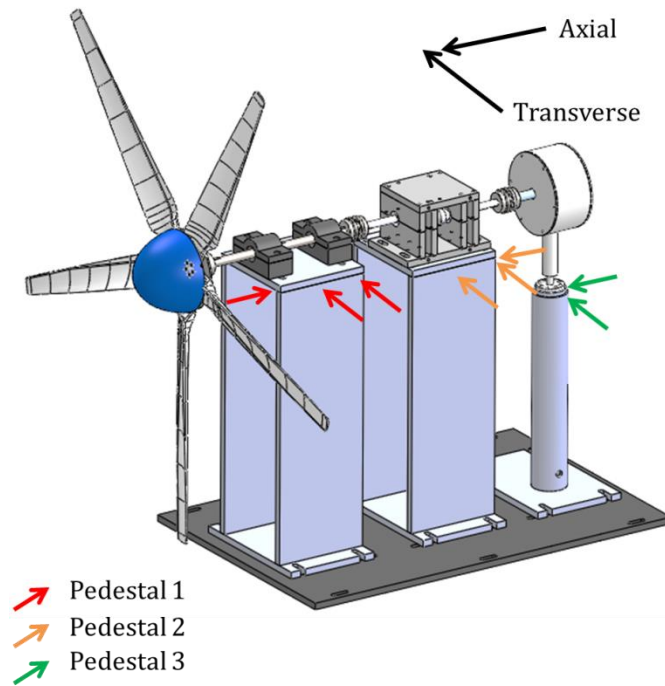
Figure G-2: Positions and directions of impact.

Figure G-3 shows the large modal impact hammer (with a soft tip), the CoCo FFT analyser and the signal processor of the impact hammer.

Figure G-3: Modal impact hammer, CoCo FFT analyser and signal conditioner used in dynamics measurements of the setup test-bench

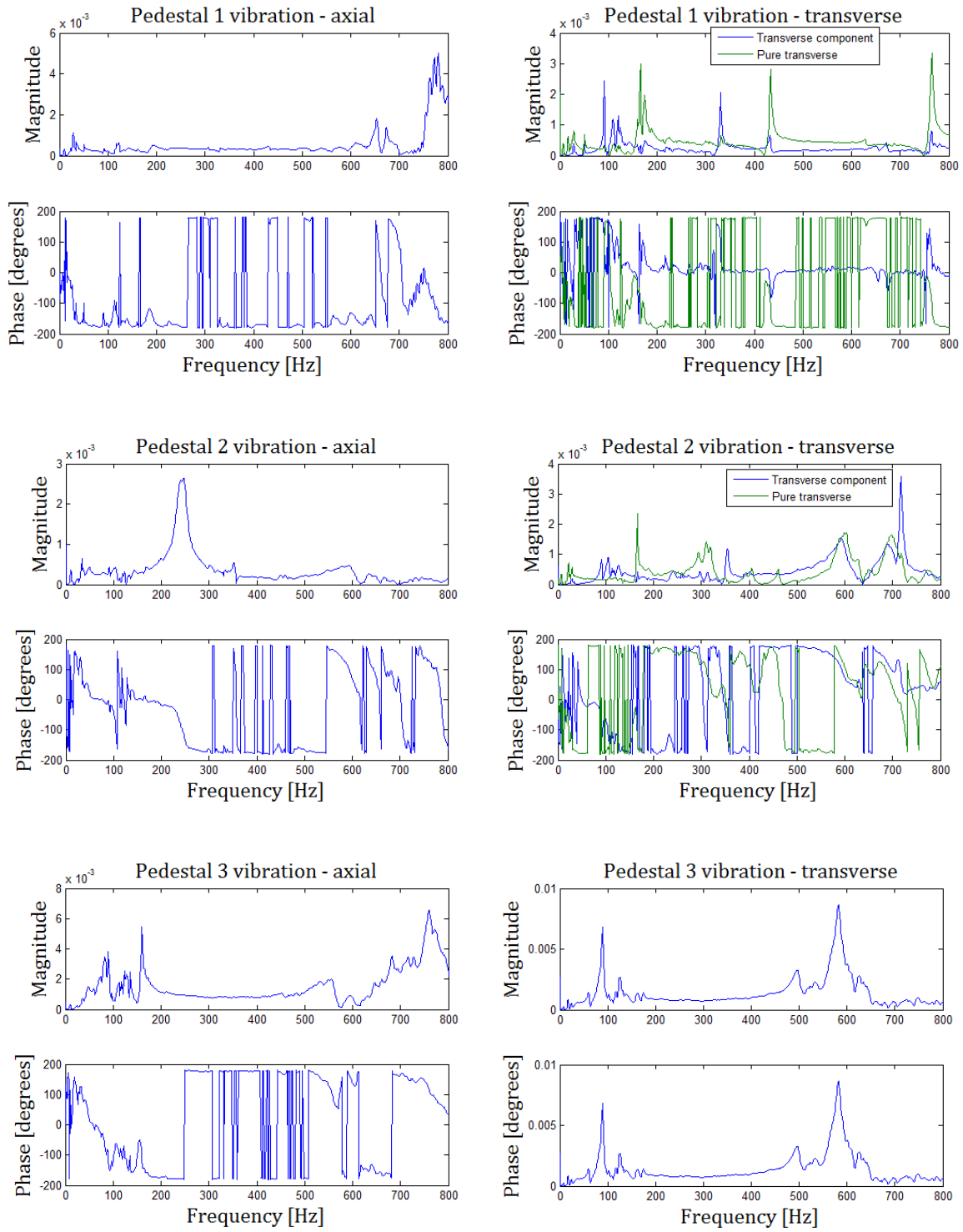Magnitude and phase information obtained from the tests are shown in the FRF's in Figure G-4 below.

Figure G-4: FRFs of the setup pedestals

Blade

Blades vibrate in the plane of rotation, orthogonal to the plane of rotation, longitudinally, torsional. Blade vibration modes can also be coupled. Figure G-5 shows the placement of an accelerometer on the blade tip. The modal impact hammer that was used to excite the vibration of the blade, and measure the impulse force, is shown in Figure G-6. Notice the Nylon tip. The combined effect of the Nylon tip and the sponge protection on the blade allowed for excitation of vibration modes in the desired frequency range. The three directions of impact to excite the mentioned vibration modes are shown in Figure G-7.
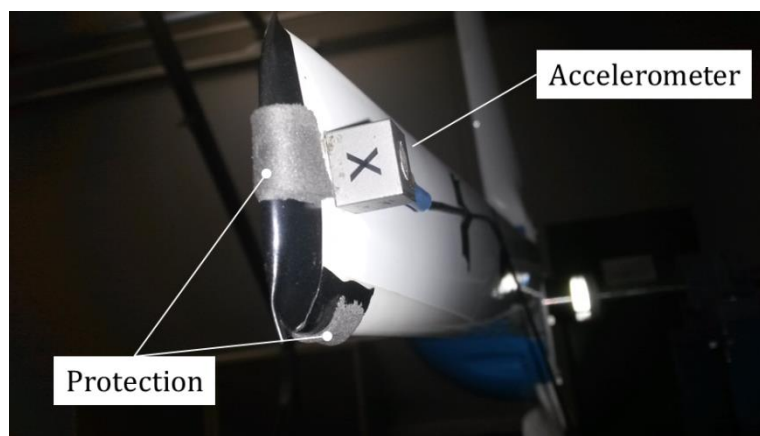
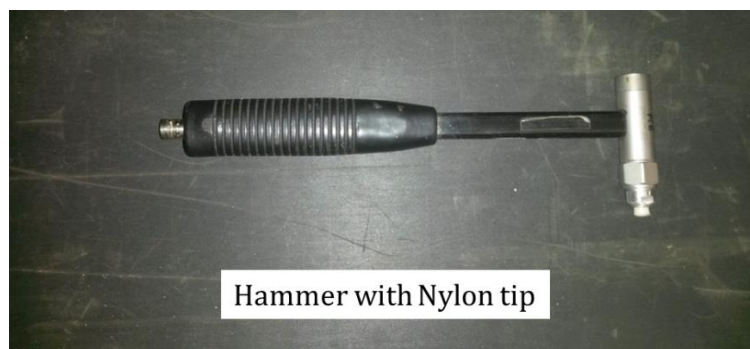Figure G-5: Instruments for the modal impact test of the wind turbine blade.

Figure G-6: Modal impact hammer with a Nylon tip that was used to excite the vibration modes and measure the impact on the blade.
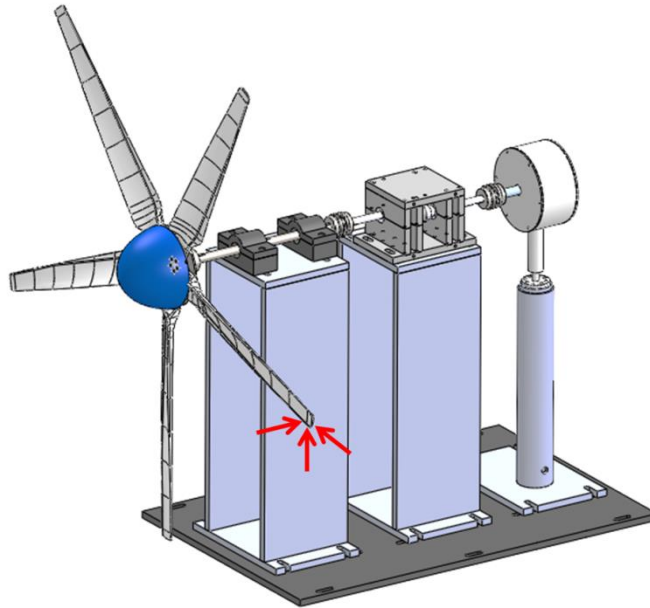
Figure G-7: Positions and directions of impact on the wind turbine blade.

Figure G-8 shows the FRFs that were obtained by measuring the response of the blade to the given impact. Frequencies of the vibration modes are identified from these FRFs and presented in Table 4-1.
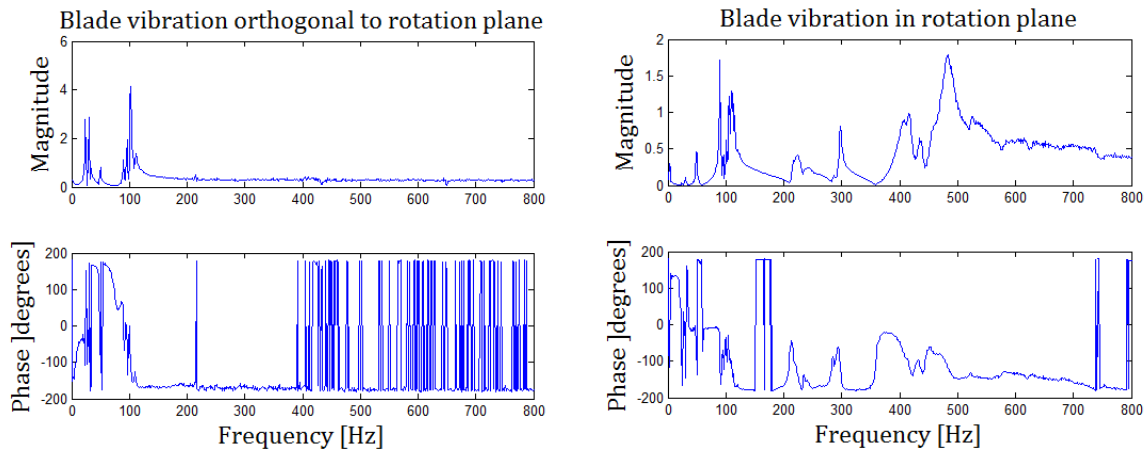

Figure G-8: FRFs of the WT bade.

Lateral vibration of shafts

Figure G-9 shows the impact (excitation) locations and the locations where the response was measured with an accelerometer. Acceleration was measured in the same direction as the

97

excitation. A modal hammer was used to excite the drivetrain components to vibrate at the natural frequencies while the response is measured with an accelerometer.
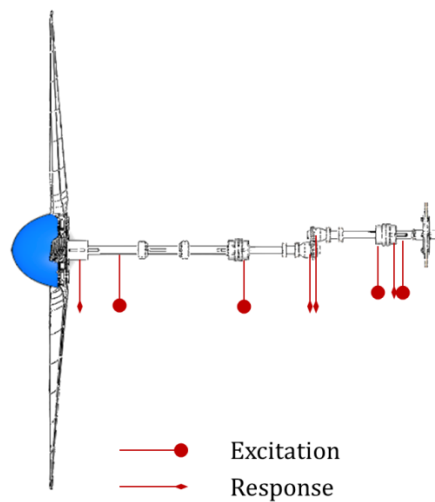

Figure G-9: Modal analysis locations of excitation and locations of measurement.

Figure G-10, below, shows the FRFs that are used to identify the natural frequencies of the shafts. Natural frequencies are the frequencies on the FRF's at which the magnitude of vibration is significantly larger than at other frequencies, hence the peaks. These frequencies are also indicated with a phase change of 180 degrees.
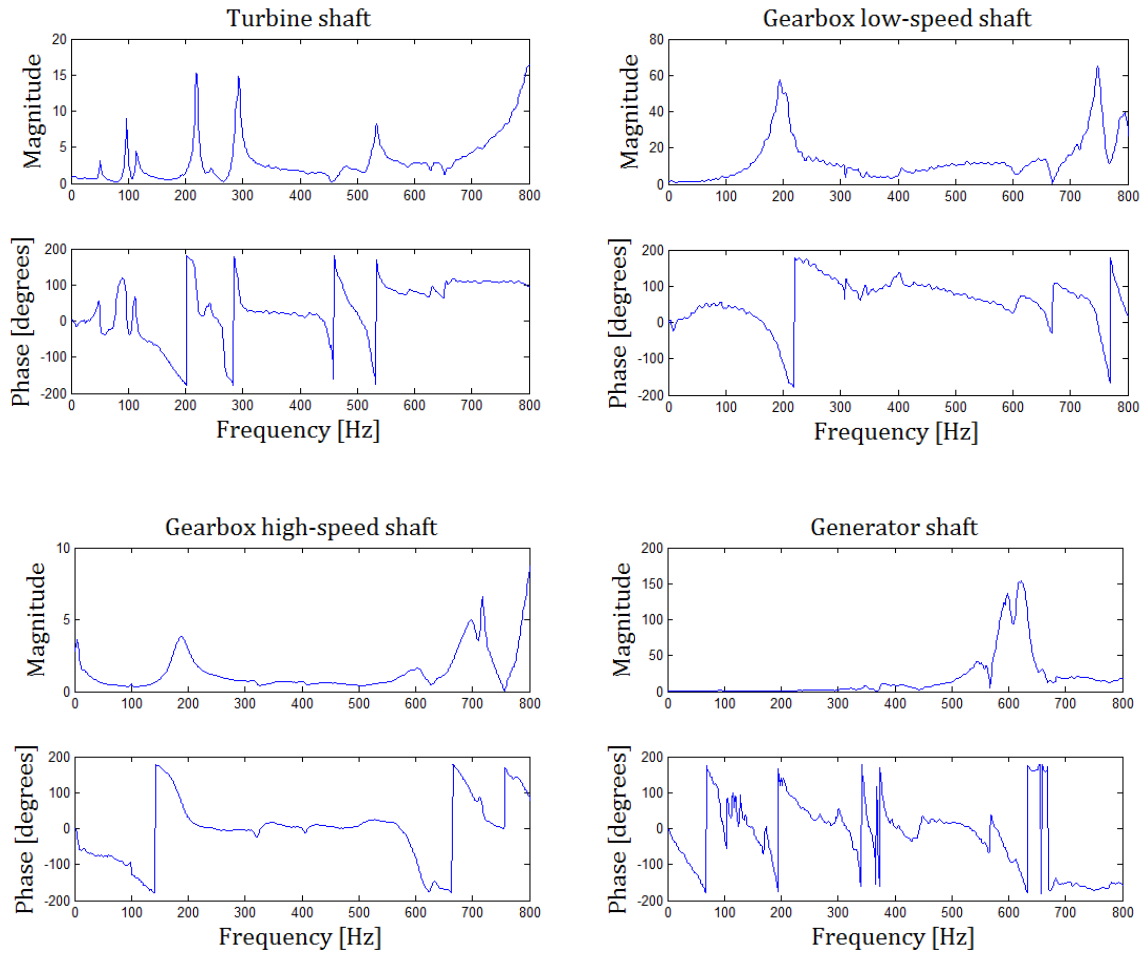
98

Figure G-10: FRFs of the drivetrain shafts in lateral vibration.